UC Berkeley
UC Berkeley Electronic Theses and Dissertations

Title

Multi-Scale Studies of Transport and Adsorption Phenomena of Cement-based Materials in Aqueous and Saline Environment

Permalink

https://escholarship.org/uc/item/4wn51541

Author

Yoon, Se Yoon

Publication Date

2012

Peer reviewed|Thesis/dissertation

Multi-Scale Studies of Transport and Adsorption Phenomena of Cement-based Materials in Aqueous and Saline Environment

By

Se Yoon Yoon

A dissertation submitted in partial satisfaction of the

requirements for the degree of

Doctor of Philosophy

in

Engineering – Civil and Environmental Engineering
in the

Graduate Division

of the

University of California, Berkeley

Committee in charge:

Professor Paulo J.M. Monteiro
Professor Claudia P. Ostertag
Professor Garrison Sposito

Fall 2012

Abstract

Multi-Scale Studies of Transport and Adsorption Phenomena of Cement-based
Materials in Aqueous and Saline Environment

by

Se Yoon Yoon

Doctor of Philosophy in Engineering – Civil and Environmental Engineering

University of California, Berkeley

Professor Paulo J.M. Monteiro, Chair

The transport and adsorption phenomena in cement-based materials are the
most important processes in the durability of concrete structures or nuclear waste
containers, as they are precursors to a number of deterioration processes such as
chloride-induced corrosion, sulfate attack, carbonation, etc. Despite this importance,
our understanding of these processes remains limited because the pore structure and
composition of concrete are complex. In addition, the range of the pore sizes, from
nanometers to millimeters, requires the multi-scale modeling of the transport and
adsorption processes. Among the various environments that cement-based materials are
exposed to, aqueous and saline environments represent the most common types.
Therefore, this dissertation investigates the adsorption and transport phenomena of
cement-based materials exposed to an aqueous and saline environment from atomic to
macro-scales using different arrays of novel spectroscopic techniques and simulation
methods, such as scanning transmission X-ray microscopy (STXM), X-ray absorption
near edge structure (XANES), molecular dynamics (MD), and finite element method
(FEM). The structure and transport of water molecules through interlayer spacing of
tobermorite was investigated using MD simulations because the interlayer water of
calcium silicate hydrate (C-S-H) gel influences various material properties of concrete.
The adsorption processes of cementitious phases interacting with sodium and chloride
ions at the nano-scale were identified using STXM and XANES measurements. A
mathematical model and FEM procedure were developed to identify the effect of
surface treatments at macro-scale on ionic transport phenomena of surface-treated
concrete. Finally, this dissertation introduced a new material, calcined layered double
hydroxide (CLDH), to prevent chloride-induced deterioration.

Acknowledgements

I would like to acknowledge many people helping to bring this thesis together. First of all, I would like to thank my thesis advisor and mentor, Paulo J.M. Monteiro, for giving me the great opportunity to study and research at U.C. Berkeley, as well as a role model to be a respectable scholar. Despite a lot of trial and error to find research directions, Professor Monteiro has encouraged and guided me to solve the problems that I have met in the way of the research. My gratitude is also due to my committee members, Drs. Claudia P. Ostertag and Garrison Sposito for their advice.

All the members of our concrete lab have provided technical support and advice over the last five years. I am especially grateful to Juhyuk Moon, Sung-Chul Bae, Sejung Rosie Chae, Cagla Meral, Pierre-Adrien Itty, and Gabriel Jen. I also would like to thank Dr. Juyoung Ha, former postdoctoral research fellow in our group, and Dr. Sang-Gyun Oh, former visiting scholar, for helping me developing scientific perspectives and research directions. Discussions with them are always valuable to find the way in the research. This work would have been much more difficult without the helps from beamline scientists at Advanced Light Sources (ALS). David A. Kilcoyne has been particularly generous and supportive during my synchrotron based spectroscopic experiments. I wish to thank Timothy Teague and Lev Stepanov for help in performing all the experimental measurements.

Lastly, I greatly appreciate to my family for their support and love. It is no doubt that their love made me to achieve this goal. In particular, I thank my parents, Im-Sook Im and Bum-Sik Yoon, for selflessly giving me everything that they have. I respect my father who supported my decision to explore different world. I know that my mother has prayed every day since I came to the U.S. from my country. I acknowledge my mother-in-law, Hosim Joo, for her support and love. Her visit and cuisine was my biggest asset for pursuing Ph.D. Most of all, I would like to thank my wife, In-Hee Choi, for all the support and love. She made the life in Berkeley be the most wonderful and joyful moments in my life. I am also sorry that I cannot support her during the last semester of her Ph.D. candidacy nearby her.

Table of Contents

List of Tables

List of Figures

vii

Chapter 1. Introduction

1.1. Motivation for the Research

Concrete is the most extensively used construction material in the construction industry worldwide [1], and cementation is the most commonly used method for solidifying radioactive waste in reinforced concrete containers [2]. Therefore, the need for a more durable cement-based material has not been lost on the global engineering community. Steel bars for concrete reinforcement are subject to corrosion, as chloride ingress and carbonation initiate the corrosion process despite the fact that the ionic transport is not harmful to the constituents and properties of concrete [3]. The other deterioration mechanisms, such as sulfate attack, make the cementitious phases unstable in aggressive environments.

A characteristic common to all of these deterioration processes is that transport and adsorption are the precursors that initiate the deterioration [4]. In spite of the great influence of transport and adsorption on the deterioration mechanism, they are difficult to study because cement-based materials reveal complex phases and pore structures. Concrete is a composite material consisting of a porous cement paste matrix and discrete aggregate particles. Aggregate sizes typically range from 0.1 to 20 mm, covering two orders of magnitude. The cement paste matrix is neither a simple nor a homogenous phase. The unhydrated cement particle is also a complex agglomeration of calcium silicate, aluminate, ferrite, and sulfate phases, ranging from 0.001 to 0.1 mm [5]. When hydration is initiated, various phases, such as calcium silicate hydrates, ettringite, monosulfoaluminate, and calcium hydroxide, are not only formed, but they also generate pores of various sizes ranging from 1nm to 1 mm. It is, therefore, essential to have a clear understanding of the transport and adsorption processes on multiple scales.

In particular, the marine environment has long been one of the most aggressive environments for reinforced concrete. In the case of solidified radioactive waste, although no high-level radioactive waste has been disposed into marine environments, coastal environments—often saline—are frequently considered as potential sites for low-level radioactive waste [6]. On the other hand, many reinforced concrete structures, such as bridges, harbors, power stations, and pre-stressed concrete storage tanks, have been built near or under marine environments. In addition, the use of de-icing salt and unwashed sea sand exposes concrete structures to the saline condition [7]. Therefore, using a multi-scale study, this dissertation attempts to investigate the transport and adsorption phenomena of cement-based materials exposed to aqueous and saline environments and to suggest a method to protect the cement-based materials in such environments.

1.2. Literature Review

This section presents the fundamentals of Portland cement and its hydration, which remain stable over long periods of time. A brief description of the complex porous system in the cement paste matrix is also given. A summary of recent advances in modeling ionic and moisture transport through such a complex porous matrix is then provided. As one of the common protective methods against aggressive transport, surface treatments are introduced in the following subsection. Lastly, since chloride ions, which are a primary element of saline solutions, are adsorbed by the hydration product, a summary of the main processes are described.

1.2.1 Portland Cement and Concrete: A Short Description

Clinker, which is the precursor of Portland cement, is produced by calcining limestone and clay minerals up to $1450 \,^{\circ}C$. A few percent of gypsum (a source of sulfate) is then added to the clinker to control the set rate of Portland cement at early ages. The major Portland cement minerals are tricalcium silicate ($3CaO \cdot SiO_2$ or C_3S), dicalcium silicate ($2CaO \cdot SiO_2$ or C_2S), tricalcium aluminate ($3CaO \cdot Al_2O_3$ or C_3A), and tetracalcium alumino-ferrite ($2CaO \cdot Al_2O_3 \cdot Fe_2O_3$, C_4AF)[1]. The chemical reaction of cement with water, commonly referred to as hydration, produces hydrated compounds. According to ASTM C 125 [8], *concrete* is defined as a mixture of cement (binder), water, fine aggregate (commonly sand), and coarse aggregate (commonly gravel); *mortar* is defined as a mixture of fine aggregate, cement, and water without a coarse aggregate.

Hydration of the calcium silicate phases (C_3S and C_2S) produces calcium hydroxide and a family of calcium silicate hydrates (C-S-H), which has a poorly crystallized structure and was recently described as a nano-crystalline structure with slight bent CaO sheets and additionally disordered silicate chains based on the tobermorite crystal structure [9]. C-S-H phases act as a primary binding phase in the hardened cement paste. For this reason, there is strong motivation to identify the structure of C-S-H and improve its strength and durability. Recent molecular simulation and experimental studies have investigated the nature of the C-S-H phases and suggested its structural model based on the recently defined structure of 14 Å tobermorite and jennite [10, 11]. The hydration of aluminate, ferrite, and sulfate phases produces Al_2O_3-Fe_2O_3-mono (AFm) phases ($[Ca_2(Al,Fe)(OH)_6] \cdot 1/2X \cdot nH_2O$) and Al_2O_3-Fe_2O_3-tri (AFt) phases ($[Ca_3(Al,Fe)(OH)_6]_2 \cdot X_3 \cdot nH_2O$), where many anions can serve as *X*. The AFm phase has its name due to the mono formula unit of CaX in another way of expressing the formula, $C_3(A,F) \cdot CaX \cdot nH_2O$. The term AFt refers to the triple formula units of CaX in the formula, $C_3(A,F) \cdot 3CaX \cdot nH_2O$. The major AFm phases occupying the greatest proportion in the Portland cement hydration are monosulfoaluminate (X is SO_4^{2-}), which is also abbreviated as monosulfate, monocarboaluminate (X is CO_3^{2-}), and hydroxyl-

---

[1] Cement chemists use the following abbreviations: $C = CaO$, $S = SiO_2$, $A = Al_2O_3$, and $F = Fe_2O_3$

AFm (X is $2OH^-$). The most important AFt phase is ettringite (X is SO_4^{2-}), which is formed during the early hydration of most Portland cements and subsequently transforms to monosulfoaluminate.

The manufacturing process of Portland cement generates a large amount of carbon dioxide, producing 650~920 kg of CO_2 per one ton of Portland cement. The manufacturing of cement is thus responsible for about 7~8 percent of all CO_2 emissions worldwide [12]. To reduce the CO_2 impact, industry waste or supplementary cementing, such as fly ash, blast furnace slag, silica fume, rice husk ash and metakaolin, can be used as partial replacements for Portland cement. On the other hand, more durable cement-based materials can also reduce CO_2 emissions, thereby increasing the service life of the concrete structure.

1.2.2. Ionic Transport (Nernst-Plank/Poisson Model)

Recently, two comprehensive models have been developed to simulate ionic transport into cement-based materials: electrochemical chloride removal (ECR) [13-16] and the Nernst-Plank/Poisson (NPP) model [17-19]. The NPP model has been extended to describe chemical activity [13], temperature effects [20], partial saturation [21], convection [16], and other processes. Due to these improvements, this thesis focuses on the NPP model.

Cement-based materials are porous media that contain both a persistent solid matrix and a void space ranging from nano- to- millimeters in size. At pore scale, a common characteristic of the pore space in cement-based materials is that all the pores can be occupied by water (liquid phase) and air (gas phase), even though their proportions depend on the humidity and environments in contact with the concrete structure's boundaries. Therefore, the sampling volume representing the behavior of the cement-based materials must be sufficiently small and contain all of the solid, liquid, and gas phases. With these considerations, the homogenization technique (Representative Elementary Volume, REV) was introduced to a conservation and transport equation at microscopic level [21]. This REV concept will be discussed in greater detail following an illustration of the conservation and transport equations described below.

The conservation equation for ionic transport at pore scale is given by the following microscopic equation:

$$0 = \frac{\partial C_i}{\partial t} + \nabla \cdot j_i + r_i \tag{1.1}$$

where, C_i is the concentration of the species i, j_i is the ionic flux, r_i is the chemical reaction and t is the time variable. The Nernst-Plank equation is used to describe ionic transport in porous media [17, 18]. The equation not only includes the effect of concentration gradients but also that of the electric field, meaning that this equation is

more appropriate for modeling the electric potential field generated by the external voltage [22]. For this reason, the equation has been extended to involve other parameters, such as chemical activity and partial saturation [4]. The brief derivation of the Nernst-Plank equation is as follows:

The flux density of an ionic species i is proportional to its electrochemical potential gradient:

$$j_i = -\frac{D_i C_i}{RT} \nabla \mu_i \qquad (1.2)$$

where, C_i is the concentration of the ionic species i, D_i is the diffusion coefficient, μ_i is the electrochemical potential, R is the ideal gas constant, and T is the temperature. The electrochemical potential, μ_i, is defined as:

$$\mu_i = \mu_i^o + RT \ln\left(\gamma_i C_i\right) + z_i F \phi \qquad (1.3)$$

where μ_i^o is a reference level, γ_i is the chemical activity coefficient, z_i is the charge valance, F is the Faraday constant, and ϕ is the electrical potential. Therefore, the flux density is:

$$j_i = -D_i \left(\nabla C_i + \frac{z_i F}{RT} C_i \nabla \phi + C_i \nabla \left(\ln \gamma_i \right) \right) \qquad (1.4)$$

After the flux density (1.4) is substituted into the conservation equation (1.1), the Nernst-Planck equation can be derived.
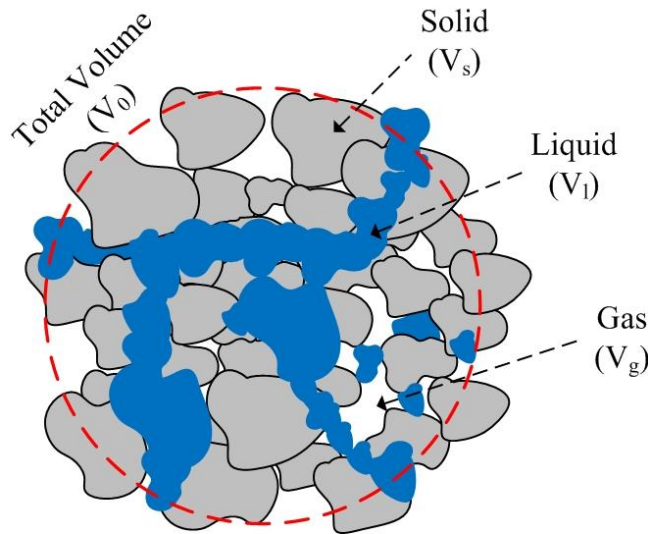
Figure 1-1. Representative elementary volume (REV) of cement-based materials.

We have discussed the process of developing the continuum model. The size of REV's size will be reviewed next, which must contain gas, liquid, and solid phases as shown in Figure 1-1. It is required to define any averaged characteristic of the REV before starting the derivations. The total volume of the REV is V_0, which is the sum of each phase, the gas phase (air, V_g), the liquid phase (water, V_l), and the solid phase (solid matrix, V_s). The volumetric fractions of liquid (θ_l) and gas (θ_g) are represented in the following equations:

$$\theta_l = V_l / V_0 \qquad \text{and} \qquad \theta_g = V_g / V_0 \tag{1.5}$$

The extensive properties (e) of an α-phase per unit volume is denoted by e_α. The volumetric intrinsic phase and volumetric phase averages of e_α are, respectively:

$$\overline{e_\alpha}^\alpha = \frac{1}{V_\alpha} \int_{V_\alpha} e_\alpha dV \quad \text{and} \quad \overline{e_\alpha} = \frac{1}{V_0} \int_{V_\alpha} e_\alpha dV \tag{1.6}$$

Therefore, the relation between the two values is:

$$\overline{e_\alpha} = \theta_\alpha \overline{e_\alpha}^\alpha \tag{1.7}$$

The transport equation is derived from averaging the conservation equation (1.1), resulting in the following equation:

$$0 = \overline{\frac{\partial C_i}{\partial t}} + \overline{\nabla \cdot j_i} + \overline{r_i} \tag{1.8}$$

Now, we need to introduce the Leibniz integral rule [23]. Assuming that a function, f, and the derivation, $\partial f/\partial x$, are continuous over the integration range, y_0, the Leibniz integral rule is as follows:

$$\frac{\partial}{\partial x} \int_{y_0} f(x,y) dy = \int_{y_0} \frac{\partial}{\partial x} f(x,y) dy + \int_{y_0} \frac{\partial}{\partial y} f(x,y) \frac{\partial y}{\partial x} dy \tag{1.9}$$

According to the Leibniz integral rule and the divergence theorem, the first term of Equation (1.8) on the right side is given by:

$$\overline{\frac{\partial C_i}{\partial t}} = \frac{\partial \theta_l \overline{C_i}^l}{\partial t} - \frac{1}{V_0} \int_{S_{ls}} \cancel{C_i v \cdot n_{ls} dS} - \frac{1}{V_0} \int_{S_{lg}} \cancel{C_i v \cdot n_{lg} dS} \tag{1.10}$$

where, v is the REV's velocity of movement, and $S_{\alpha\beta}$ is the surface between α and β-phases. The deformation of the cement-based materials is negligible, meaning that the integrals are cancelled out. Furthermore, following the procedure above, the second term of Equation (1.8) on the right side is given by:

$$\overline{\nabla \cdot j_i} = \nabla \cdot \theta_l \overline{j_i}^l + \frac{1}{V_0} \int_{S_{ls}} j_i \cdot n_{ls} dS + \frac{1}{V_0} \int_{S_{lg}} j_i \cdot n_{lg} dS \qquad (1.11)$$

The solid/liquid interface can have some ionic movements, such as surface-sorption and ion-exchange, whereas only the water-filled paths contribute to ionic transport and ions cannot move from liquid to gas phases, meaning that the second integral is cancelled out. By substituting Equations (1.10) and (1.11) into Equation (1.8), the following equation is given:

$$0 = \frac{\partial \theta_l \overline{C_i}^l}{\partial t} + \nabla \cdot \theta_l \overline{j_i}^l + \frac{1}{V_0} \int_{S_{ls}} j_i \cdot n_{ls} dS + \theta_l \overline{r_i}^l \qquad (1.12)$$

The Nernst-Plank equation (1.4) is substituted into Equation (1.12):

$$\frac{\partial \theta_l \overline{C_i}^l}{\partial t} = \nabla \cdot \left(D_i \theta_l \left(\nabla \overline{C_i}^l + \frac{z_i F}{RT} \overline{C_i}^l \nabla \phi + \overline{C_i}^l \nabla (\ln \gamma_i) \right) \right) - \frac{1}{V_0} \int_{S_{ls}} j_i \cdot n_{ls} dS - \theta_l \overline{r_i}^l \qquad (1.13)$$

The integral can be considered with the following equation:

$$\frac{\partial \theta_s \overline{C_{s,i}}^s}{\partial t} = -\nabla \cdot \theta_s \overline{j_{s,i}}^s - \frac{1}{V_0} \int_{S_{ls}} j_{s,i} \cdot n_{ls} dS \qquad (1.14)$$

where, $C_{s,i}$ is the concentration of the species i that sorbed or exchanged on the surface of the solid matrix. There is no flux inside the solid matrix, such that only the flux at the solid/liquid interface remains. Substituting Equation (1.14) into Equation (1.13) gives:

$$\frac{\partial \theta_l \overline{C_i}^l}{\partial t} = \underbrace{\nabla \cdot \left(D_i \theta_l \nabla \overline{C_i}^l \right)}_{\text{diffusion}} + \underbrace{\nabla \cdot \left(\frac{D_i z_i F}{RT} \theta_l \overline{C_i}^l \nabla \phi \right)}_{\text{migration}}$$

$$\qquad (1.15)$$

$$+ \underbrace{\nabla \cdot \left(D_i \theta_l \overline{C_i}^l \nabla (\ln \gamma_i) \right)}_{\text{chemical activity}} + \underbrace{\frac{\partial \theta_s \overline{C_{s,i}}^s}{\partial t}}_{\substack{\text{chemical reactions} \\ \text{at solid/liquid interface}}} - \underbrace{\theta_l \overline{r_i}^l}_{\substack{\text{chemical reactions} \\ \text{in liquid (pore solution)}}}$$

where, each term of the equation describes the corresponding phenomena of ionic transport in cement-based materials, and the equation incorporates the moisture transport, reflecting the unsaturated condition that most concrete structures encounter. The first term on the right side of the above equation illustrates ionic diffusion induced by the spatial variation in the ionic concentrations. Since each ion with its own electric charge affects the movement of other ions, the migration is included in the second term. The third term reflects the effect of the ionic strength on the ionic dissolution in the pore fluid

using chemical activity. The fourth and fifth terms describe the chemical reactions. The former term includes the surface-sorption and ion-exchange occurring at the solid/liquid interface, and the latter illustrates the dissolution/precipitation inside the pore fluid. The electric field (V) in the above equation varies in terms of the spatial distribution of the ions. The electric field can be traced by the Poisson equation expressed as:

$$0 = \nabla^2 \phi + \frac{F}{\varepsilon} \sum z_i C_i \tag{1.16}$$

where, ε is the dielectric constant of the specimen. The numerical difficulty in solving a large number of F/ε can be overcome by reducing the element size in the finite element method (FEM). The values of F/ε have been validated by Krabbenhøft [22]. The diffusion coefficient (D_i) in Equation (1.15) provides information on the pore structure of the cement-based materials based on the following equation:

$$D_i^o = \tau D_i \tag{1.17}$$

where, τ is the tortuosity of the material, and D_i^o is a diffusion coefficient of the species i in free water. The percolated paths of the pore spaces contribute to the diffusion coefficient by determining how tortuous the paths are in the cement matrix.

The model described above was introduced by Kato [17] and was extended by Samson et al. [19-21]. This model was applied not only to describe the chloride ingress [4] and calcium leaching [24], but also to analyze the accelerated migration test, which is a test method to measure the ionic diffusivity of the cement-based materials. This model, known as the Nernst-Plank/Poisson equation, has significant potential to be employed in the simulation of other forms of deterioration, carbonation and decalcification, which are induced by the ionic transport of cement-based materials.

1.2.3. Moisture (Water) Transport

The volumetric fraction of the liquid (water) phase (θ_l) represents the moisture transport in cement-based materials. One simplified approach is the Richards equation [25] to simulate the mass transport of water in porous materials. Samson et al. [21] verified that the single value θ_l can determine the movement of both vapor and liquid water in cement-based materials. Richards proposed the following equation to illustrate water flow due to capillary suction:

$$\frac{\partial \theta_l}{\partial t} = \underbrace{\nabla \cdot \left(K \nabla \psi \right)}_{\text{suction}} + \underbrace{\frac{\partial K}{\partial z}}_{\text{gravity}} \tag{1.18}$$

where, K is the hydraulic conductivity, and ψ is the suction potential. The two terms on the right side of the equation represent the suction-driven and gravity-driven components

of flow. Here, the substitution of the hydraulic diffusivity, $D_\theta = K(d\psi/d\theta_l)$, makes the equation as follows:

$$\frac{\partial \theta_l}{\partial t} = \nabla \cdot \left(D_\theta \nabla \theta_l \right) + \cancel{\frac{\partial K}{\partial z}} \tag{1.19}$$

where, the hydraulic diffusivity, D_θ, is the nonlinear coefficient. Generally, the effects of gravity on moisture transport in cement-based materials have been neglected [26-28], because the suction-driven process might be much faster than the gravity-driven one [27]. To solve Equation (1.19), the relationship between the hydraulic diffusivity, D_θ, and the water content, θ_l, is required. Many formulae have been introduced to represent the hydraulic diffusivity, D_θ. Van Genuchten proposed the equation for soil-water [29], and Hall et al. [30], Lockington et al. [27], and Xi et al. [31] introduced the equation for cement-based materials. For example, Hall's equation is described as:

$$D_\theta = D_0 \exp\left(B\Theta \right) \tag{1.20}$$

where, D_0 and B are the experimentally determined parameters. B has a value between 6 and 8. Θ is the normalized water content defined as:

$$\Theta = \frac{\theta_l - \theta_d}{\theta_s - \theta_d} \tag{1.21}$$

where, θ_d is the dry moisture content (usually taken as zero), and θ_s is the saturated moisture content. These formulae to obtain the hydraulic diffusivity generally require further experimental confirmation to determine the empirical parameters.

1.2.4. Diffusivity and Hydration of Cement Paste

Cement paste is a porous material with a complex pore structure and solution. Free chloride ions from the saline environment dissolve in this pore solution and move through the pore structure. A model developed by Garboczi et al. determines the ionic diffusivity of cement pastes as a function of the pore structure. The following equation was derived and fitted to the data [32]:

$$\frac{D_t}{D_0}(\phi) = 0.001 + 0.07 \cdot \phi^2 + 1.8 \cdot H(\phi - 0.18) \cdot \left(\phi - 0.18 \right)^2 \tag{1.22}$$

where, D_t is a diffusion coefficient at time t, D_0 is a diffusion coefficient in free water, ϕ is the capillary porosity fraction, and H is the Heaviside function.

Cement particles undergo random growth due to hydration reactions, i.e., the pore structure's influence on chloride diffusivity varies with the degree of hydration of the

cement paste. Thus, based on Power's model for ordinary Portland cement pastes, the volume fraction of the total $[\phi(\alpha)]$ and water-filled $[\phi_w(\alpha)]$ capillary porosity and unhydrated cement $[\gamma(\alpha)]$ is highly dependent on the degree of hydration (α), and can be estimated as follows [33]:

$$\phi(\alpha) = \frac{\rho_{cem}(w/c) - f_{exp} \cdot \alpha}{1 + \rho_{cem} \cdot (w/c)} \tag{1.23}$$

$$\phi_w(\alpha) = \frac{\rho_{cem}(w/c) - (f_{exp} + \rho_{cem} \cdot CS)\alpha}{1 + \rho_{cem} \cdot (w/c)} \tag{1.24}$$

$$\gamma(\alpha) = \frac{1 - \alpha}{1 + \rho_{cem} \cdot (w/c)} \tag{1.25}$$

where (w/c) is the water-to-cement mass ratio, α is the degree of hydration of the cement at time t, ρ_{cem} is the specific gravity of the cement (here taken to be 3.2), f_{exp} is the volumetric expansion coefficient for the solid cement hydration products relative to the cement reacted (taken here to be 1.15 [33]), and CS is the chemical shrinkage. Under saturated conditions, the chemical shrinkage is assumed to be compensated for by the imbibition of external curing water ($CS = 0$) [34]. In that case, the total and water-filled porosities are identical.

After verification with experimental data, Bentz recently developed a model to describe the hydration kinetics of Portland cement based on spatial considerations [34]. In this model, the hydration rate has a first-order dependence on both the volume fractions of the available water-filled porosity and unhydrated cement-like bimolecular-type reactions. In terms of these phase fractions, the hydration rate is expressed as:

$$\frac{\partial \alpha}{\partial t} = k \cdot \phi_w(\alpha) \cdot \gamma(\alpha) \tag{1.26}$$

where k is the rate constant. Substituting Equation (1.24) and (1.25), the following analytical solution was obtained:

$$\alpha(t) = \frac{p\{\exp[R(1-p)t] - 1\}}{\{\exp[R(1-p)t] - p\}} \tag{1.27}$$

with $p = \rho_{cem}(w/c)/(f_{exp} + \rho_{cem}CS)$ and $R = k(f_{exp} + \rho_{cem}CS)/[1 + \rho_{cem}(w/c)]^2$. As shown above, the diffusivity of the cement-based materials varies with the maturity of the cement hydration. Therefore, when we consider long-term performance or early-age hydration, the hydration process is an important parameter that has to be involved. The models presented can be employed to estimate the ionic diffusion coefficient at time t.

1.2.5. Surface Treatments to Control the Ingress of Aggressive Ions

Treating the surface of concrete structures is one possible means of inhibiting this deterioration process and extending the service life of RC structures. As shown in Figure 1-2, there are many different types of surface treatments whose goal is to slow down the corrosion process by reducing chloride ingress: (a) coatings that form a distinct layer on the concrete surface (typically 300 μm to 1 mm thick); (b) pore blockers that penetrate percolated pores to a certain depth, solidifying to block the pores; (c) pore liners that penetrate into concrete pores, making the pore surface water repellent; and (d) sealers that form a physical film on the concrete surface, and that not only bond with the concrete surface but strengthen it as well. All types of surface treatments produce a distinguished pore structure within their settled region from the pore structure in concrete. An interfacial transition due to the distinct tortuosities may develop when two materials, which are the surface treatment and concrete having different pore structures, connect.
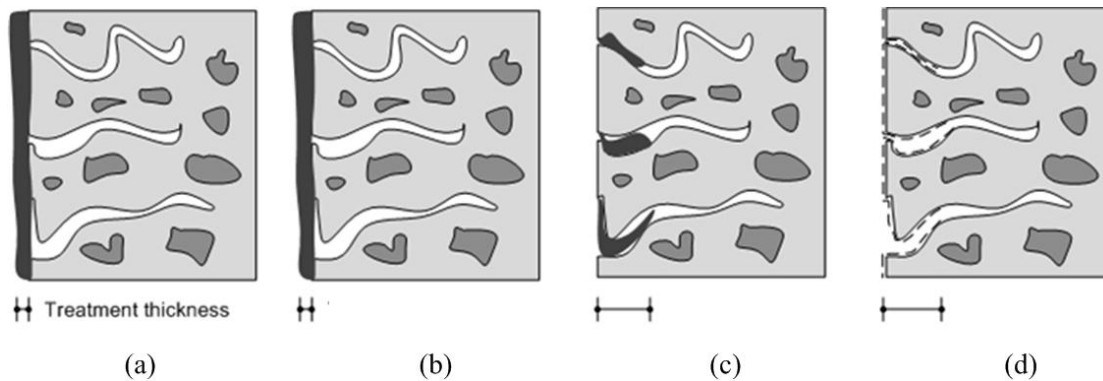
Figure 1-2. Surface treatment: (a) coating; (b) sealer; (c) pore blocker; and (d) pore liner (adapted from Refs. [35, 36]).

1.2.6. Adsorption of Chloride Ions by Cementitious Phases

In saline solution, the chloride ions are the most important element; they are abundant and affect the performance of the reinforced concrete by initiating corrosion. The chloride ions in saline solution interact with cementitious phases in various ways, at times causing phase transitions due to adsorption or ion exchange. Studies [4] have shown that binding mechanisms of chloride to the hydrated phases of Portland cement can be classified into two categories: (1) an interaction of sodium and chloride ions in the pore solution with calcium silicate hydrate (C-S-H) [37, 38]; and (2) a reaction between chloride ions and AFm phases [39, 40]. Since C-S-H comprises 50 ~ 60% of the volume of fully hydrated cement and acts as a primary binding phase in Portland cement, the long-term performance and durability of the C-S-H phase are key issues for the safety of concrete-based structures. Furthermore, monosulfoaluminate and hydroxyl-AFm serve as

an important "sink" for chloride ions.

Several recent studies have investigated the reaction of C-S-H with NaCl solution [41-47]. Viallis et al. [41] studied the structure of silicate tetrahedra and adsorbed sodium ions with solid-state NMR spectroscopy. Hill et al. [42] investigated the behavior of C-S-H in saline solution and the effect of the Ca/Si ratio, temperature, and cationic type on this behavior. Sugiyama [44, 45] also emphasized the importance of cationic interactions with C-S-H and successfully described the exchange reaction of sodium with calcium in C-S-H using a thermodynamic model. However, most studies to date have not considered the significance of anionic interaction with C-S-H when the cement-based materials come into contact with sodium chloride solutions. Ramachandran [37] suggested the following three possible mechanisms of chloride ion interactions with C-S-H: (1) chemisorptions of the chloride layer on the surface of C-S-H; (2) penetration of chloride into the C-S-H interlayer space; and (3) incorporation and precipitation of chloride within the C-S-H lattice.

In their structure, AFm phases consist of a positively charged main layer $[Ca_2Al(OH)_6]^+$ and negatively charged interlayer $[X \cdot nH_2O]^-$ or $^{2-}$ where X can be either a monovalent or a divalent anion. Recent studies suggest that Friedel's salt formation is the result of chloride reacting with the AFm phases [40, 48, 49]. The previously reported NMR study indicates that dissolution/precipitation and ion exchanges are the main mechanisms in the formation of Friedel's salt by adsorbing chloride ions [40]. In ion exchange, anions are released into the pore solution due to chloride binding by the AFm phases.

$$[R-X]+Cl^- \leftrightarrow [R-Cl]+X^- \text{ or } \tfrac{1}{2}X^{2-} \qquad (1.28)$$
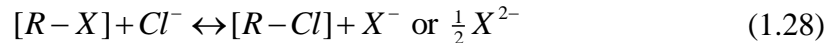
where R indicates the ion exchange sites. However, a chloro-sulfate AFm phase, known as Kuzel's salt, has also been identified [49-51]. Based on XRD analysis, Hirao et al. suggested the possibility of precipitation of the AFt phases under a low concentration of chloride [51].

1.3. Research Gaps in the Literature and the Focus of the Dissertation

The previous section in this chapter presented a literature review on ionic and moisture transport and chloride adsorption in cement-based materials. Despite the current state-of-the-art studies of this subject, there are still gaps in the research. By identifying these gaps, we can point to directions for future research. Therefore, our main objective in this section is to outline the research gaps in the literature and to introduce research goals that will fill some of those gaps in this thesis.

1.3.1. Research Gaps in Transport Simulation at the Nano-Scale

MD simulations can be applied to understand the transport phenomena of cementitious phases at the nano-scale. The most important phase among the hydrated cementitious phases is calcium silicate hydrate (C-S-H) as a binder. Because of their similar structure [5], 14 Å tobermorite is often used as one of the structural models for C-S-H (I). With its layered structure consisting of CaO_7 polyhedra and SiO_2 tetrahedra, the interlayer space of 14 Å tobermorite can accommodate a significant amount of water [52]. Therefore, detailed knowledge of the water transport of 14 Å tobermorite may provide insight into creep or shrinkage related to the water movement of C-S-H (I).

Megaw et al. were the first to investigate the crystal structure of tobermorite [53]. Three structures of tobermorite phases have been reported according to their different basal spacing : (1) water-free 9 Å tobermorite (riversideite, $Ca_5Si_6O_{16}(OH)_2$) [54, 55]; (2) 11 Å tobermorite ($Ca_{5-x}Si_6O_{17-2x}(OH)_{2x} \cdot 5H_2O$) [54, 56]; and (3) 14 Å tobermorite (plombierite, $Ca_5Si_6O_{16}(OH)_2 \cdot 7H_2O$) [52]. Recently, Bonaccorsi et al. refined the crystal structure of 14 Å tobermorite using synchrotron radiation X-ray diffraction (XRD) [52]. Therefore, the detailed structural and transport properties of water molecules in the interlayer space of 14 Å tobermorite need to be studied. Because XRD techniques cannot observe hydrogen atoms [57], MD simulations can give detailed information on structural positions and self-diffusion coefficients of the interlayer water in 14 Å tobermorite. Therefore, using MD simulations, Chapter 3 demonstrates the trajectory of the water molecules through the interlayer space of 14 Å tobermorite. This trajectory provides insight on their structural properties and mobility through the interlayer space. This study compares the water transport through the interlayer space with the transport on the surface of 14 Å tobermorite.

1.3.2. Research Gaps in Chloride Interactions with Cementitious Phases

Because no long-range order exists in C-S-H structures and most of the phases formed in saline solution are complex, currently available experimental techniques can only give a general indication of its nanostructure. In other words, more advanced experimental tools are necessary to understand the effects of chloride on the structure of C-S-H. In the case of the AFm phase, the adsorption process of chloride ions by monosulfoaluminate includes many different types of phase transitions. Since a phase transition often discontinuously occurs in a specific external condition, it is possible that the continuous adsorption isotherms, like Freundlich and Langmuir isotherms, cannot represent the adsorption process of chloride ions by monosulfoaluminate. That is, understanding the phase change that occurs by chloride binding is critical in determining the chloride adsorption isotherms. X-ray spectroscopies allow us to quantify the phase assemblage and observe its morphology. Therefore, using these experimental techniques, Chapter 4 investigates how the adsorption processes of sodium and chloride ions   affect the phase change of monosulfoaluminate and the polymerization of C-S-H. In other words, the study shows how the C-S-H phases, depending on their Ca/Si ratio, determine

whether they adsorb the sodium or chloride ion. Furthermore, it examines the phase changes of monosulfoalumiante while increasing the NaCl concentration in aqueous solution.

1.3.3. Research Gaps in the Effects of Surface Treatments

Previous studies have clearly demonstrated that surface treatments improve the durability performance of RC structures [36, 58-68]. Some of these studies have based their findings on using Rapid Chloride Permeability Test (RCPT) to measure the effective ionic diffusivity of surface-treated concrete samples [36, 66, 68]. Currently, it is not feasible to measure the electric field inside a pore solution and the corresponding ionic profile as a function of time. Nevertheless, such information is crucial to understand and accurately measure the effective chloride diffusivities of surface-treated concrete because surface-treated concrete, as a composite material, might reveal more complicated and dynamic processes than bulk concrete in ionic transport. According to a previous study, the conventional single-species model homogenized the diffusivities of concrete and surface treatment, suggesting a pseudo-diffusion coefficient to the surface-treated concrete specimen [69], and Zhang et al. suggested a simple model to describe chloride diffusion into surface-treated concrete [70]. Their conventional single-species model disregards electro-neutrality combined with the absence of the migration term, which is known to be problematic in describing the ionic contents of concrete samples during RCPT [22]. Clearly a more sophisticated model for simulating surface-treated concrete is required since there is still no appropriate model that accurately simulates surface-treated concrete. Therefore, the influence of the surface protection on ionic movement still needs to be researched futher. A numerical model is developed to show the effect of the surface treatment on ionic transport, and then validated with RCPT experiments in Chapter 5. Based on this model, Chapter 5 demonstrates the ionic transport and electric field through the surface-treated concrete, which differ from those through untreated concrete.

1.3.4. Research Gaps in Absorbent of Chloride Ions

Steel bars embedded in concrete are normally protected by a passive film formed by a thin iron oxide layer on the steel surface, which remains stable in the high-alkaline environment of the cement-based materials. Corrosion can be initiated when this protective film is depassivated by a chloride attack in saline environments, such as de-icing salts, unwashed sea sand, and seawater [71, 72]. The chloride-induced corrosion of steel reinforcing bars usually affects the performance of reinforced concrete (RC) structures, and may result in major deterioration of the structure [3]. To address this issue, many protecting inhibitors against chloride attacks have been developed. They can be classified according to their application methods as follows: (1) added to fresh concrete as an admixture; and (2) applied on the surface of hardened concrete or the steel reinforcing bars [73]. Many materials, such as sodium nitrite and aminoalcohol, have

been used as admixed or surface-applied inhibitors against corrosion in reinforced concrete [74, 75]. Such inhibitors usually cover the anodic or cathodic sites of the steel bars to prevent chloride attacks. A more effective and direct approach would be to find an effective chloride absorbent that works in the cementitious environment.

Because of their high anion exchange capacities, there is increasing interest in the application of layered double hydroxides (LDHs) to concrete technology. Hydrotalcite or LDH-like phases found in hydrated slag cement have been found to increase the binding capacity of chloride ions [76, 77]. Tatematsu et al. [78] admixed a hydrocalumite-like material to cement mixtures as a salt adsorbent, and Raki et al. [79] showed that LDH-like materials admixed in concrete can control the release rate of organic admixtures. Furthermore, several methods have been developed to utilize LDH-like phases in the construction industry [80-85], including hydrocalumite- or hydrotalcite-based admixtures to capture chloride. The thermal decomposition of Mg/Al-CO$_3$ LDH at around 500 °C results in Mg/Al oxides, which increase the binding capacity of anions with reforming hydrotalcite structures [86, 87]. For this reason, calcined layered double hydroxide (CLDH) has been employed as a chloride absorbent in aqueous solution [88, 89], as expressed by the following equation:

$$Mg_{1-x}Al_xO_{1+x/2} + x \cdot Cl^- + (m+1+x/2)H_2O \rightarrow Mg_{1-x}Al_x(OH)_2Cl_x \cdot mH_2O + x \cdot OH^-$$

(1.29)
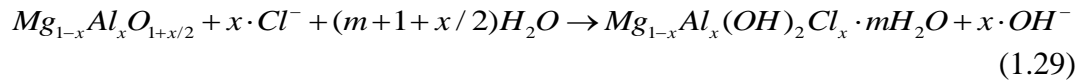
Therefore, this CLDH may have the potential to be an effective adsorbent for chloride ions in the cement matrix. Although the chloride uptake by CLDH has been carefully investigated in aqueous solutions, the investigation of its adsorption in cementitious materials has not been studied in depth. For this reason, a detailed study of the effect of the cementitious environment on chloride adsorption by CLDH is both necessary and long overdue. Chapter 6 evaluates the feasibility of using CLDH as a chloride adsorbent in hardened cement paste. Equilibrium and kinetic isotherms in the cement paste and dominant parameters in the adsorption process were determined. Furthermore, X-ray based techniques were applied to observe the structural change and morphology of CLDH. This finding determines whether or not CLDH has the extraordinary potential to prevent chloride-induced deterioration of reinforced concrete. Chapter 2 briefly introduces the simulation and experimental techniques used in the following chapters; Chapters 3 to 6 present our research contributions to the research gaps; and, finally, the summary and conclusions of this thesis are provided in Chapter 7.

Chapter 2.

Simulation and Experimental Techniques

This chapter introduces the simulation and experimental techniques that will be employed in Chapters 3 to 6. Each technique is a vast research subject and applied to a variety of research fields. Though an in-depth description of each technique is beyond the scope of this thesis, it is worthwhile to provide a brief description of the techniques. For this reason, this chapter will focus on aspects that are related to this thesis.

2.1. Molecular Dynamics

Computer simulations play an important role in understanding the structural and dynamic properties of molecules and ions as well as the microscopic interactions between them. One of the main techniques for simulation is molecular dynamics (MD). MD simulations are capable of providing complementary information to experimental limitations so that we may perform MD simulations on the computer that are difficult to measure in the laboratory. Furthermore, MD simulations act as a link between atomic properties and microscopic measurements in the laboratory. In MD simulations, sequential configurations of the simulation system are produced by integrating Newton's laws of motion, and the results show a trajectory defining how the positions and velocities of atoms in the simulation cell alter over time. The trajectory can be obtained by solving the differential equations derived from Newton's second law. MD simulation is solved by the numerical, step by step, analysis of the classical equations of motion.

MD simulations have been used to obtain complementary information on water molecules existing in the interlayer structure of mineral phases. In the mineral research related to cement, Churakov has described the structure and dynamics in the interlayer of 11 Å tobermorite based on ab-initio molecular dynamics simulations [90, 91]. Because of the long duration of the simulations and limited computational resources, Churakov emphasized the need to develop a classical force field model to reproduce dynamic and structural properties of hydrated phases. Recently, the CLAYFF force field model for clay phases [92], of which a more detailed description will be given in Chapter 3, was successively applied to study the structure of water molecules on the surface of tobermorite as well as to understand chloride sorption on the surface of cementitious phases. These applications have been led by Kalinichev et al. [46, 93]. The authors investigated the interfacial reactions of portlandite, Friedel's salt, ettringite, and tobermorite, and compared ionic diffusion coefficients for chloride on the surface sites to those in bulk solution. They found two different regions, which have distinct diffusivities, called the inner and outer-sphere surface complexes. According to their MD simulations, the chloride binding capacity on the surface of the cementitious phases decreases in the sequence Friedel's salt > portlandite > ettringite > tobermorite.

2.2. Finite Element Method (FEM)

Finite element method (FEM), also known as finite element analysis (FEA), is a numerical procedure used to solve complex partial differential or integral equations, of which the analytical solution cannot be determined. Its applications generally extend to continuum mechanics, heat or mass transfer, electromagnetic problems (design of micro-electromechanical system, MEMS), and structural analysis. The basic idea of the FEM is simply to generate a mesh by dividing a target object into a number of elements and then to solve each element with a weak form. There are various methods to obtain the weak form from the governing equation (strong form), such as the collocation method, the least square method, and the Galerkin method. The FEM is generally a special case of the Galerkin method.

In a 1-D element, the sum of the two trial functions is capable of expressing the linearly approximate solution over the element. The approximate solution can be presented in terms of nodal values of the element as f_1 and f_2:

$$\overline{f}(x_e) = \left(1 - \frac{x_e}{L_e}\right)f_1 + \left(\frac{x_e}{L_e}\right)f_2 \tag{2.1}$$

where, L_e is the element length. This approximate solution can be defined as row and column vectors:

$$\overline{f}(x_e) = \left[\left(1 - \frac{x_e}{L_e}\right) \quad \left(\frac{x_e}{L_e}\right)\right]\begin{bmatrix} f_1 \\ f_2 \end{bmatrix} = [N][f_e] \tag{2.2}$$

where *[N]* is named as *shape function*, and the derivatives of the shape function are notated by *[B]* as follows:

$$[B] = \frac{d}{dx_e}[N] = \left[\left(-\frac{1}{L_e}\right) \quad \left(\frac{1}{L_e}\right)\right] \tag{2.3}$$

This basic concept can be extended to the 2-D and 3-D objects and various shapes of the element (generally triangular or rectangular element). Recently, element-free Galerkin methods, based on particle methods, have been developed to consider the object that is not a continuum, but rather a set of particles in the fields, such as astrophysics, solid state physics, and biochemistry [94]. However, in this thesis, we will focus on the classic FEM with the notations mentioned above to solve the extended Nernst-Plank/Poisson equation.

The NPP model is considerably more complicated than the conventional single-species model. Generally, a numerical scheme is necessary to compute the NPP equation. The numerical solution of the NPP equation was developed in 1995 by Kato, M. who used the finite-difference method (FDM) for steady-state cases [17]. As the NPP equation

16

has been extended to include chemical activity, convection, partial saturation, and other processes, the FEM has been demonstrated to be more preferable than the FDM because the FEM makes the numerical procedure simpler than the FDM in the extended NPP equation. In the FEM procedure, coupled and uncoupled algorithms have been proposed to solve the NPP equation [18]. The coupled algorithm has an advantage over the number of elements in convergence, but it deals with larger sized matrices than an uncoupled one and requires a classical Newton-Raphson method to solve the non-linear set of the weak form for each time step. Both algorithms will be discussed further in Chapter 5.

2.3. Scanning Transmission X-ray Microscopy (STXM) and X-ray Absorption Near Edge Spectroscopy (XANES)

Synchrotron-based scanning transmission X-ray microscopy (STXM) is one of the few tools providing information on morphology and spectroscopic speciation for samples [95-98]. The zone plate focuses monochromatic X-rays, and the spatial resolution depends on the coherence of the x-ray radiation incident and the quality of the zone plate. The spatial resolution of up to 30 nm pixel sizes can generally be achieved with STXM. As significant levels of higher-order diffracted light involved in the X-ray incident can disturb the spatial resolution and the quality of spectra, an order sorting aperture (OSA) having a 40 ~ 60 µm pin hole is applied to eliminate higher-order diffracted light, leaving only first-order diffracted light. For this reason, the correct calibration of OSA is important to maintain the quality of images and spectra obtained from STXM. The sample is held on a set of piezo fine stages, which is mounted onto a set of coarse stages. Since multiple samples can be installed on a sample holder, the coarse stages move the targeted sample to the proper position. The fine stages are used for the majority of data acquisition by moving the sample to the accurate position. A STXM image is obtained at a given photon energy by raster scanning the sample. A sequence of images with a stepwise increment in photon energy represents spatially resolved spectral information. This sequence of images is referred to as a "stack." Advanced Light Source (ALS) offers a wide energy range in the soft X-ray energy region. Furthermore, this stack becomes a source to extract the X-ray absorption near edge spectroscopy (XANES).

In XANES, the interactions of photons with matter are studied by measuring the photo-absorption energy. By using X-ray radiation, a core electron of the atom can be taken out of its core-level and excited to unoccupied bound or continuum states. When the X-ray incident excites the atom and the photon energy is sufficiently large, the photoelectric effect results in the step-like shape of the absorption spectrum, and the photo-absorption energy due to the excitation is called the "absorption edge." The energy of the bound atom depends on the positions and types of its neighbors and differs from the speciation of the bound atom. When increases in the photon energy are limited to near the adsorption edge, the photoelectron can occupy either unoccupied bound or low-lying continuum states. This part of the spectrum is called the XANES region. In the

XANES region, the scattering on the neighboring atoms is strong, so that the photoelectron acts as a very sensitive probe that can recognize the charge distribution and the arrangement of the neighboring atoms around the absorbing atom [99].

STXM and XANES enable the characterization of complex cement phases. Ha et al. used these techniques to investigate the effects of organic polymers on structures of the C-S-H phase [98]. Their study shows that Si K-edge XANES spectra of STXM images can serve as fingerprints of local structural variations in tetrahedral silicate chains of the C-S-H phase as Si K-edge generally shifts to higher energy in its absorption edge with an increase in the silicate polymerization. Using STXM, they also successfully observed that a strong spatial correlation between Ca and C absorption XANES spectra can identify the adsorbed sites of organic polymers in the interlayered structure of the C-S-H phase. This previous study shows that STXM can resolve both the spatial resolution and speciation limitation problems that arise in lab-based experiments, like Nuclear Magnetic Resonance. In this thesis, these techniques are applied to study the interactions between cementitious phases and NaCl and these are discussed further in Chapter 4.

2.4. Rapid Chloride Permeability Test (RCPT)

RCPT is used to evaluate material resistance to chloride ion ingress. In a common approach, chloride ions are forced into a concrete specimen through the induction of an external voltage on the specimen surface. In this process, several standard tests are performed that measure various different parameters: AASHTO T277 [100] and ASTM C1202-10 [101] measure charges passed in coulombs for determining chloride permeability, and NT Build 492 (Nordic Standards) [102] measures an average chloride penetration depth from which a diffusion coefficient is calculated. NT Build 492 is often referred to as the rapid migration test (RMT) due to the relatively different configuration of the experimental setup.

The basic concept and minor modifications can be applied in the RCPT setup. When surface treatments are applied to concrete specimen, the schematic presentation of RCPT is illustrated in Figure 2-1. For this experiment, the protective material was applied on only one side of circular surfaces of the cylindrical cementitious specimen, which is in contact with a cathode cell. Generally, the specimen was maintained in a saturated condition during RCPT, because previously it was vacuum-saturated for 24 hours. In the common standard tests, the cathode cell is filled with 3.0 % NaCl aqueous solution and the anode cell with 0.3 N NaOH aqueous solution. Recent studies show that adding 0.3 N NaOH solution into the cathode cell to prevent a pH imbalance between the two cells improves the results [22, 103]. After RCPT, the cylinder specimen was split and sprayed with 0.1N silver nitrate solution; this was done to examine the chloride penetration depth through the specimen, see Refs [36, 104]. Since chloride penetration measurements are insensitive to concrete pore solution conductivity and less dependent on testing variations than the charge measurements, such modification does not change

the property of materials; instead, it actually improves detection sensitivity [105].
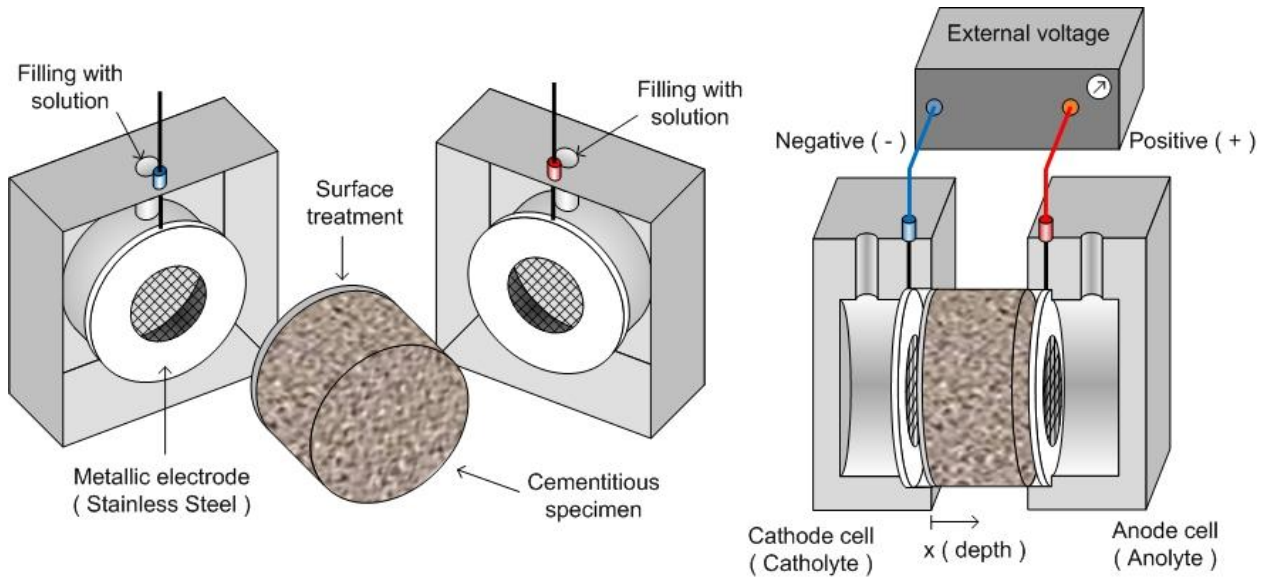
Figure 2-1.Cell-face view and test arrangement of RCPT.

Chapter 3.

Structure and Transport of Water Molecules in Interlayer of 14 Å Tobermorite

The major constituents of Portland cement are calcium silicate and aluminates, which react with water to produce a hard mass. The calcium silicate hydrate (C-S-H) phases among the hydration products constitute 50~60 % of volume of fully hydrated solid, and they are the principal binding phases in concrete. In spite of the importance of the C-S-H phases, their exact composition and atomic structure is still unclear for the following reasons. First, the C-S-H phases in hydrated cement are amorphous or nano-crystalline as mentioned in Chapter 1. Second, the large variations in the composition and nanostructure of the C-S-H phases are caused by factors such as the water-to-cement ratio, the curing temperature, and the degree of hydration. For this reason, most research on the C-S-H phases usually starts with a model compound having a crystalline structure. Tobermorite, which is crystalline, has been used predominantly as the basic structure to model the C-S-H phases of hydrated cement due to the structural similarity between tobermorite and the C-S-H phases. Moreover, Taylor referred to the C-S-H phase as a structurally imperfect form of 14 Å tobermorite [5]. Therefore, we are able to understand the material properties of the C-S-H phases based on those of 14 Å tobermorite. The C-S-H phases and 14 Å tobermorite have an interlayer space containing a significant amount of water. Structure and transport of the interlayer water can affect not only the mechanical property but also the creep and shrinkage of concrete. This is because the interlayer water moves, and the C-S-H phases are more likely to be dehydrated under pressure or dry conditions.

Since XRD techniques cannot detect the hydrogen atom, the molecular dynamics (MD) simulation provides complementary information on the interlayer water of 14 Å tobermorite based on its refined structure. The MD simulation requires an empirical force field. Recently, CLAYFF was developed for the MD simulation of hydrated and multicomponent mineral systems [92]. In the CLAYFF, its interatomic potentials were derived from structural and spectroscopic data for a variety of simple hydrated compounds, and the parameters of the Lennard-Jones function and Coulombic energy were derived by Mulliken and the electro-static potential analysis of density function theory. As mentioned in Chapter 2, CLAYFF has shown good results when applied to MD simulations to describe the structure and behavior of intercalated water in 14 Å tobermorite. In this chapter, MD simulations with CLAYFF were performed to investigate the detailed structural positions and transport of water molecules in the interlayer of 14 Å tobermorite. In natural samples of 14 Å tobermorite, Ca cations and water molecules in the interlayer space can occupy available sites in an infinite number of ways. The study by Bonaccorsi et al. [52] proposed an ordered distribution, and the

simulation conducted here assumed this ordered distribution. To compare the simulation results with the reported data of the refined structure from XRD, radial distribution functions (RDF) were constructed from the MD simulations. Based on the MD simulation results, density profiles and velocity autocorrelation functions were investigated, and detailed information on structural positions and self-diffusion coefficients of the interlayer water in 14 Å tobermorite was studied.

3.1. Computational Procedure

In this chapter, the molecular modeling is based on the use of the CLAYFF force-field model [92], which has been successfully applied previously to cement materials and surface binding of tobermorite [46, 93, 106]. The employed water model is the flexible version of the simple point charge (SPC) water model [107, 108]. This water model has been used to describe successfully the structure and properties of water [109, 110] and interactions with cementitious phases [46, 93, 106]. The potential interaction energy U is the sum of an electrostatic Coulomb potential between atomic charges and a Lennard-Jones potential (12-6) caused by the short-range van der Waals interactions.

$$U = \sum_{i,j}^{i \neq j} \left[\frac{q_i q_j}{4\pi\varepsilon_0 r_{ij}} + 4\varepsilon_{ij} \left\{ \left(\frac{\sigma_{ij}}{r_{ij}} \right)^{12} - \left(\frac{\sigma_{ij}}{r_{ij}} \right)^6 \right\} \right] \tag{3.1}$$

where q_i and q_j are the effective point charges of atoms i and j, r_{ij} is the distance between those atoms, ε_0 is the electric constant (8.854×10^{-12} F/m), and ε_{ij} and σ_{ij} are parameters of the Lennard-Jones potential. The Lennard-Jones parameters for the interactions between different elements were obtained by arithmetic mean and geometric mean [111].

$$\sigma_{12} = \sigma_{21} = \frac{\sigma_{11} + \sigma_{22}}{2} \ \ (arithmetic) \qquad \varepsilon_{12} = \varepsilon_{21} = \sqrt{\varepsilon_{11}\varepsilon_{22}} \ \ (geometric) \tag{3.2}$$

The model structure was based on the crystal structure of 14 Å tobermorite refined by Bonaccorsi et al. from synchrotron XRD and order-disorder theory. This structure presents an ordered distribution of zeolitic calcium cations and water molecules in the interlayer space, as shown in Figure 3-1. Water molecules W1, W2, and W3 surround a calcium cation so that they form a $Ca(H_2O)_4O_2$ octahedron with two O5 oxygen atoms of bridging tetrahedra. According to the proposed ordered distribution, these Ca-centered octahedra and W4 water molecules alternately occupy the location between two neighbor O5 oxygen atoms. This structural configuration was applied to the MD simulations.

The 14 Å tobermorite has been refined previously in a monoclinic unit cell with the space group *B11b*. Thus, the monoclinic cell was used for the initial configuration, but the simulation supercell was converted to orthorhombic *P1* symmetry. Based on the

configuration of the ordered scheme, water molecules and calcium cations in the interlayer of 14 Å tobermorite were initially arranged, and the other intra-structure atoms—except water molecules—were kept fixed at their crystallographic positions during the MD simulations. The periodic supercell for MD simulations consisted of 4×4×1 simulation cells in a, b, and c directions, respectively.

The MD calculations were carried out using the large-scale atomic / molecular massively parallel simulator (LAMMPS) [112]. The energy of the model system in energy minimization was allowed to converge to its minimum within 0.005 kcal/mole of the relative root mean square fluctuations, and then this optimized structure (see Figure 3-2) was employed in the starting configuration for further simulations of the Hoover NVT (canonical) ensemble with a time step of 0.5 fs. Given a set of coordinates, the atom velocities were randomly assigned from a Maxwell-Boltzmann distribution at a fixed temperature. The classical atomic motion equations were integrated with the Verlet algorithm, and a cut-off radius of 6.0 Å was used for the Lennard-Jones interactions. To observe the effects of temperature, the temperatures were set to 100 and 300 K. The system was allowed to relax and equilibrate for 100 ps. Interlayer molecular configurations were stored every 5 fs after the relaxation time, and the simulation time was extended to 100 ps. Structural properties and dynamic properties were calculated from the MD trajectory after the relaxation time.

3.2. Results and Discussion

3.2.1. MD Simulations versus XRD Refinement

Atomic distances of 14 Å tobermorite obtained from MD simulations were compared with the refined structure reported by Bonaccorsi et al. [52]. The calcium cation strongly interacts with water molecules in the interlayer space. Four water molecules, which are W2, W3, and two W1s in Figure 3-1, are strongly bonded to the calcium cation; therefore, the water molecules are the nearest neighbors of the calcium cation. Based on the reported bond distances in the refined structure, Ca-W1 bond distances range from 2.4 to 2.6 Å, and Ca-W2 and Ca-W3 bond distances are 2.4 Å, and the distances of Ca-W4 and Ca-W6 are respectively 3.86 Å and 4.75 Å. Analysis of the radial distribution function (RDF) between calcium cations and water molecules allows for comparison of the atomic distances between the MD simulations reported herein and the existing structure refinement.

Figure 3-3 presents the computed Ca-O_w RDF at 100 and 300 K. The first peak in Figure 3-3 is at a distance of 2.5 Å, corresponding to the bond distances between W1, W2, and W3 water molecules and the calcium cation. The peaks below the second and third arrows in Figure 3-3 correspond to the distances between the calcium cation and the W4 and W6 water molecules, respectively, and their values are 3.8 and 4.8 Å, which are similar to the atomic distance reported by Bonaccorsi et al. [52]. The structural distances

of atoms obtained by the MD simulations are in good agreement with the XRD refinement. Their differences are small enough to be caused by the experimental uncertainties and approximated procedures in simulations. The three peaks below the arrows in Figure 3-3 indicate the nearest water molecules of the centered calcium cation in the interlayer of 14 Å tobermorite have stronger intensity and narrower peak width than the other peaks. Despite the higher temperature (300 K), those three peaks remain strong, implying that the water molecules in the interlayer of 14 Å tobermorite maintain octahedral structure with the calcium cation at 300 K. Because an exact determination of the oxygen and hydrogen positions in water molecules by experimentation is complicated due to the invisibility of protons to X-rays, more detailed positions of oxygen and hydrogen and dynamics in the interlayer water from the MD trajectory will be discussed in the next section.

3.2.2. Structure and Mobility of Water Molecules

The MD trajectory converts into the time-averaged atomic density maps in Figure 3-4 and the density profiles along the *c*-axis in Figure 3-5, which enable to provide better understanding of structure and mobility of water molecules. In the W1 water molecule—one of the nearest neighbors of the calcium cations—its oxygen atom is mainly attracted by the calcium cation. In other words, the W1 water molecule interacts so strongly with the calcium cation that its oxygen atom is attracted to and oriented towards its closest calcium cation. In Figure 3-4, the "W1"s indicate the W1 water molecules. The high-density zone in its center indicates the spatial distribution of the oxygen atom of the W1 water molecule in the *ab*-plane; the two high-density zones next to the center are hydrogen atoms. Almost directly located in a line, these two cases infer that the H-H and oxygen atoms of the W1 water molecule, respectively, orient up and down along the *c*-axis, or they have opposite orientations. As Figure 3-5 (W1) shows the spatial distribution of its H-H and oxygen atoms along the *c*-axis, the former case corresponds with the upper W1 water molecule, while the latter case does with the lower W1 water molecule. This W1's structure can be understood from its neighbors in Figure 3-4 and Figure 3-5. Since one of the hydrogen atoms of the W1 water molecule is close to the oxygen atom of the W6 water molecule, they form a hydrogen bond. Furthermore, the other hydrogen atom of the W1 water molecule forms a hydrogen bond with the bridging oxygen of the pairing silica tetrahedron.

The density profiles along the *c*-axis for the W2 water molecule at temperatures of 100 and 300 K are presented in Figure 3-5 (W2). The W2 water molecule can occupy two adjacent sites at the lower temperature. The first site is located in the middle of the interlayer along the *c*-axis. Here, its oxygen atom orients toward the calcium cation, and the two hydrogen atoms maintain balanced interactions between the two O5 oxygen atoms of the bridging tetrahedra. The second site then moves to a lower location, making the hydrogen bond with the oxygen atom of the W1 water molecule. As shown in Figure 3-4(b) and Figure 3-5(b, W2), at T = 300 K, the W2 water molecules are able to jump

between the upper and lower W1 water molecules, due to sufficient kinetic energy. Only one density group of the W2 water molecule due to adjacent sites is shown in Figure 3-4(a), whereas in Figure 3-4(b), two groups have moved up. In fact, at T = 300 K, a small peak at the center of the c-axis still appears in Figure 3-5(b). Thus, this site is more likely to provide a geometry that locally minimizes the energy of the model system. The orientation of the oxygen atom in the W2 water molecule is directed toward the closest calcium cation without regard to the locations of occupied sites.

Because the W3 and W4 water molecules strongly interact with each other, their structural properties have to be described together. The W3 water molecule is strongly bonded to the nearest calcium cation, and the W4 molecule is firmly constrained by two O5 oxygen atoms by forming hydrogen bonds. These interactions dominate the orientations of the oxygen atom of the W3 water molecule and the hydrogen atoms of the W4 water molecule. As shown in Figure 3-4, three obvious zones of high densities are positioned around an indicator marked as W4. Based on Figure 3-5(b, W4), the centered high-density zone among the three is the oxygen atom of the W4 water molecule, and the other two spots are its hydrogen atoms. Their concentrations of atomic density in Figure 3-4 and Figure 3-5(W4) are intense, regardless of the temperature. In other words, the W4 water molecule is strongly constrained. Although it has two sub-positions at a low temperature (T=100 K), in Figure 3-5(a, W4), their distance is small, and the sub-positions are merged as the temperature increases and results in a broadening of peaks in Figure 3-5(b, W4). In Figure 3-4, two sites with high densities are shown next to the marked W3. The spot closest to the W4 water molecule is a position for hydrogen atoms of the W3 water molecule. Because the sites of the hydrogen and oxygen atoms are overlapped from the viewpoint of [001], only one site for them is presented in Figure 3-4. Depending on which hydrogen of the W3 water molecule forms the hydrogen bond with the W4 water molecule, the W3 molecule can occupy an upper or lower site along the c-axis in Figure 3-5(W3).

As mentioned before, the W6 water molecule forms one hydrogen bond with the W1 water molecule and does the other with the oxygen of the pairing silica tetrahedra. Because it has more available space than the other water molecules, its movement is more active and extensive than the others. For this reason, Figure 3-5(W6) shows the movement of the W6 water molecule, of which the peak widths are broad. A snapshot of the interlayer water during the MD simulation is presented in Figure 3-6; to clarify the positions of the water molecules, only one of the two pairs are shown by making other molecules invisible. Figure 3-6 clearly shows both the structure of the water molecules within the interlayer space. One of configurations of the water molecules are listed in Table 3-1.

3.2.3. Self-Diffusion Coefficient of Water Molecules

One of the important properties of the water molecules within the interlayer of tobermorite and C-S-H phases is the self-diffusion. Water transport through the interlayer

spaces of C-S-H occurs and controls creep and shrinkage [113]. In the present study, because of the relatively short time-span of the MD simulations and the low mobility of the interlayer water, the self-diffusion coefficients for the interlayer water are estimated from an integral of the velocity autocorrelation function, known as the Green-Kubo formula [114-116].

$$D = \frac{1}{3}\int_0^\infty dt \left\langle v(0) \cdot v(t) \right\rangle \tag{3.3}$$

where v is the velocity vector of the water molecule. The calculated coefficients are listed in Table 3-2. The values can be varied according to the distribution of Ca cations and interlayer ions in the natural samples. In addition, defects in tobermorite structure [90, 117] can alter the dynamic property of water molecules in the interlayer. However, the obtained values can still provide information on the scale of the coefficients compared to the diffusion coefficients of the surface-associated water molecules.

The reported diffusion coefficients for inner and outer surface water molecules of tobermorite are also presented in Table 3-2 [93, 118]. The diffusion coefficient of the interlayer water molecules is roughly equal to that of inner surface water at room temperature. Even if the movement of the water molecule is restricted by the interlayer structure, the MD simulation shows the presence of slow diffusion of the water molecule through the interlayer space that might be one reason for shrinkage or creep in cement materials. Therefore, the self-diffusion coefficient of interlayer water of 14 Å tobermorite presented in this chapter provides fundamental information on water transport in the interlayer space of C-S-H. This information is necessary for further simulation studies—such as conducting a Kinetic Monte Carlo (KMC) simulation—to study the molecular scale creep and shrinkage caused by the interlayer water of C-S-H.

3.3. Conclusion

Through the use of molecular dynamics, the structure and mobility of the interlayer water molecules in 14 Å tobermorite was investigated. The MD simulated structure was found to be in good agreement with the existing data. In the structure of the water molecules, the W1, W2, and W3 water molecules, strongly bonded by the calcium cation in interlayer spaces, maintained similar distances from the calcium, with their oxygen facing the calcium. The orientation of their hydrogen was governed by hydrogen bonds with other water molecules or oxygen atoms of silica tetrahedra. In their mobility, the W2 water molecule jumped between upper and lower sites to form a hydrogen bond with the W1 water molecule at T = 300 K. The W4 water molecule was strongly constrained by the O5 oxygen of the bridging tetrahedra. The motion of the W3 water molecule was limited by the W4 molecule, due to the strong hydrogen bond between them. The W6 water molecule moved more actively than the others, owing to weak interactions with other atoms and because it had space to move. One of configurations of the interlayer water was proposed based on the trajectory of the MD. Moreover, the self-

diffusion coefficients of water molecules in the interlayer were calculated from the velocity autocorrelation function. Although its value was smaller compared to that of the interface, their orders of magnitude were identical, suggesting that the water molecules transport trough the interlayer space. The results obtained from the MD simulation will be useful for any future studies related to the mechanical properties of the C-S-H phases or creep or shrinkage through the interlayer of the C-S-H phases.
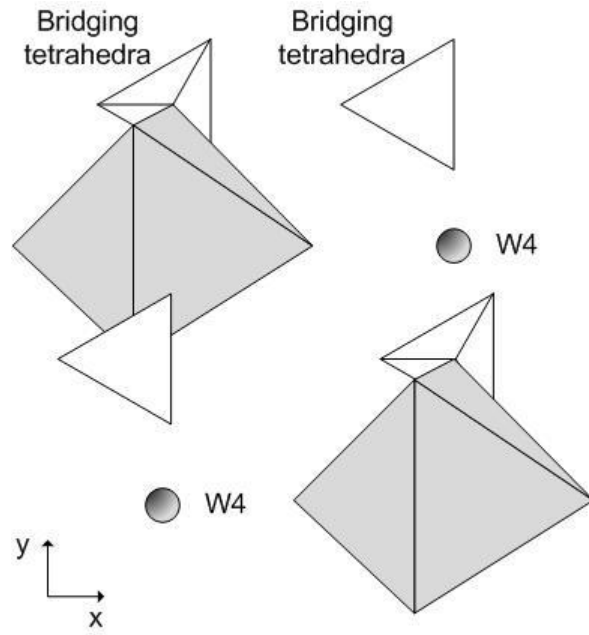
(a)
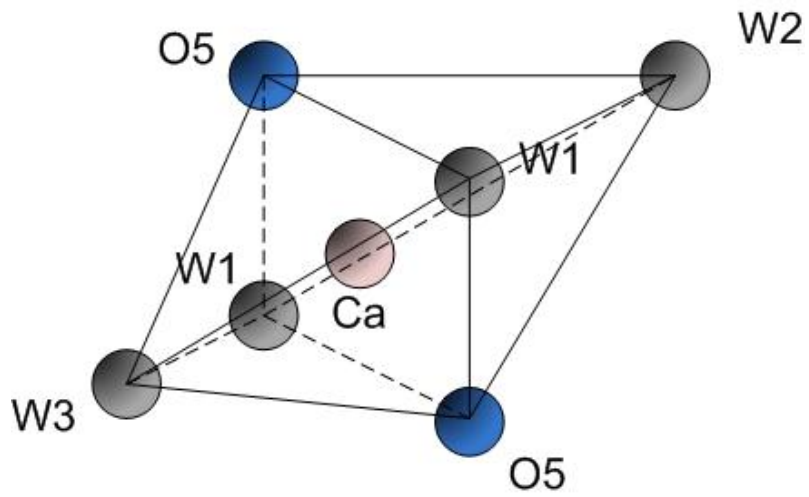
(b)

Figure 3-1. Proposed interlayer structure of 14 Å tobermorite [52]: (a) ordered distribution of Ca-centered octahedra and water molecules (W4) viewpoint [001]; and (b) octahedron centered on Ca and surrounded by water molecules (W1-W3) and oxygen atoms of bridging tetrahedron (O5).
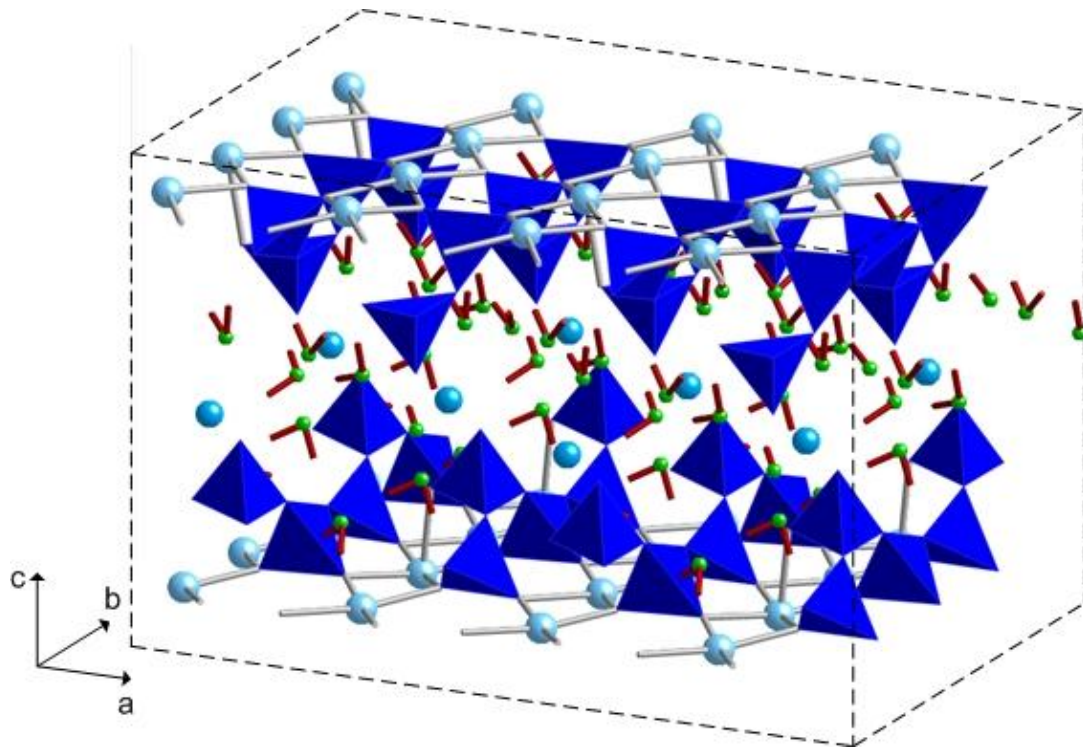
Figure 3-2. Model structure of 14 Å tobermorite initially formed as a simulation cell.
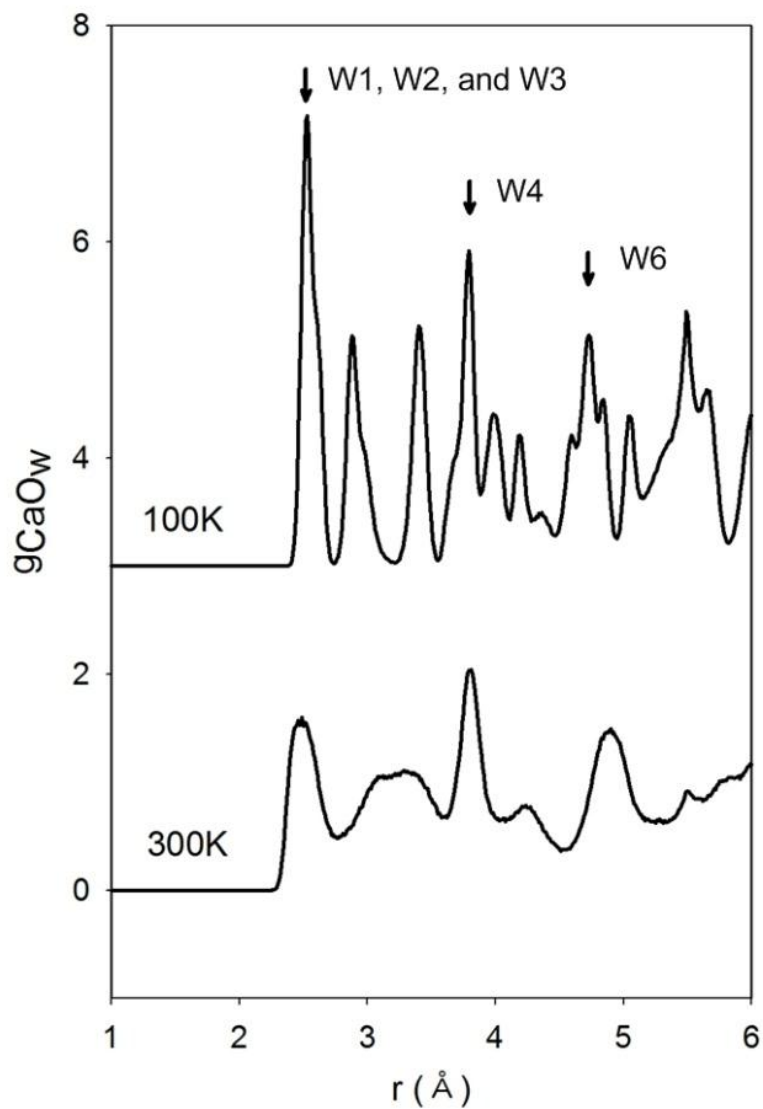
Figure 3-3. Ca-O$_w$ radial distribution function at different temperatures: Ca and subscripts O$_w$, respectively, denote calcium cation in the interlayer and oxygen of the water molecules.
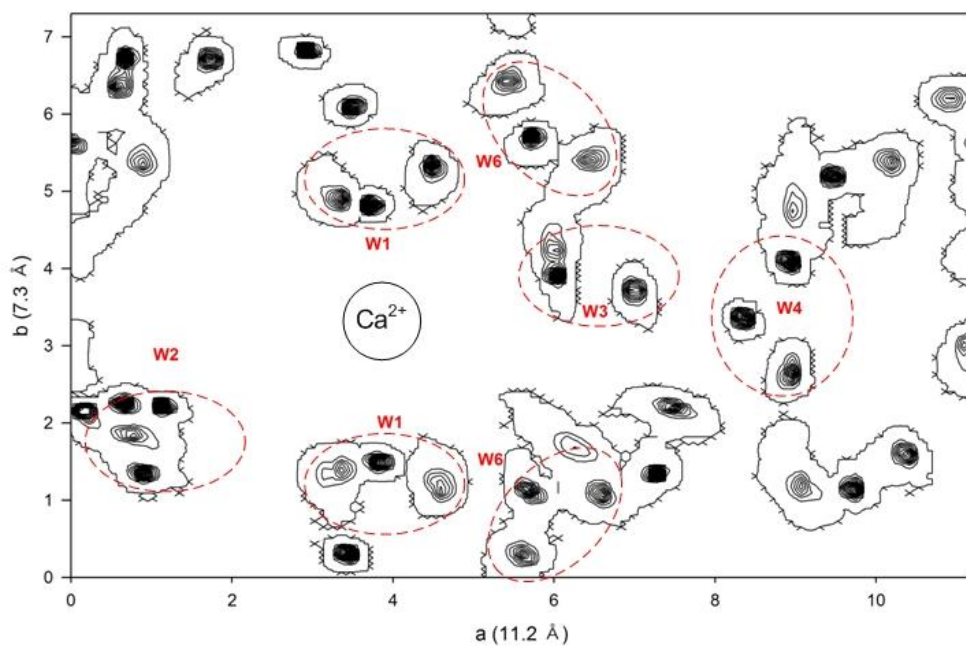
(a)
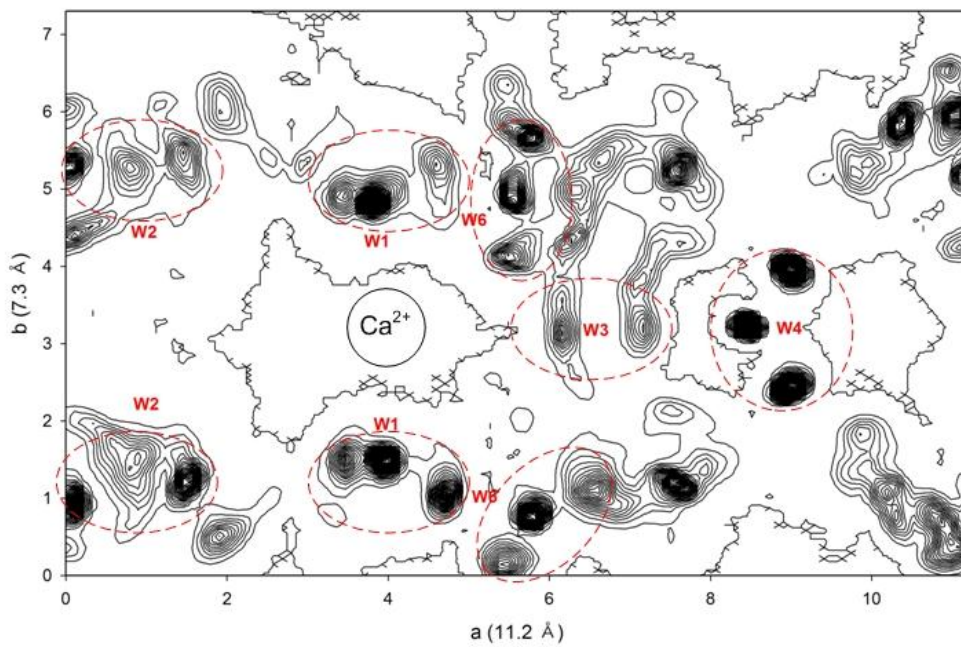
(b)

Figure 3-4. Contour maps of atomic density profiles of the water molecules accumulated along the *c*-axis of the interlayer as seen downward [001]: (a) T = 100 K and (b) T = 300 K.

(a)   (b)
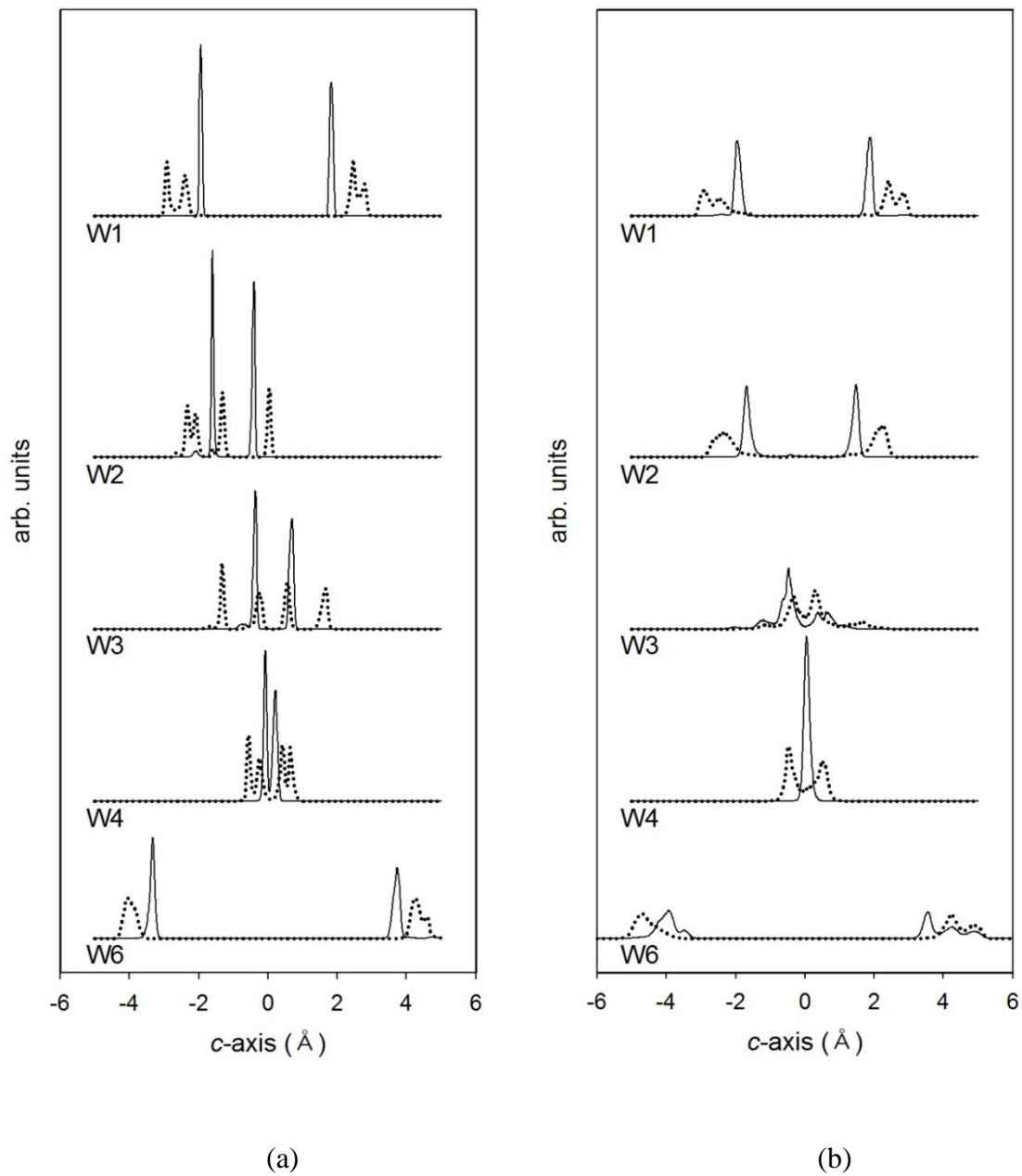
Figure 3-5. Atomic density profiles of oxygen (solid lines) and hydrogen (dashed lines) along the c-axis for W1, W2, W3, W4, and W6 water molecules at different temperatures [(a) 100 K and (b) 300 K]: the middle point of the interlayer is the original point taken as zero.
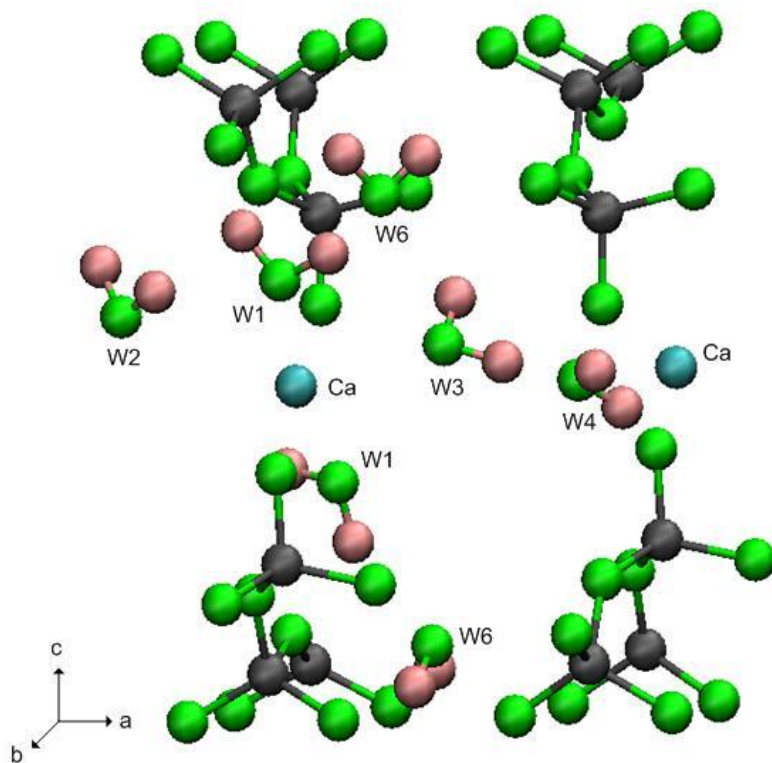
Figure 3-6. A snapshot of water molecules in the interlayer of 14Å tobermorite.

Table 3-1. Proposed orthogonal coordinates of the water molecules: the position of the calcium cation was taken as the origin.

molecule	atom	a (Å)	b (Å)	c (Å)
	Ca	0.0000	0.0000	0.0000
W1	O_w	0.3063	-1.6999	1.8013
(upper)	H_w	0.1481	-1.6232	2.7743
	H_w	1.0873	-2.3364	2.2311
W1	O_w	0.0494	1.7043	-1.9123
(lower)	H_w	0.8850	-2.2115	2.2971
	H_w	-0.2592	-1.7822	-2.8934
W2	O_w	-2.3093	-1.8513	1.5060
	H_w	-3.0079	-1.5612	2.2397
	H_w	-1.7087	-2.2238	2.2446
W3	O_w	2.4049	0.7056	0.6892
	H_w	3.4015	0.4510	0.3913
	H_w	2.4331	0.9292	1.6966
W4	O_w	4.8487	0.1415	0.2652
	H_w	5.4378	-0.5310	0.7080
	H_w	5.4113	0.9532	-0.1601
W6	O_w	2.0566	-2.2441	3.6262
(upper)	H_w	1.8712	-3.1515	3.9790
	H_w	2.4273	-1.8374	4.5604
W6	O_w	2.2943	2.5323	-3.2410
(lower)	H_w	3.0778	2.1714	-3.7938
	H_w	2.0175	3.2189	-3.9317

Table 3-2. Self-diffusion coefficients of water molecules related to tobermorite: w denotes the water molecule

Self-Diffusion Coefficient	Value (10^{-11} m^2/s)
Interlayer Dw at 100 K	0.28
Interlayer Dw at 300 K	1.4
Inner surface Dw [93]	5.0
Outer surface Dw [93]	60

Chapter 4.

Effects of NaCl on the Nanostructure of Calcium Silicate Hydrates and Monosulfoaluminate: A STXM Study

As described in Chapter 1, C-S-H and AFm phases play an important role in adsorbing chloride ions. In addition, the C-S-H phases are known as adsorbing sodium ions [41]. This chapter describes the interactions of C-S-H and monosulfoaluminate with the NaCl solution. The importance of the C-S-H phases and the complexity of their structure were already emphasized in Chapters 1 and 3. Monosulfoaluminate is chosen because first, it is abundant among AFm phases due to the sulfate source of the gypsum, and second, its intercalated sulfate does not forms solid solution with the ion-exchanged chloride (all other AFm phases do) [49]. The replacement of sulfate ions with chloride in monosulfoaluminate occurs in alternate layers in the course of its transformation to Kuzel's salt, before forming Friedel's salt which has chloride ions in all layers [49]. Therefore, we need to understand how the phase assemblage is changed from pure monosulfoaluminate as a function of the concentration of the NaCl solution. This is because it is possible that the continuous adsorption isotherms like Freundlich and Langmuir cannot represent the transformation to Kuzel's salt or Friedel's salt. In this chapter, scanning transmission X-ray microscopy (STXM) measurements (see Chapter 2) were performed to investigate the interactions between the sodium or chloride ions and the C-S-H. This synchrotron-based spectroscopic tool allows the investigation of various chemical reactions and materials, including amorphous and crystalline materials, and the reactions occurring between solids and ions. In this chapter, the technique is used to resolve both the spatial resolution and speciation limitations with the current experimental methods. In other words, STXM with concurrent measurements of X-ray absorption near edge spectroscopy (XANES) was used to examine sample compositions and spatial heterogeneities, and thus interpret interactions between sodium or chloride ions and the C-S-H with different Ca/Si ratios.

It is necessary to quantify the phase assemblage for predicting the phase change of monosulfoaluminate as a function of the concentration of the NaCl solution. Pure monosulfoaluminate was synthesized and reacted with different NaCl concentrations. STXM and XANES were used to quantify the phase assemblage and observe the sample morphology. XRD was also performed to identify the phases presented in the samples. Furthermore, thermodynamic calculations based on a previously reported database for cementitious substances were performed and compared with the quantified phase assemblage obtained from the XRD and XANES analysis. These calculations help in understanding the phase changes of monosulfoaluminate in detail.

4.1. Materials and Methods

4.1.1. Sample Preparation

All of the C-S-H samples (with Ca/Si molar ratio of 0.66, 0.95, 1.44, and 1.60) were synthesized at room temperature from calcium oxide, amorphous silica, and water, according to quantities listed in Table 4-1. To minimize the effects of carbonation, C-S-H synthesis and handling were performed inside a glove box filled with flowing N_2 gas. The calcium oxide was produced by overnight decarbonation, whereby calcium carbonate produced by Aldrich was heated to 1000 ℃. Amorphous nano-silica was provided by Cabosil. Calcium oxide, amorphous silica, and freshly deionized water were immediately mixed and sealed in thick-walled polypropylene bottles. In the reported study [119], stirring for one week was enough time to synthesize the C-S-H with Ca/Si = 0.66, 0.95, and 1.44, and we also confirmed the purity of the samples from powder XRD in Figure 4-1. Therefore, the mixed reactants, resulting in C-S-H with Ca/Si = 0.66, 0.95, 1.44, was stirred for one week. It should be noted that the mixed reactants for the 1.60 Ca/Si C-S-H were continuously mixed for one year until synthesis of pure C-S-H was verified through powder XRD, as seen in Figure 4-1. The final materials were filtered and dried under vacuum for two days and stored in an N_2 environment. As shown in Table 4-1, the water content of the mixed reactants for 1.60 Ca/Si C-S-H differs from that for other C-S-Hs. The reason to use the low water content for 1.60 Ca/Si C-S-H is that the high water content can induce calcium leaching in the Ca rich (Ca/Si = 1.60) C-S-H. Bulk chemical compositions (CaO and SiO_2) of solid samples were determined by X-ray fluorescence (XRF). NaCl-reacted C-S-H samples were prepared by reaction of the C-S-H with excess 0.35M NaCl solution in rotating barrel for 6 months. The 0.35 M concentration was chosen to use a similar concentration with seawater. The final materials were filtered and dried under vacuum for 2 days and then checked whether they contain NaCl precipitation or carbonation using XRD. After all these preparations, the samples were stored under N_2 environment until STXM measurements.

To synthesize AFm phases, tricalcium aluminate (C_3A; $Ca_3Al_2O_6$) was used as a precursor. C_3A was prepared from the stoichiometric mix of 3 mol $CaCO_3$ and 1 mol Al_2O_3 by sintering in a muffle furnace at 1450℃. Subsequently, the sample was quenched. All chemical reagents were analytical grade. Monosulfoaluminate, Friedel's salt, and Kuzel's salt were prepared according to the methods of Matschei et al. [120], and ettringite was synthesized using a method described by Perkins et al. [121].

Pure monosulfoaluminate was synthesized from the stoichiometric mix of 1 mol C_3A and 1 mol $CaSO_4$ in freshly deionized water; thereafter, the mixture was stirred for 7 days at 85℃. Next, the sample was filtered under N_2 atmosphere and dried in a vacuum chamber. Friedel's salt was prepared by mixing C_3A and $CaCl·2H_2O$ in a 1:1 molar ratio with freshly deionized water and then stirring in a tightly sealed container for one month at 23 ± 2℃, with subsequent filtration and drying. Kuzel's salt was made by adding C_3A,

$CaCl_2 \cdot 2H_2O$, and $CaSO_4$ in stoichiometric quantities to freshly deionized water. The mixture was also tightly sealed to prevent carbonation and stirred for 6 months at 23 ± 2°C before filtration and drying. Ettringite was initially prepared from two reactant solutions, specifically 6.65 g $Al_2(SO_4)_3 \cdot 18H_2O$ / 100 ml deionized water and 4.44 g $Ca(OH)_2$ / 250 ml deionized water. The reactant solutions were added together and diluted to 500 ml of additional water and 0.5 ml of 1 N NaOH solution in an N_2-filled glove box. The mixture was tightly sealed and stirred for 48 hours at 60°C before filtration and drying. NaCl-reacted monosulfoaluminate samples were prepared by suspending 0.02 g of synthesized monosulfoaluminate in 1 ml of 0, 0.1, 1, 3 and 5 M NaCl solutions for 7 days at 23 ± 2 °C. Thereafter the samples were filtered and dried in vacuum desiccators for 2 days. They were also stored under N_2 environment until further experiments

4.1.2. Experimental Setup and Analysis

X-ray diffraction (XRD) was used to identify and characterize samples, and XRD patterns were obtained at room temperature using a Rigaku Rotaflex RU200B instrument with a step of 0.02^o and Cu Kα_1 radiation at 30 kV, 15 mV. Powder X-ray XRD patterns have been analyzed with X'Pert HighScore Plus software package [122]. The STXM measurements reported herein were conducted using the STXM at BL5.3.2.1 and BL11.0.2.2 of the Advanced Light Source (ALS) at the Lawrence Berkeley National Laboratory. The XANES spectra can be obtained from these image stacks or line scans. The procedure for collecting stack images thus consists of measuring the XANES spectra for a specific element on each pixel or selected area in which one pixel can be as small as 25~30 nm. Normalization and background correction of the XANES spectra were performed by dividing each spectrum by a background spectrum taken at a sample-free area on the Si_3N_4 window. Axis 2000 software (version 2.1) [123] was used to align stack images and extract XANES spectra from stack and line scan images.

The least-square linear combination (LC) fitting implemented in the IFEFFIT package (ATHENA) [124] was performed to identify the contribution of XANES spectra of reference samples to the XANES spectra measured from the sample of monosulfoaluminate suspended in NaCl solutions. The R-factor was checked as an indicator of the robust quality of the fit.

$$R = \frac{\sum \left(\mu_{i,\exp} - \mu_{i,fit} \right)^2}{\sum \left(\mu_{i,\exp} \right)^2} \tag{4.1}$$

where, $\mu_{i,\exp}$ is the measured absorption of the sample and $\mu_{i,fit}$ is the fitted absorption from the reference spectra. The thermodynamic calculations were carried out using the geochemical code PHREEQC [125], and the thermodynamic database HATCHES

version NEA 15 [126]. The solubility constant of Friedel's salt reported by Bothe et al. [127] was used. Although there are polymorphs of Friedel's salt [128-131], only one of the polymorphs at low temperature was considered: The experiments and calculations in this study were maintained at room temperature. Solubility constants and densities of the AFm and AFt compound family were obtained from thermodynamic data reported by Matschei et al. [120] and Balonis [132], respectively.

4.2. Results and Discussion

4.2.1. Interactions between the C-S-H and NaCl

Figure 4-2(a) shows the STXM image at an energy of 1065 eV for the 0.66 Ca/SI C-S-H reacted with the NaCl solution. The Na K-edge (1070 ~ 1105 eV) and Cl K-edge (2790 ~ 2850 eV) were explored to probe for the trace of sodium and chlorine elements over the 0.66 Ca/Si C-S-H sample on the silicon nitride window (500 × 500 μm). Sodium was detected but not chlorine. Figure 4-2(b) shows the distribution map of sodium in the computed optical density between the image taken at the pre-absorption edge at 1065 eV, and the near absorption edge at 1077 eV. Note that the NaCl-reacted 0.66 Ca/Si C-S-H sample has a Na-containing area but nowhere Cl was observed. Based on the Na map in Figure 4-2(b), Na K-edge and Si K-edge XANES spectra from Area 1 and 2 of Figure 4-2(a) are shown in Figure 4-2(c) and (d). The Na K-edge spectra in Figure 4-2(c) clearly indicate that the sodium is present in Area 1 but not in Area 2. As shown in Figure 4-2(d), the silicon binding energies are 1847.0 eV in Area 1 and 1847.3 eV in Area 2. Even though 0.3 eV is a marginal shift in the binding energy compared to the 0.2 eV energy resolution in the Si K-edge XANES, this energy shift may suggest possible heterogeneity in silicate structures. As a matter of fact, the Si K-edge generally shifts to a lower binding energy with the increased depolymerization of silicate chains due to structural instability [133]. Therefore, the energy shift suggests the possible interaction between the C-S-H and the sodium ions depolymerizing silicate chains in the C-S-H.

To understand the variation in the silicate structure of the C-S-H, it is worth reviewing the structure of the silicate tetrahedral linear chains in Figure 4-3: Q1 is an end silicate tetrahedral of a chain, Q2 is a middle silicate tetrahedral in the pairing site, Q2L is the middle one in the bridging site, and Q3 is a silicate tetrahedral branching to another silicate chain. It is well known that a significant fraction of the bridging silicate tetrahedra (Q2L) is often missing in the silicate chains of the C-S-H, implying that those sites are vulnerable [134]. Based on this fact, the depolymerization due to the interaction between the C-S-H and sodium ions could be explained by the vulnerable bridging tetrahedra. In other words, the bridging tetrahedra (Q2L) could be removed by the sodium interaction to depolymerize the silicate chains. Traces of the sodium and chlorine elements were not detected in the C-S-H samples with Ca/Si = 0.95 and 1.44. This suggests that the sodium and chloride ions may not interact strongly with the C-S-H at a medium range of Ca/Si ratios (approximately 0.9 ~ 1.4).

STXM measurements were conducted to assess the interactions between sodium or chloride ions and the 1.60 Ca/Si C-S-H. Figure 4-4(a) shows an STXM image of the NaCl-reacted 1.60 Ca/Si C-S-H taken at 1850 eV. There was no significantly detectable chlorine in Areas 3 to 5. Thus, Areas 1 and 2 were magnified and measured for the chlorine element. Figure 4-4(b) shows the contrast map for the Cl L_{III}-edge. The presence of chlorine is also detectable with the Cl L_{III}-edge XANES spectra between 200 and 205 eV. The chlorine signatures in the Cl L_{III}-edge XANES spectra [see Figure 4-4(c)] provide evidence for the significant enrichment of chlorine in Area 1 compared to Area 2, meaning that there was an interactive correlation between the bound chloride ions and the C-S-H; no sodium was detected in the C-S-H with a 1.60 Ca/Si ratio. In addition, the Si K-edge XANES spectra in Figure 4-4(d) are similar in their binding energies at 1846.5 eV, indicating that there are no spatial heterogeneities in the silicate structure of the C-S-H. Hence, it could be suggested that the silicate chains of 1.60 Ca/Si C-S-H remained intact despite the strong interaction with chloride ions.

Based on the Ca/Si ratio, the C-S-H phases exhibited different behaviors in NaCl solution. The STXM measurements show that the C-S-H with 0.66 Ca/Si had only a Na-containing area; the C-S-H with 0.95 or 1.44 Ca/Si had neither Na nor Cl-containing areas, and the C-S-H with 1.60 Ca/Si had only a Cl-containing area. In the C-S-H phases, non-bridging oxygen of the silica tetrahedral chains presented in the end groups of the silicate chains induces a negative charge. Positively charged calcium ions in the interlayer space complement the negative charge of the silicate chain. However, it could be possible that the excessive cations within the interlayer structure can shift the overall charge balance of the C-S-H interlayer from negative to positive, even with the charge balancing mechanism of the negatively charged end group (Q1) in silicate chains. In this condition, the residual charge in the C-S-H influences the ionic selectivity: sodium when negative at a low Ca/Si and chloride when positive at a high Ca/Si. Previously, Hong et al. also reported that sodium and potassium binding into the C-S-H phase improves as its Ca/Si ratio decreases [47]. The residual charge also explains the fact reported in many previous studies that the proportion of Q1 tetrahedra (end groups) increases as the Ca/Si ratio increases [41, 135]. The C-S-H with higher Ca/Si ratio has more calcium ions held in its interlayer space. For this reason, the increase in the Ca/Si ratio of the C-S-H means that the increasing positive charge of the calcium ions becomes equivalent to the negative charge of silicate chains at a certain Ca/Si ratio (approximately 1.0 ~ 1.4) of the C-S-H. Thus, silicate chains must break their connections to produce more negative charges to balance the positive charge of the excessive calcium cations. This phenomenon is reflected through an observed increase in Q1 tetrahedra. When the silicate chains exhaust most of the vulnerable bridging tetrahedra at higher Ca/Si ratios, the overall charge in the C-S-H becomes positive, and the C-S-H with a high Ca/Si ratio in a saline environment adsorbs chloride ions to compensate for the net positive charge caused by excessive calcium cations. As shown in Figure 4-2(d) and Figure 4-4(d), sodium ions depolymerized the silicate chains of the C-S-H with 0.66 Ca/Si, whereas chloride ions had no effect on the silicate chains of the C-S-H with 1.60 Ca/Si. As mentioned above,

the C-S-H with low Ca/Si contains many bridging sites, which are vulnerable enough to be subjected to increased relaxation induced by interacting sodium cations. On the other hand, since the C-S-H with high Ca/Si already has less available bridging tetrahedra, it may maintain its silicate structure without depolymerization even as chloride ions interact with the C-S-H. As a result, the Si K-edge spectra in Figure 4-4(d) reflect no variance in the binding energies.

4.2.2. XANES Reference Spectra of AFm and AFt phases

AFm phases have a layered structure consisting mainly of sheets of $Ca(OH)_6$ octahedral ions, but one third of Ca are replaced—mainly by Al or Fe—as a relatively minor substitution. In the $Ca(OH)_6$ octahedron, the Ca cation forms seven-fold coordination with an additional water molecule from the interlayer space, and this water molecule directly interacts with interlayer anions, such as SO_4^{2-}, OH^-, Cl^-, and CO_3^{2-}. Therefore, probing the nearest atomic neighbors and coordination environments around the Ca atom can be a good indicator to distinguish the different AFm phases, and XANES spectra can provide such information on the status of AFm phases. Wieland et al. reported no differences in Al K-edge XANES spectra of AFm-type compounds, despite the different chemical compositions and structures [136]. It is likely that changes in coordination environments around Al atom in AFm compounds are less sensitive to variations in the interlayer substitutes. Ca $L_{III,II}$-edge XANES spectra, in particular, have different intensities of pre-edges, which indicates the magnitude of the crystal field [137]; moreover, the crystal field parameter might differ with the electro-negativities of interlayer anions in the AFm phases. We carried out experiments to collect Ca $L_{III,II}$-edge XANES spectra of Kuzel's salt ($Ca_4Al_2(SO_4)_{0.5}(Cl)(OH)_{12} \cdot 6H_2O$), Friedel's salt ($Ca_4Al_2(Cl)_2(OH)_{12} \cdot 4H_2O$), monosulfoaluminate ($Ca_4Al_2(SO_4)(OH)_{12} \cdot 6H_2O$), and ettringite ($Ca_6Al_2(SO_4)_3(OH)_{12} \cdot 26H_2O$) for reference spectra.

Figure 4-5 shows the XANES spectra of the AFm and AFt powder samples. These spectra have been extracted and normalized using aXis 2000 and IFEFFIT software package.[123, 124, 138] We labeled the main peaks *a1* and *a2* (L_{III}-edge) and *b1* and *b2* (L_{II}-edge). The Ca $L_{III,II}$-edge spectra show two well-resolved features corresponding to L_{III} (349.3 eV) and L_{II} (~352.6 eV). The multi-peak pattern before the main edges is derived from the crystal field in response to the symmetry of the atoms surrounding Ca in the first shell. As shown in Figure 4-5, the AFm phases that are Kuzel's salt, Friedel's salt, and monosulfoaluminate have similar pre-L_{III}-edge features, with three distinguishable peaks, since Ca atoms are seven-fold coordinated by the same ligands. In contrast, ettringite has two major pre-edge features since the Ca atoms in these phases are eight-fold coordinated. Our observations are in good agreement with a previously reported study on symmetry coordination and pre-edge features [137]. These features in each of the AFm and AFt phases are listed in Table 4-2.

4.2.3. Phase Quantification from NaCl-Reacted Monosulfoaluminate

To investigate the phase assemblage of monosulfoaluminate reacted with chloride ions, a series of monosulfoaluminate suspended in selected concentrations (0, 0.1, 1, 3, and 5 M) of NaCl solutions were analyzed by XRD (see Figure 4-6). The phase change occurred even in freshly deionized water (0 M NaCl solution). Although the diffraction patterns are dominated by the peaks at 9.9° and 19.9° *2θ*, which are attributed to monosulfoaluminate, ettringite is also identified at 9.1° and 15.8° *2θ*. In the 0.1 M NaCl solution, the intensities of the peak positions corresponding to monosulfoaluminate rapidly reduced with the appearance of the new peaks at 10.6° *2θ*, indicating the formation of Kuzel's salt. When increasing the NaCl concentration, the diffraction patterns for monosulfoaluminate were not detected at 1M, 3M, or 5M NaCl concentrations, and those for ettringite were reduced in the 1 and 3 M NaCl solutions and then not detected in 5 M NaCl solution. X-ray diffraction patterns indicated the presence of small peaks corresponding to Friedel's salt in 3 M NaCl solution, and all monosulfoaluminate was completely transformed to Friedel's salt in the 5 M NaCl solution.

XANES spectra of monosulfoaluminate exposed to NaCl solutions of different concentrations were collected for the Ca $L_{III,II}$-edge. In a subsequent step, least-square fitting was carried out using the linear combination fitting tool implemented in IFEFFIT (ATHENA). Quantification of Ca-containing mineral phases was performed using the Ca $L_{III,II}$-edge reference spectra (monosulfoaluminate, Kuzel's salt, Friedel's salt, and ettringite) and existing phases identified from XRD analysis. As shown in Figure 4-7, the fitted results are in good agreement with the measured spectra. To further test the quality of fits, we calculated the R-factor, where a value of less than 0.02 is generally considered to be a good fit. Table 4-3 shows the R-factors for the XANES spectra of monosulfoaluminate samples suspended in 0, 0.1, 1, 3, and 5 M NaCl solutions. As shown in Table 4-3, all the LC fittings performed on the samples had R-factor of less than 0.02, indicating the good fit of the approach.

In the results of thermodynamic calculations, four phases—Friedel's salt, Kuzel's salt, monosulfoaluminate and ettringite—were encountered in the phase assemblage. Figure 4-8 depicts a sequence of the phase changes in monosulfoaluminate suspended in NaCl solutions with increasing concentrations from 0 to 5 M. In addition, the calculated proportions of the four phases are compared with the LC fitting results for the XANES spectra in Figure 4-8. The calculated proportion change of the phase assemblage shows generally satisfactory agreement with the phase proportions of LC fitting from XANES spectra.

4.2.4. Morphology

The STXM images in Figure 4-9 represent typical morphologies found in NaCl-reacted monosulfoaluminate with different chloride levels. Figure 4-9(a) shows the

presence of needle-like compounds, the typical morphology of ettringite [3]. However, the needle-like compounds are not detected in Figure 4-9(c) and (d). The samples in Figure 4-9(a) and (b) have large smudged regions that might be the dissolved regions of the sample particles. However, Figure 4-9(c) shows that only a small amount of the dissolved region is observed, but most regions keep the plate shape. At high NaCl concentration (see Figure 4-9(d)), the sample shows relatively well-defined hexagonal plates with a sharp edge.

4.2.5. Chloride Binding by Monosulfoaluminate

The alteration of mineral substances with exchangeable ions in a solution generally depends on pressure and temperature but additionally, on mass balances and chemical activity coefficients. The results obtained herein are particular to the concentration of aqueous solution. Thus, different experimental conditions may induce somewhat different results. Nevertheless, understanding of the phase change of monosulfoaluminate as a function of NaCl concentration is important to assess the adsorption isotherms, which are applied to determine the time to corrosion initiation for reinforced concrete in chloride environments. Therefore, more detailed description of the phase change is discussed as follows.

At low NaCl concentrations below 0.2 M, a large amount of monosulfoaluminate is dissolved into the NaCl aqueous solution, which might have a low ionic strength. A significant proportion of chloride ions below the 0.1 M concentration could substitute in the undissolved monosulfoaluminate, thus depleting chloride ions. The depletion effect will, however, be negligible for the higher initial concentrations of NaCl solutions. As the dissolution of monosulfoaluminate liberates a lot of sulfate ions, the sulfate concentration may be elevated in the solution. Since ettringite is more stable phase than monosulfoaluminate in sulfate-rich environments, it is formed in the low NaCl concentration of the aqueous solution. Therefore, the thermodynamic calculations and LC fitting results reveal an increase in the proportion of ettringite within the range of 0 to 0.2 M NaCl concentrations in Figure 4-8. Furthermore, the STXM image in Figure 4-9(a) shows the ettringite formation and the dissolution of monosulfoaluminate as containing a relatively large proportion of needle-like compounds and the dissolved area of sample particles. While some of monosulfoaluminate are dissolved into the NaCl solution, the undissolved monosulfoaluminate is simultaneously subjected to the exchange of its sulfate ions in the interlayer space with free chloride ions in the NaCl solution. For this reason, the proportion of monosulfoaluminate is rapidly reduced, while that of Kuzel's salt is rapidly elevated when the chloride concentration is increased up to 0.2 M. After all of the monosulfoaluminate was exhausted due to the dissolution and the phase transition over the 0.2 M NaCl concentration, the proportion of Kuzel's salt was slowly increased with the reduction in the ettringite formation, as shown in Figure 4-8. Ettringite formation can only occur from the dissolution/precipitation process [139]. However the dissolution of monosulfoaluminate is prevented by higher ionic strength induced by the

higher NaCl concentration in the NaCl solution. In other words, more monosulfoaluminate is intact to be subjected to the phase transition to Kuzel's salt, as it remains undissolved at the higher NaCl concentration. This process can be observed from the STXM images in Figure 4-9, in which the dissolved area is reduced as the NaCl concentration of the aqueous solution increases.

The further increase of the NaCl concentrations in the range of 3 to 4 M causes the rapid change of the dominant phase from Kuzel's salt to Friedel's salt in Figure 4-8. This transition occurs dramatically because it does not compete with the ettringite formation. Over the 4 M NaCl concentration, the sample morphology in Figure 4-9(d) maintained a well-defined hexagonal shape relatively better than those in Figure 4-9(a), (b), and (c); furthermore, needle-like ettringite cannot be observed in Figure 4-9(d). Therefore, at these concentrations, there is a phase transition from monosulfoaluminate to Friedel's salt without the dissolution of monosulfoaluminate. This means that the ion exchange becomes the only binding mechanism of chloride ions by monosulfoaluminate at high ionic strength. In short, the binding mechanism of the chloride ion by monosulfoaluminate is determined by the free chloride content, ionic strength in the pore solution, and the available amount of monosulfoaluminate in the hardened cement paste.

4.3. Conclusion

This study aimed to investigate the interactions between cementitious phases and NaCl solutions. The following conclusions were obtained:

(1) The Na and Cl-element maps obtained from the STXM images showed that the C-S-H phase with 0.66 Ca/Si strongly interacts with sodium ions, whereas that with 1.60 Ca/Si does so with chloride ions. As a matter of fact, in the C-S-H phases the non-bridging oxygen of the silica tetrahedral produces a negative charge, and the interlayer Ca cations counteract the negative charge of the silicate chain. Therefore, it is proposed that the ion selectivity of the C-S-H phases is determined by their residual charge.

(2) The Si K-edge XANES of the Na-containing area in 0.66 Ca/Si C-S-H shifted toward a lower binding energy while that of the Cl-containing area in 1.60 Ca/Si C-S-H did not differ from other non-Cl-containing areas. It is a well-known fact that the Si K-edge XANES generally shifts to a lower binding energy with increased depolymerization of silicate chains. Abundant bridging tetrahedra of the 0.66 Ca/Si C-S-H are more likely to be ruptured by the interaction with sodium ions, resulting in the energy shift. On the other hand, since the 1.60 Ca/Si C-S-H has deficient bridging tetrahedra, the silicate chains of the Cl-reacted C-S-H are more likely to remain intact.

(3) As the NaCl concentration increased up to 0.2 M in the aqueous solution, the proportions of Kuzel's salt and ettringite rose rapidly. The dissolution of monosulfoaluminate induced ettringite formation, and the phase transition from

monosulfoaluminate to Kuzel's salt occurred at low NaCl concentrations. In the 0.2 M NaCl concentration, when monosulfoaluminate was exhausted, ettringite formation was reduced through the lesser dissolution of monosulfoaluminate due to the higher ionic strength. As a result, ettringite was not found in the 4 M NaCl concentration. In the range of 3 to 4 M NaCl concentrations, without the competition of ettringite formation, Friedel's salt becomes a dominant phase from Kuzel's salt. Beyond a 4 M NaCl concentration, all of the monosulfoaluminate transformed into Friedel's salt without the dissolution.

(4) The chloride binding mechanism by monosulfoaluminate depends on the free chloride content and ionic strength in the pore solution, and the available amount of monosulfoaluminate in hardened cement paste.

Given the robust results presented herein, more systematic nano-level studies of the interaction between sodium chloride and cementitous phases is necessary to come to definite conclusions on the detailed types and mechanisms of binding on or into cementitous phases. This study provides fundamental information for further research. In addition, soft X-ray spectromicroscopy holds significant promise for studies of ionic binding mechanisms by various cementitious phases.
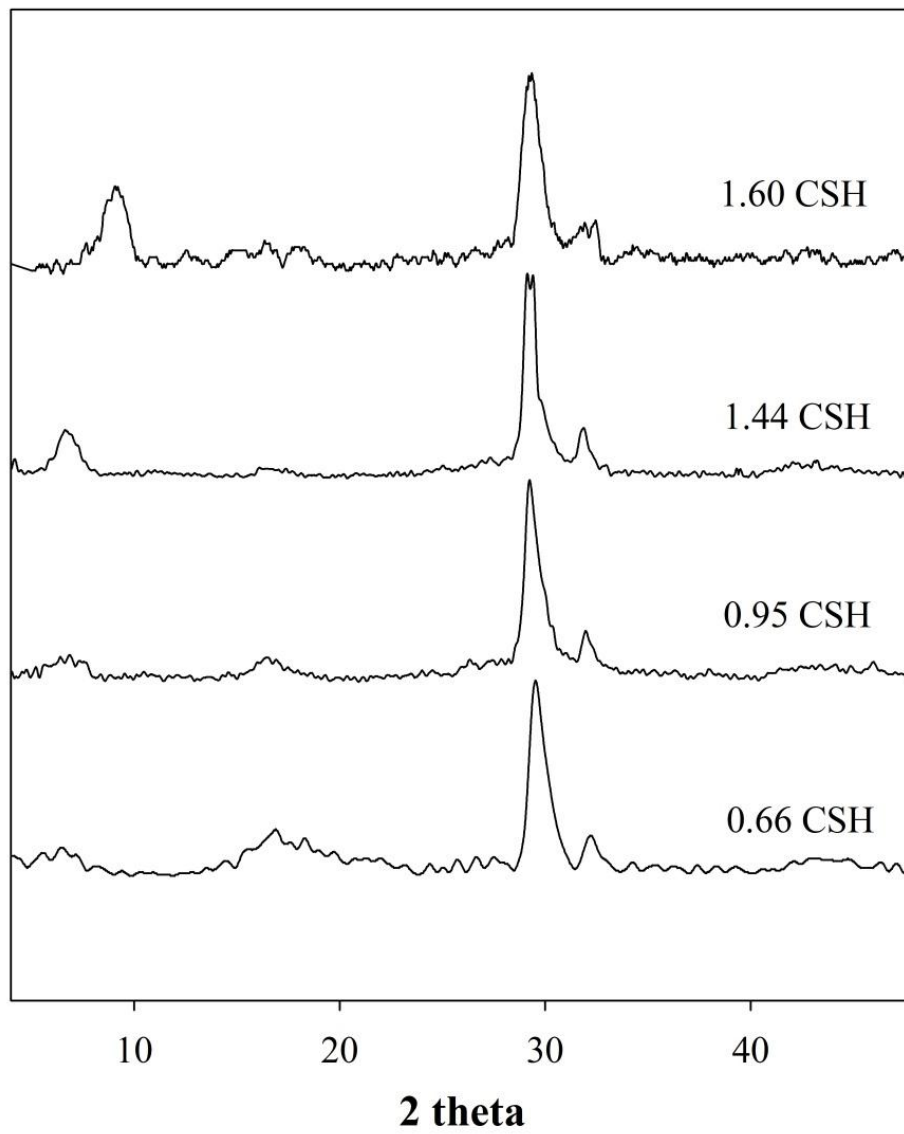
Figure 4-1. XRD powder patterns of synthetic C-S-H phases with different Ca/Si ratios.
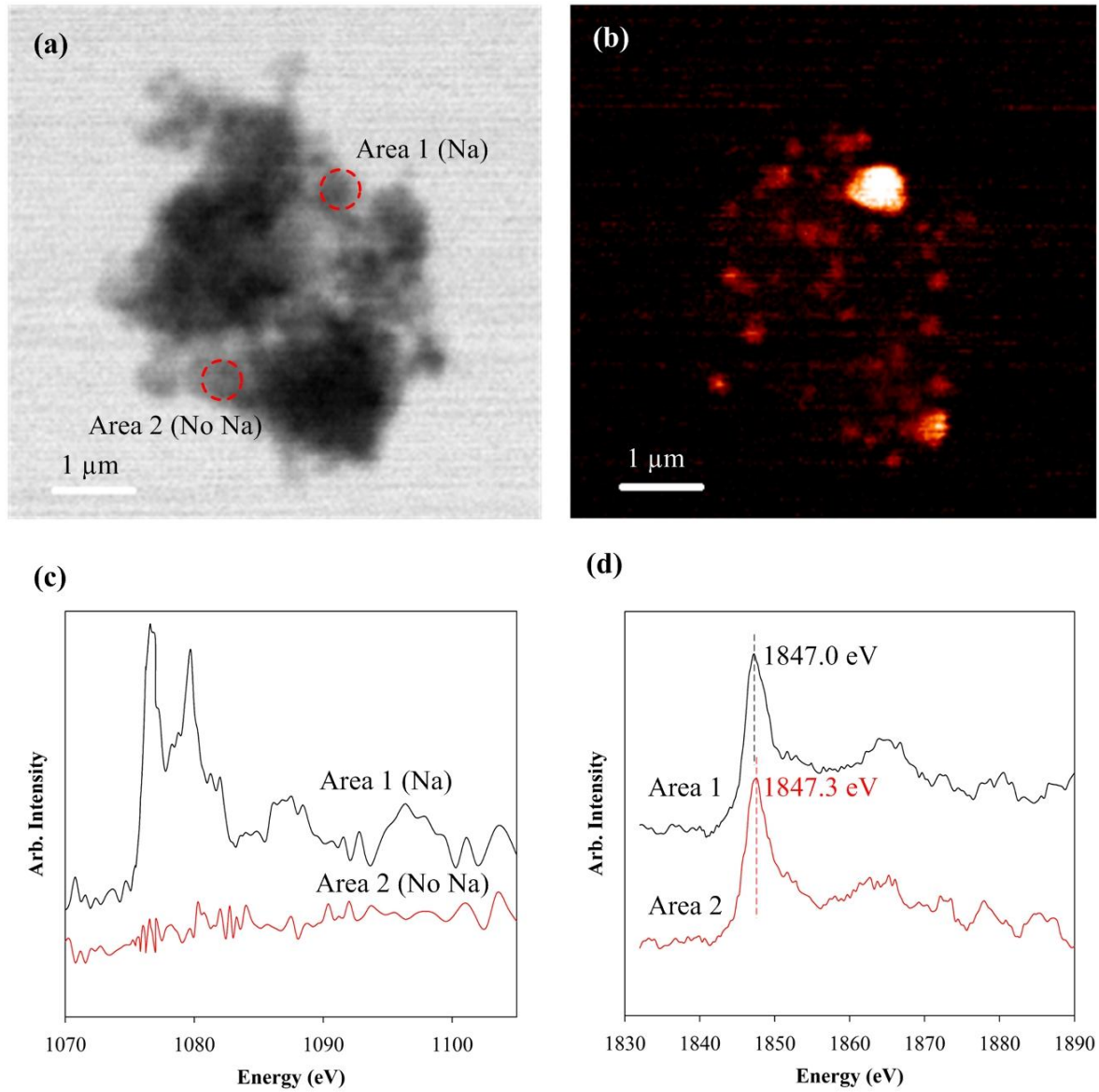
Figure 4-2. (a) STXM image of C-S-H with Ca/Si = 0.66 reacted with the NaCl solution at 1065 eV; (b) Na map of image contrast at Na K-edge where the area of high concentrations of Na area are bright white; (c) XANES spectra of Na K-edge; and (d) XANES spectra of Si K-edge taken from different locations indicated in (a).
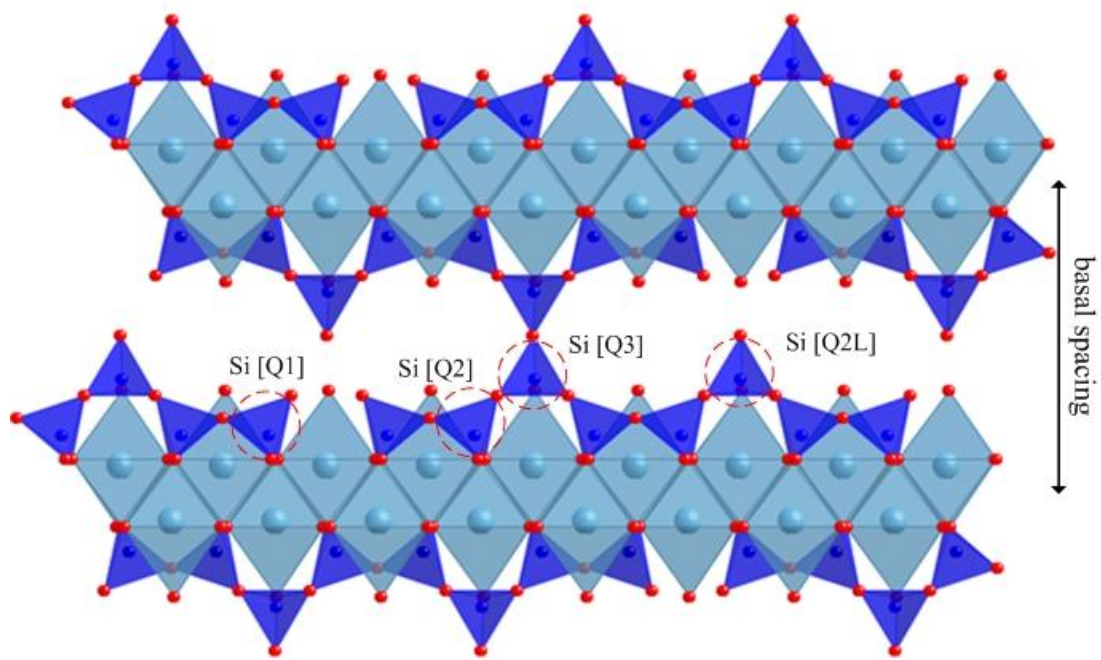
Figure 4-3. Conceptual structure of C-S-H: the triangles are Si tetrahedral, the red circles are bridging oxygen, and the diamonds are Ca octahedra.
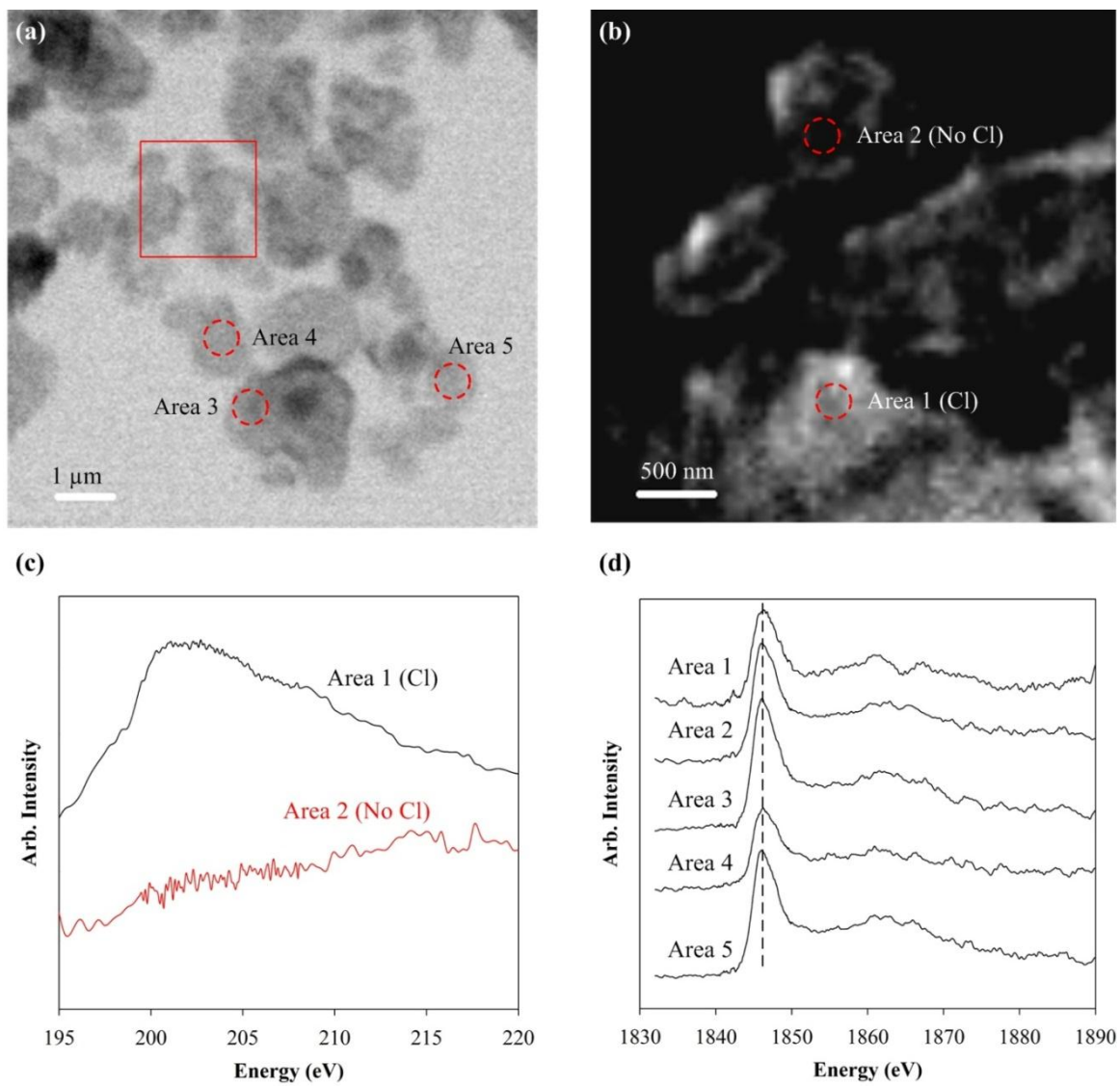
Figure 4-4. (a) STXM image of C-S-H with Ca/Si = 1.60 reacted with the NaCl solution at 202.0 eV; (b) Cl map of image contrast at Cl L_{III}-edge for the area enclosed in the square box in (a); (c) XANES spectra of Cl L_{III}-edge; and (d) XANES spectra of Si K-edge taken from different locations indicated in (a) and (b).
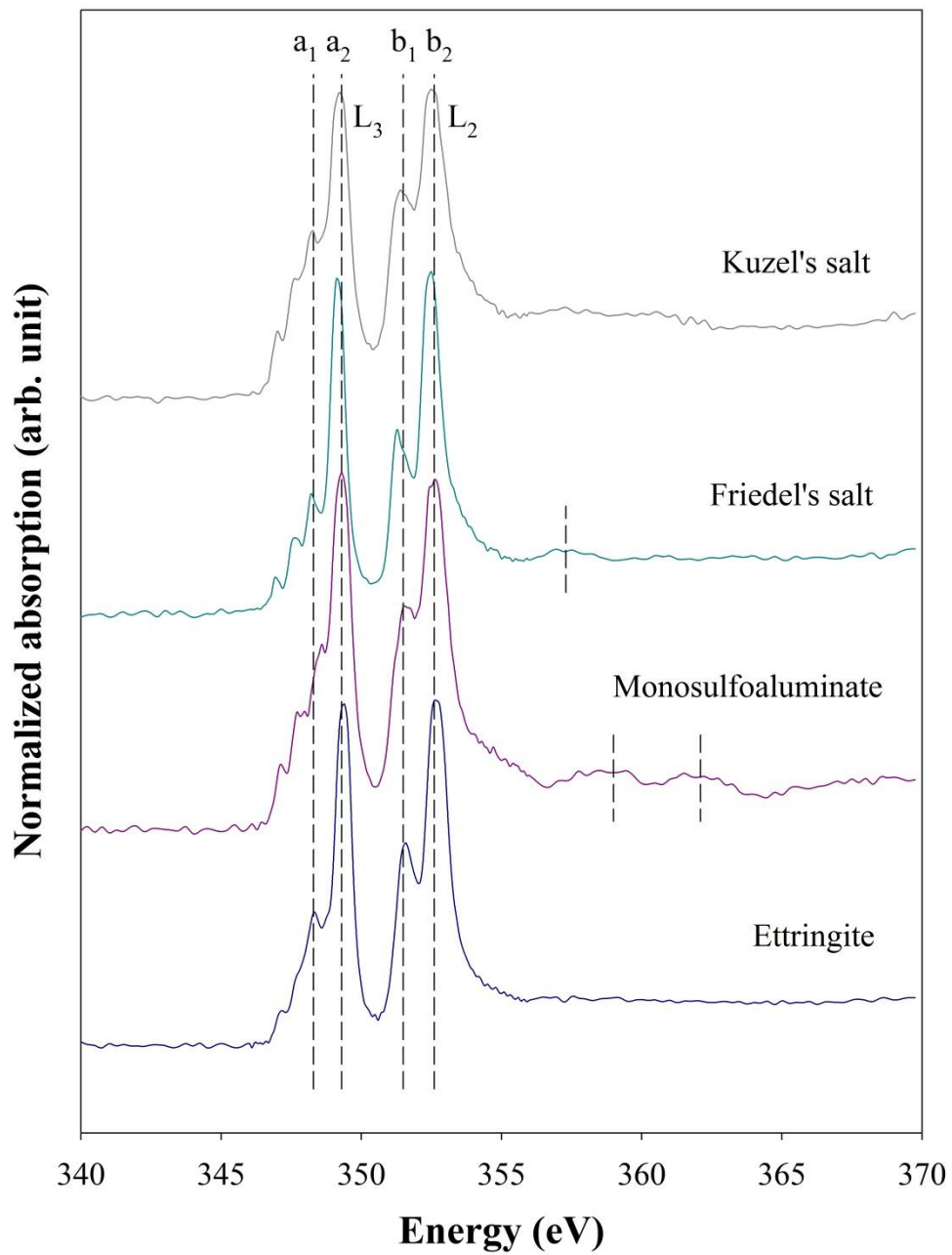
Figure 4-5. XANES reference spectra of Ca $L_{III,II}$-edge for Kuzel's salt, Friedel's salt, monosulfoaluminate, and ettringite; the broken lines indicate spectral features.
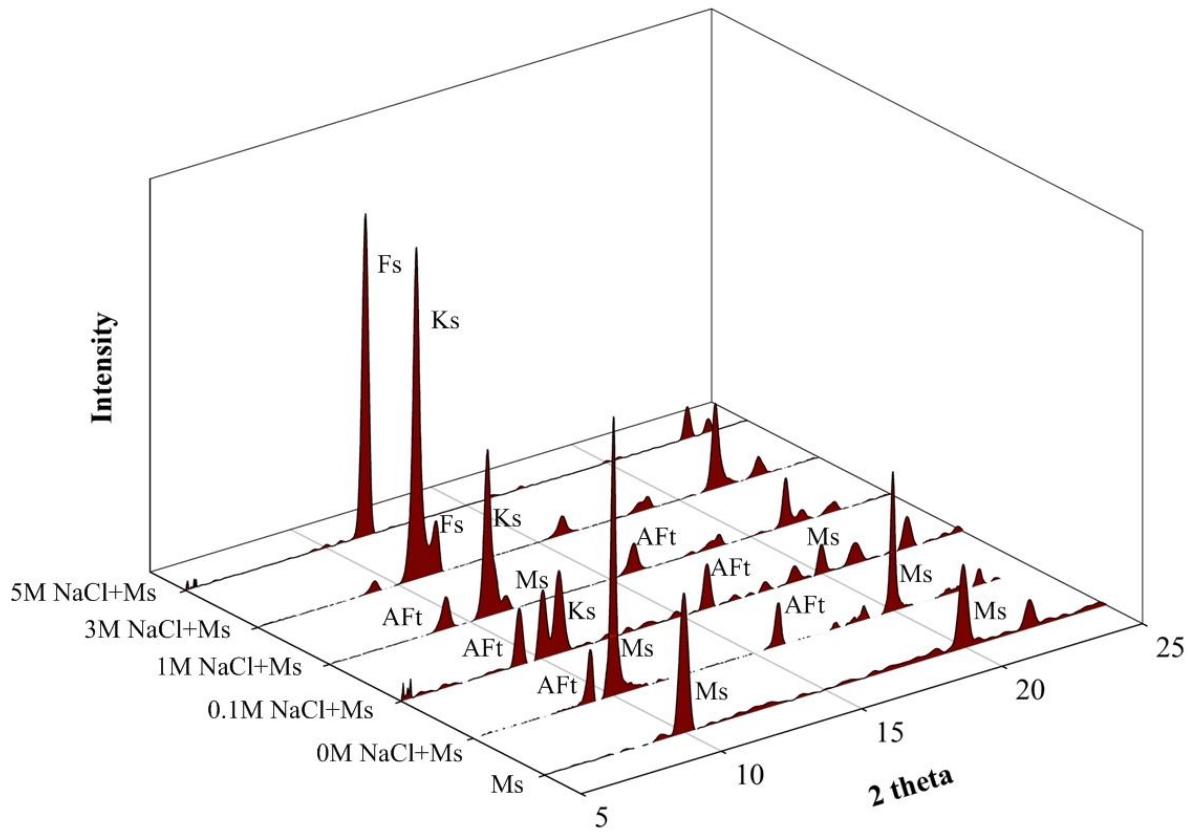
Figure 4-6. XRD patterns of phase changes from monosulfoaluminate in NaCl solutions: Ks is Kuzel's salt, Fs is Friedel's salt, Ms is monosulfoaluminate, and Aft is ettringite.
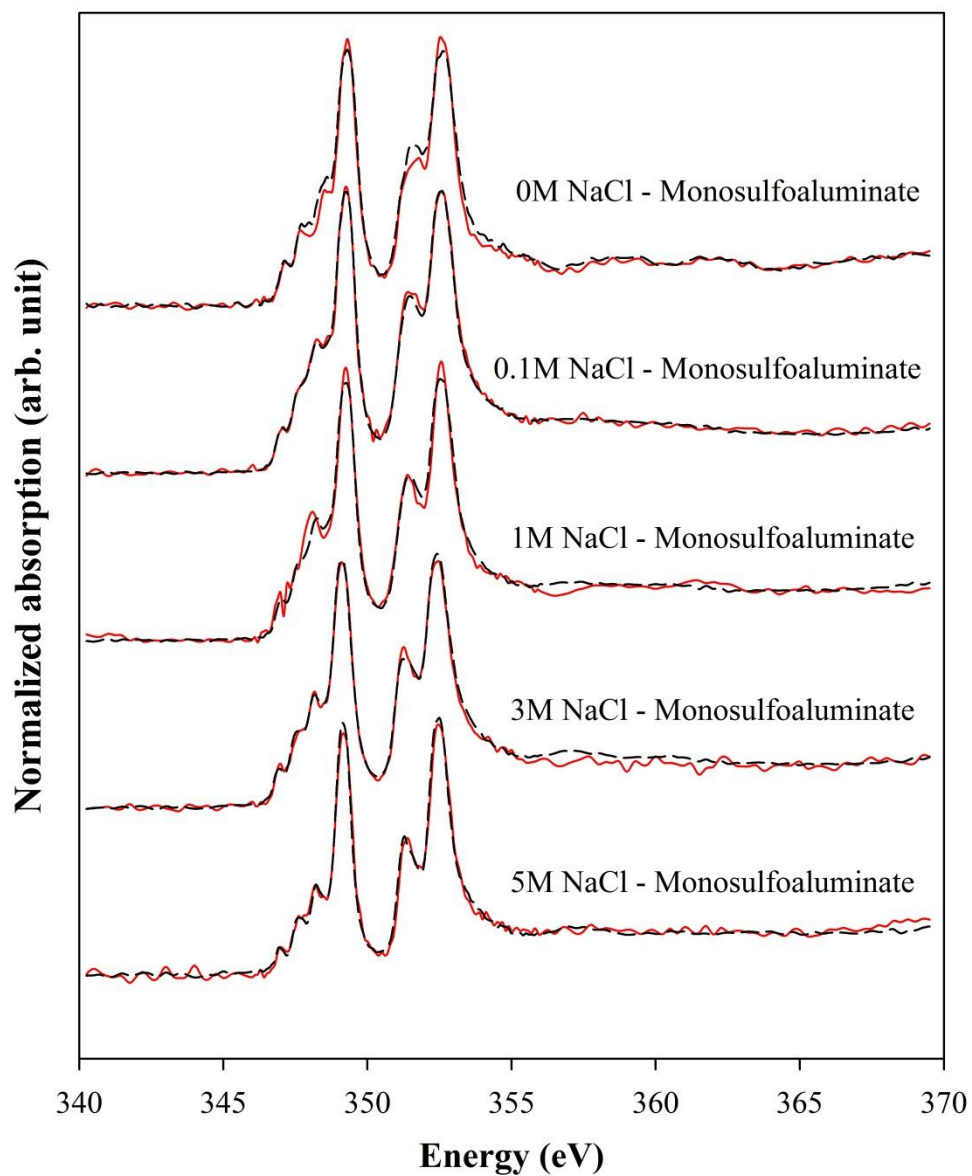
Figure 4-7. XAENS spectra of Ca $L_{III,II}$-edge collected from the samples of monosulfoaluminate that was reacted in NaCl solutions of different concentrations: solid lines are the experimental XANES spectra, and the broken lines are the modeled spectra based on LC fitting.
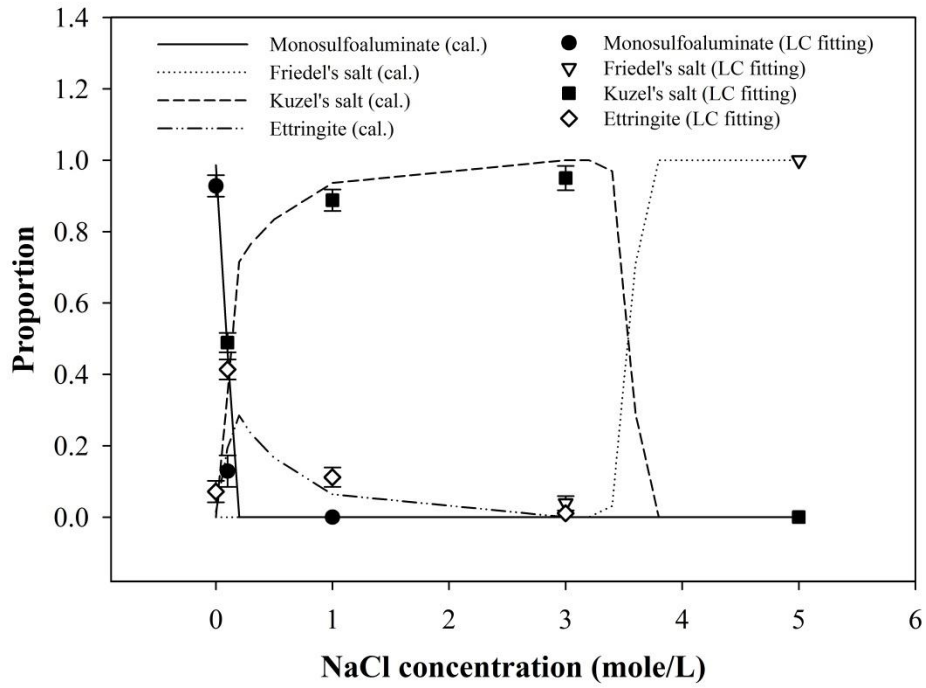
Figure 4-8. Calculated proportions of solid phases showing phase development and proportions of those determined from the least-square fitting of XANES spectra.
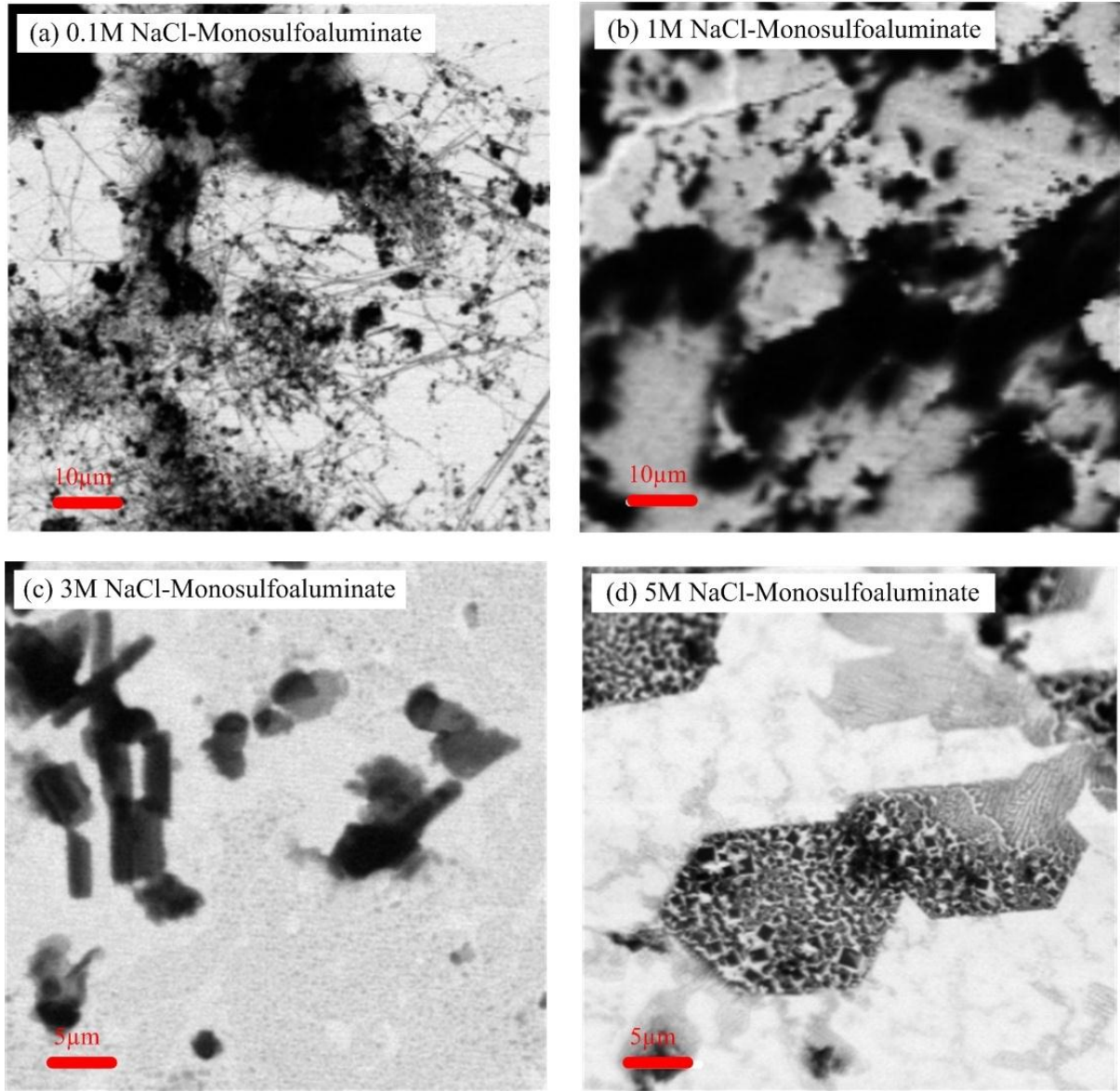
Figure 4-9. STXM images: (a) monosulfoaluminate in 0.1 M NaCl solution resulting in ettringite, kuzel's salt, and remained monosulfoaluminte; (b) monosulfoaluminate in 1 M NaCl solution resulting in ettringite and kuzel's salt; (c) monosulfoaluminate in 3 M NaCl solution resulting in kuzel's salt; and (d) monosulfoaluminate in 5 M NaCl solution resulting in Friedel's salt.

Table 4-1. Mass of reactants used for the synthesis of C-S-H samples.

Sample (C-S-H)		Ca/Si = 0.66	Ca/Si = 0.95	Ca/Si = 1.44	Ca/Si = 1.60
Mass of Reactant (g)	CaO	1.89	2.29	3.00	3.41
	SiO_2	3.09	2.57	2.07	1.94
	H_2O	250	250	250	63

Table 4-2. Ca $L_{III,II}$-edge XANES intensity ratios and peak positions of Friedel's salt, Kuzel's salt, monosulfoaluminate, and ettringite, and coordination figure within the first shell of calcium
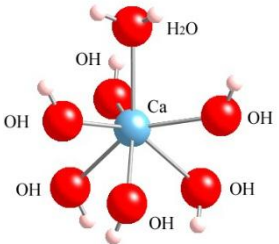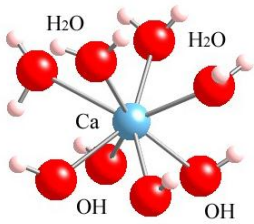
Mineral name		AFm phase			AFt phase
		Friedel's salt	Kuzel's salt	Monosulfoaluminate	Ettringite
Intensity ratio	a_2/a_1	2.77	1.36	1.87	2.56
	b_2/b_1	1.86	1.23	1.93	1.70
Peak positions in L_3-edge (eV)		346.9 347.6 348.2 **349.2**	347.0 347.6 348.3 **349.2**	347.1 347.8 348.6 **349.3**	347.2 348.3 **349.4**
Peak positions in L_2-edge (eV)		351.3 **352.5**	351.37 **352.57**	351.6 **352.6**	351.6 **352.6**
Peak positions in post-edge (eV)		357.3	–	359.0 362.1	–
Figure within the first shell of Ca					

Table 4-3. Proportions of the solid phases determined from the least-squares fitting of Ca $L_{III,II}$-edge XANES spectra.

NaCl solution	Monosulfoaluminate	Friedel's salt	Kuzel's salt	Ettringite	R-factor
0 M	0.928 ± 0.030	−	−	0.072 ± 0.030	0.0061
0.1 M	0.129 ± 0.044	−	0.489 ± 0.027	0.414 ± 0.028	0.0011
1 M	0 ± 0	−	0.888 ± 0.030	0.112 ± 0.027	0.0055
3 M	−	0.039 ± 0.020	0.950 ± 0.034	0.011 ± 0.010	0.0022
5 M	−	1 ± 0	0 ± 0	−	0.0042

Chapter 5.

Ionic Transport of Surface Treated Concrete

Chloride ions can destroy the passive layer on reinforced steel bars in concrete, and act as a catalyst to corrosion. Besides, chloride ions are not consumed in the corrosion, but remain free to continue the reaction. For this reason, the chloride-induced corrosion is one of the most dangerous and deleterious processes in reinforced concrete. The primary mechanism for the chloride ingress is the ionic transport through the concrete region covering the steel bar. To extend the service life of the reinforced concrete structure against this deterioration, one of common methods is by surface protection of concrete. This inhibits or delays the ionic transport by reducing the ionic diffusivity of the concrete surface. A more detailed description of the surface treatment was presented in Chapter 1. The influence of the surface treatment in the ionic transport still needs more research; because only a simple model derived from conventional single-species without electro-neutrality is available [70]. Most information on the ionic diffusivity of the surface-treated concrete has been provided by the application of the rapid chloride permeability test (RCPT) because this test is short in duration and provides rapid results. However, there is no appropriate model that accurately analyzes the RCPT results of surface-treated concrete samples.

Based on the extended NPP model, this chapter presents a mathematical model and its numeral implementation to investigate the effect of surface treatments using the finite-element method (FEM). The numerical model simulated ionic movements inside surface-treated concrete during an RCPT, and the algorithms were used to analyze the RCPT measurements. In the conventional single-species model, the diffusivities of concrete and a surface treatment were homogenized to provide their pseudo-diffusion coefficient. The simulation results presented here are compared to those obtained from the conventional model using the pseudo diffusivity and validated using the chloride profile of the surface-treated concrete after RCPT. Consequently, the effects of surface treatment on the ionic profiles and electric field were examined and discussed in this chapter.

5.1. Numerical Model for Surface-treated Specimens

The different pore structures between the surface-treated region and the concrete region can be involved in the model using their separate tortuosities based on Equation (1.15). As the RCPT was conducted on samples that had been subjected to saturation process, all percolated pores in the specimen were occupied by water in which the ions had dissolved and formed a pore solution. In the following simulations, only three dissolved ionic species, Na^+, Cl^-, and OH^-, were considered. Other possible ions, such as

Ca^{2+}, K^+, SO_4^{2-}, etc., were ignored because of their negligible concentrations in both the anode and cathode cells. In most previous research dealing with the extended NPP model, it was assumed that chemical reactions were negligible [22, 103]. This assumption is, at least partially, supported by the fact that RCPT is shorter in duration compared to other chloride tests. The purpose herein is to simulate the evolution of ionic movement and the electric field instead of chemical sorption; therefore, chemical reactions were not included in the simulations.

Because RCPT keeps a constant temperature and pore saturation, the terms related to these controlled conditions can be cancelled out from Equation (1.15). Therefore, the model assuming saturated condition, constant temperature, and neglect of chemical reactions is presented in the following equation:

$$\frac{\partial C_i}{\partial t} = \nabla \cdot \left\{ D_i \nabla C_i + \frac{D_i z_i F}{RT} C_i \nabla \phi + D_i C_i \nabla \left(\ln \gamma_i \right) \right\} \tag{5.1}$$

In the pore solution, the local electro-neutrality must be preserved at every point, so that any excess charge caused by the ionic movement builds up a local electric potential field. This local potential can be calculated using the Poisson equation, see Equation (1.16).

As mentioned in Chapter 2, there are two algorithms that may be used to solve the NPP model using the finite element method: the coupled algorithm based on the Picard iteration, and the uncoupled algorithm based on the Newton-Raphson method. Samson et al. stated that only the coupled algorithm is appropriate for solving the NPP system with a low value (*0.0001*) of α^2 for a steady-state case [18]. In order to reconsider the usage of the uncoupled algorithm, the dimensionless example used by Kato [17] and Samson et al. [18] is used. For the sake of simplicity, consider only the case of two monovalent ions for both species, $C_0=\omega=1$ and length $L=1$. Both species have a dimensionless concentration of 1 at $x=0$ and 1.5 at $x=1$. In this example, the governing equations are:

$$\frac{\partial C^{\pm}}{\partial t} = \frac{\partial^2 C^{\pm}}{\partial x^2} + \frac{\partial}{\partial x} \left(\frac{\partial \phi}{\partial x} C^{\pm} \right) \tag{5.2}$$

$$0 = \frac{1}{\alpha^2} \left(C^+ - C^- + \omega \right) + \frac{\partial^2 \phi}{\partial x^2} \tag{5.3}$$

Based on our numerical model in Equations (5.5) and (5.7), Figure 5-1 provides the correct solution for the uncoupled algorithm.

The coupled algorithm, on the other hand, stacks all values into one matrix that consumes a significant amount of computation resources: CPU, time, and memory. The total number of elements and species are 1000 and 3, respectively, and the matrix size is 4000×4000, including the electric potentials. In addition, the coupled algorithm requires inversing the large matrix and iterating the Newton-Raphson method to solve the

57

nonlinear set of equations per time step. In addition, the presence of the surface treatment requires incorporating a large number of elements to avoid diversion near the boundaries and interfaces. For these reasons, the uncoupled algorithm was deemed more suitable to simulate ionic movements inside the surface-treated concrete specimen during RCPT.

To derive a numerical model involving the effect of the surface treatment for the uncoupled algorithm and discrete pore structures, the extended Nernst-Planck equation was applied to the Galerkin method by using the virtual concentration (δC_i) over the domain (Ω):

$$(\delta C_i)\frac{\partial C_i}{\partial t} = (\delta C_i)\nabla \cdot \left\{ D_i \nabla C_i + \frac{D_i z_i F}{RT} C_i \nabla \phi + D_i C_i \nabla (\ln \gamma_i) \right\} \quad (5.4)$$

By applying the divergence theorem and the explicit scheme, the numerical model is expressed as:

$$\{C_i\}^{t+\Delta t} = \left\{ [I] - D_i \left[\frac{1}{\Delta t} \int_\Omega [N]^T [N] d\Omega \right]^{-1} \begin{bmatrix} \int_\Omega [B]^T [B] d\Omega + \frac{z_i F}{RT} \nabla \phi \int_\Omega [B]^T [N] d\Omega \\ + \nabla (\ln \gamma_i) \int_\Omega [B]^T [N] d\Omega \end{bmatrix} \right\} \{C_i\}^t \quad (5.5)$$

$$D_i = \begin{cases} D_i = D_i^s, & treatment\ region \\ D_i = D_i^c, & concrete\ region \end{cases} \quad (5.6)$$

where *[N]* is a shape function, *[B]* is a derivative of the shape function, *[I]* is an identity matrix, D_i^s is a diffusion coefficient of the surface treatment, and D_i^c is a diffusion coefficient of the concrete specimen. The Poisson equation is also computed in the same way, with its arranged equation given by:

$$\{\phi\} = \left[\int_\Omega [B]^T [B] d\Omega \right]^{-1} \left[\frac{F}{\varepsilon} \int_\Omega [N]^T d\Omega \right] \left(\sum_{i=1}^N z_i C_i \right) \quad (5.7)$$

Figure 5-2 shows flowcharts comparing the coupled algorithm and the algorithm for the newly derived numerical model. As shown in Figure 5-2(b), the matrix inversions are achieved before entering the time loop, with inversed matrices in Equations (5.5) and (5.7) that are constant regardless of the time, *t*. In contrast, the coupled algorithm includes the inversion process in the course of the time loop, due to an inversed matrix that varies depending on the time to solve the non-linear set of the coupled matrix. Consequently, with the numerical model presented in this study, the computation load can be reduced, enough to compute RCPT within several minutes instead of hours using personal computer systems. Therefore, the numerical model not only describes the effect of the surface treatment, but also reduces the computing time that is necessary to iteratively fit the simulation results to the colorimetric measurement as a means of

obtaining the diffusion coefficient. The initial and boundary conditions for our simulation are listed in Table 5-1. Even though the thickness of the surface treatment is unrealistic for some types of protective materials, such as pore blockers or liners, a thickness of 3 mm was used for the simulation setup to more clearly observe ionic movements within the treatment.

5.2. Model Validation

5.2.1. Materials

Sample cylinders measuring ϕ 100 × 200 mm were produced with concrete and cured in water at 25°C for 28 days. The cement was ASTM Type I Portland cement, and the coarse and fine aggregate was respectively crushed gravel and sand with a maximum particle size of 20 mm and 1 mm. The detailed concrete composition is shown in Table 5-2, and the compressive strength of the concrete samples at 28 days was 25 MPa. After 28 days of water curing, the specimen was cut into 50 mm-thick slices. One circular surface of the sample disk was coated with a 6 mm-thick polymer-modified (styrene/acrylic acid ester) cement paste (provided by Re-form System, Inc.) as a surface treatment, and then further cured in water for 7 days before being subjected to further testing.

5.2.2. Experimental

Before RCPT, the specimen was vacuum-dried for 1 days and then saturated with alkaline solution ([NaOH] =0.3 mol/L) until a constant weight was reached. For the RCPT, the catholyte solution was 0.8 N NaCl and 0.3 N NaOH, and the anolyte solution was 0.3 N NaOH in freshly de-ionized water. The RCPTs were carried out in the surface-treated concrete specimens for 24, 36, and 48 hours, and a voltage of 20.0V was applied during the test. After the RCPT, pulverized samples were taken from specimens using the dry-grinding technique. The samples were measured for acid-soluble chloride to obtain total chloride content along the specimen depth according to ASTM C1152 [140]. To convert a measured unit to a simulated one, the total porosities of the specimen, which was not pulverized, were obtained from scanning electron microscope (SEM) images according to image analysis techniques (see Figure 5-3) [141]. As an additional experiment, the test specimen was split into two parts. Then 0.1 N silver nitrate was sprayed on the split surface of the specimen to measure the total depth of chloride penetration; see Ref. [142]. Information on the diffusion coefficient of the concrete and the surface treatment is required before simulating ionic profiles of surface treated sample during RCPT. Figure 5-4 shows the algorithm used to calculate the diffusion coefficient from numerical calculations and the experimental measurement. The penetration depth of chloride ions through the specimen can be measured by spraying the silver nitrate, and the numerical simulation is able to compute the penetration depth from

the estimated lower and upper values of the diffusion coefficient. The diffusion coefficient can be numerically obtained by using the bisection method until the calculated penetration depth matches the experimental measurement. A numerical computation is carried out with the intermediate value of the upper and lower diffusion coefficients, and then the simulated penetration depth is compared to the measured one. If the former is higher than the latter, the upper coefficient is updated to the intermediate value. If the opposite is the case, the lower one is changed. The process is continued until the interval is sufficiently small (10^{-15} m^2/s). Based on this method, the diffusion coefficient of concrete (16.0×10^{-12} m^2/s), and polymer-modified cement paste specimens (7.3×10^{-12} m^2/s) were calculated from the separate RCPTs and colorimetric measurements.

5.2.3. Model Prediction versus Experimental Profile

As shown in Figure 5-5(a) and (b), the experimental chloride content at different depths of the specimen are quantitatively similar to the chloride profile simulated by the present model with discrete diffusion coefficients. In addition to the chloride profile, the experimental chloride penetration depths were measured with 0.1 N silver nitrate [see Figure 5-5(b)]. Since the threshold chloride concentration of reacting chloride with 0.1 N silver nitrate is 0.07 N, the penetrated depth values of this concentration in Figure 5-5(a) corresponds to 15.9 mm, 28.3 mm, and 39.5 mm calculated by the present model, and 17.9 mm, 25.5 mm, and 33.5 mm obtained from the single-species model of the pseudo-diffusion coefficient, respectively. Therefore, the present model more accurately predicts the discrete diffusion coefficients and shows better agreement with the results from the experimental penetration depths (16 mm, 29 mm, and 40 mm) after 24, 36, and 48-hour RCPTs [see Figure 5-5(b)].

5.3. Results and Discussion

5.3.1. NPP Model with Discrete Diffusion Coefficients and Single-Species Model with Pseudo-diffusion Coefficient

Buenfeld et al. suggested calculating the pseudo-diffusion coefficient of surface-treated cement systems by using the following simple equation [69].

$$\frac{L_t}{D_p} = \frac{L_s}{D_s} + \frac{L_c}{D_c} \quad \text{and} \quad L_c = L_s + L_c \tag{5.8}$$

where, L_t, L_s, and L_c are the depth of the total specimen, the surface treatment, and the concrete sample, respectively, D_p is the pseudo-diffusion coefficient of the surface-treated specimen, and D_s and D_c are the chloride diffusion coefficients of the surface treatment and the concrete sample, respectively. Equation (5.8) was applied to obtain

the pseudo-diffusion coefficient to conduct the following comparison. The chloride profiles of the surface-treated concrete sample at 36 hours after onset of RCPT (see Figure 5-6) were obtained from the present model, and compared to the results from the conventional single-species model with a pseudo-diffusion coefficient used in previous studies [69, 70, 143]. As shown in Figure 5-6, the single-species model with the pseudo-diffusion coefficient is too simplistic to take into account the effects of the surface treatment on the RCPT and to adequately describe the ionic movements of the surface-treated concrete samples. In addition, because the penetration depths of both models are significantly mismatched, the single-species model might yield erroneous pseudo-diffusion coefficients for the surface-treated specimen.

5.3.2. Ionic Transport and Electric Field during RCPT

Figure 5-7(a) presents the effect of a highly effective surface treatment on the variation of the sodium distribution profile during an RCPT. Sodium ions located near the surface treatment/concrete interface immediately moved toward the interface and, in only a few hours, narrowly grew beyond their boundary concentration. As an effective surface treatment has a much lower diffusivity than concrete, its presence in a cementitious system acts as an enormous barrier to ion permeation. In the case of the sodium ion, its positive ion flux not only tends to migrate toward the cathode cell due to electrostatic attraction, but it is also able to move more freely in the region of the concrete than in the surface treatment area because of higher ionic diffusivity in the concrete. As a consequence the sodium ions reach the interfacial region within a relatively short period of time. In other words, since the sodium flux in the concrete region is significantly faster than that in the surface treatment, a drastic increase in the sodium content is raised in the narrow interfacial region during the initial period of the RCPT as shown in Figure 5-7(a). This sodium content is high enough to affect the sodium distribution profile within the surface treatment even after the initial period of the RCPT, as the increased sodium concentration becomes an interface boundary condition. Thus, the large number of sodium ions within the interfacial region gradually diffuses and migrates toward the cathode side after the initial period of the RCPT, and the interface boundary condition causes the η shape of the sodium profile within the treatment region, as shown in Figure 5-7(a), at 24 hours. With the same mechanism, other cations would also show a similar ionic behavior over time.

The chloride distribution profiles are shown in Figure 5-7(b). During the first few hours of RCPT, there was no sharp increase in the chloride distribution at the interfacial region, as opposed to the initial tendency of sodium ions to concentrate near the interfacial boundary. The reason for this opposite tendency is that chloride ions, with their one negative charge, tend to migrate from cathode to anode, but the only source of chloride ions in the RCPT is the sodium chloride solution of the cathode cell, whereby the chloride ions come into contact with the surface treatment, which has relatively low diffusivity. As a result, the chloride ions are trapped in the catholyte solution during the

first few hours of the RCPT, since they have difficulty migrating through the surface treatment. After the initial period of RCPT, the chloride ion gradually diffuses and migrates through the surface treatment. When it reaches the concrete region, it moves rapidly toward the anode side. During this time period, the interfacial region undergoes a continuous increase in chloride content, until the shape of the chloride distribution profile within the treatment region becomes analogous to the η shape of the sodium distribution profile. However, since the shape of the ionic distribution profiles within the treatment region depends on the effectiveness of the surface treatments, the η shape is raised with highly effective surface treatment. Since a large number of cations are confined to the interfacial boundary during RCPT, they generate a local electric field, which attracts anions to the interfacial region and distorts the overall electric field. Here, the chloride concentrations of the interfacial region increase beyond that of the catholyte [see Figure 5-7(b)]. The electric field along the depth of the surface-treated concrete sample [see Figure 5-7(c)] is significantly distorted during RCPT, and cannot maintain the linear potential gradient of the externally applied voltage.

The electric field does not immediately respond to the rapid increase in cation concentrations of the interfacial region during the very beginning of RCPT. As the sodium content at the interfacial boundary reaches its maximum concentration, however, the potential profile has a maximum hump near the interfacial region at around the 5-hour mark of the RCPT [see Figure 5-7(c)]. Then, anions clump together with the confined cations at the interfacial region to compensate for the locally-generated field, and the local distortion of the electric field is reduced and distributed all along the depth of the sample.

The ratio of diffusion coefficients of the surface treatment to the concrete D_s/D_c can denote the relative effectiveness of the surface treatment to prevent chloride diffusion. Figure 5-8(a) and (b) shows the sodium and electric potential profiles with different effectiveness (D_s/D_c = 2, 5, and 10) of the surface treatments at 5 hours after the beginning of RCPT, whereby the cation content near the interface is raised to maximum concentrations [see Figure 5-7(a)]. As shown in Figure 5-8(a) (see the upward-pointing arrow), as the effectiveness of the surface treatment increases, higher sodium concentrations were observed in the interfacial region at the 5-hour mark during RCPT. In contrast to the interfacial region, the sodium content decreases at the downward-pointing arrow in Figure 5-8(a) as the surface treatment is more effective. Since the highly effective surface treatment restricts ionic movements within the interfacial region, with higher effective one more ions are accumulated within the interfacial region instead of moving to other regions due to diffusive force. Consequently, the sodium content at the downward-pointing arrow in Figure 5-8(a) is reduced to supply more ions to the interfacial region. These suggested ionic interactions are expected to influence the electric field along the sample depth and, indeed, such a mechanism was observed in the simulations reported herein. In Figure 5-8(b), note that the electric field was more distorted in direct relationship to the more effective surface treatments, and its distortion is likely to be proportional to the increase in sodium concentrations in the interfacial

region.

5.3.3. Prospective Application of the Model and Algorithms

Accurate measurement and analysis of ionic diffusivity in cementitious materials is crucial to evaluate the service life of RC structures near or in saline environments. Particularly, since many RC structures located in marine environments have been treated with the protective materials, their measurement and analysis become more complicated. The consequences of misunderstanding the effect of the surface treatment on the measurement and calculation of diffusivity can lead to a significant increase in maintenance or replacement costs, or endanger the safety of the structure by overestimating its service life. The proposed numerical model provides a more accurate method to simulate ionic profiles through a surface-treated concrete specimen, as well as to compute the diffusion coefficient from RCPT. Based on the algorithm in Figure 5-4, the accurate diffusion coefficient of various surface treatments can be measured from two separate RCPTs of non-treated and surface-treated concrete specimens, even using extremely thin surface treatments, such as pore blockers and pore liners. Although, based on our study, further research is necessary to identify the detailed effects of various types of surface treatments on ionic transport, this study first depicted ionic flocculation and electric distortion through a surface-treated concrete specimen during RCPT, and then provided a way to incorporate the present model with colorimetric measurement,

5.4. Conclusions

In this chapter, based on the extended NPP model, a numerical model was developed to simulate the effects of surface treatment on the ionic movement and electric field of a treated concrete specimen. In the numerical method, the FEM procedure was modified by reconsidering the usage of the uncoupled algorithm. The model was validated by RCPT experimental data. This study was motivated by how experimentally difficult it is to measure the electric potentials of pore solutions along the specimen depth and ionic profiles within a narrow interfacial region. During the first few hours of RCPT, cations accumulate at the interfacial region, and anions are trapped in the cathode cell due to the low diffusivity of the effective surface treatment. As a result of the increasing cation content at the interfacial region, the electric potential field is distorted instead of maintaining a constant potential gradient. After the first few hours of RCPT, the anion content increased at the interfacial region due to electro-neutrality, increasing chloride concentrations in this region beyond the boundary condition of the cathode cell. Concurrently, the local electric field was reduced and distributed all along the specimen. The profile variations of these ionic movements and electric distortions were so interactive as to render the single-species model with a pseudo-diffusion coefficient inappropriate to describe the chloride penetration through the surface-treated cementitious sample during RCPT. A sophisticated model is required to determine the diffusivity of the surface treatment during the duration of RCPT. The proposed numerical

model and algorithms in this study make it possible to compute accurate diffusivities of the surface-treated concrete.
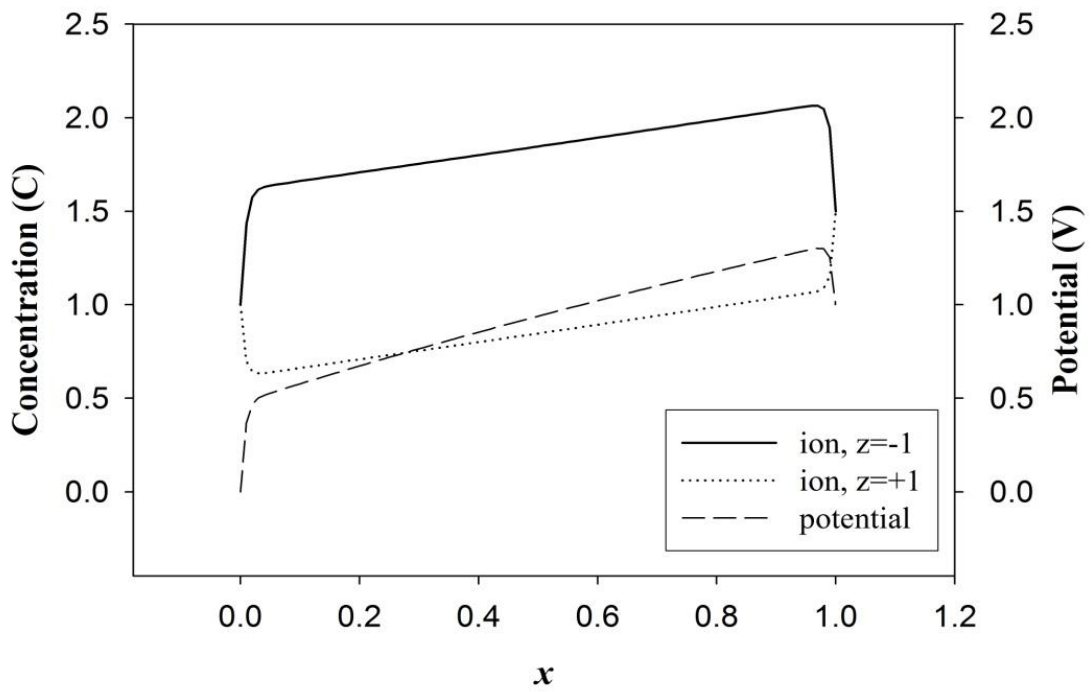
Figure 5-1.Uncoupled algorithm: solution for α^2=0.0001.
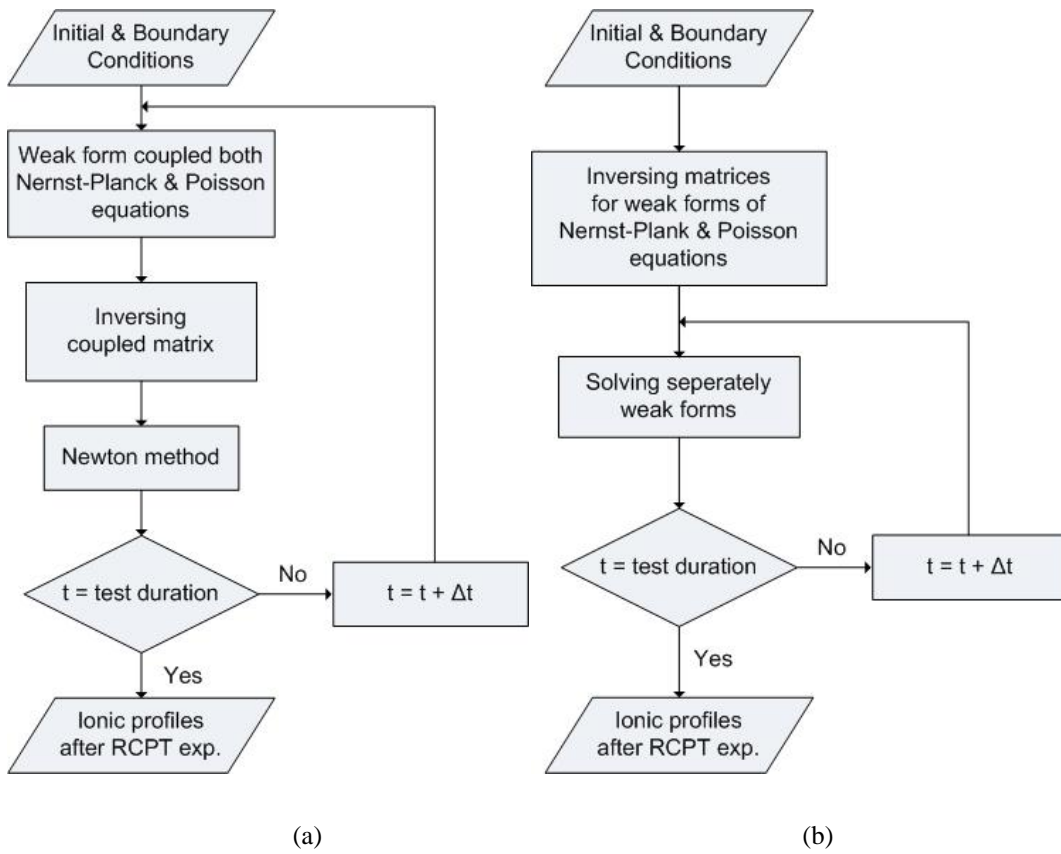
Figure 5-2. Flow charts: (a) coupled algorithm (b) algorithm for the present model.
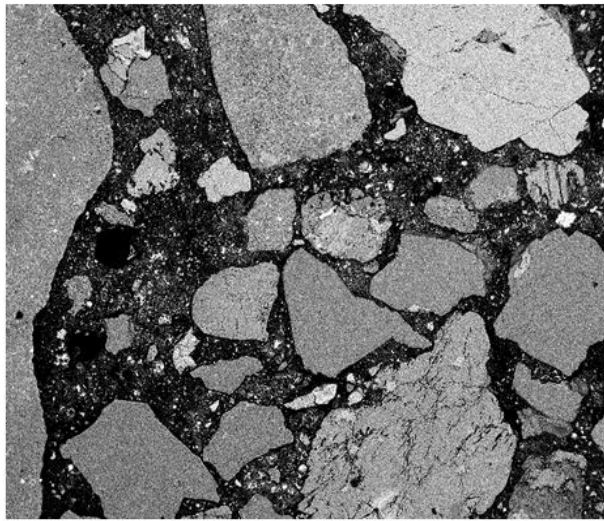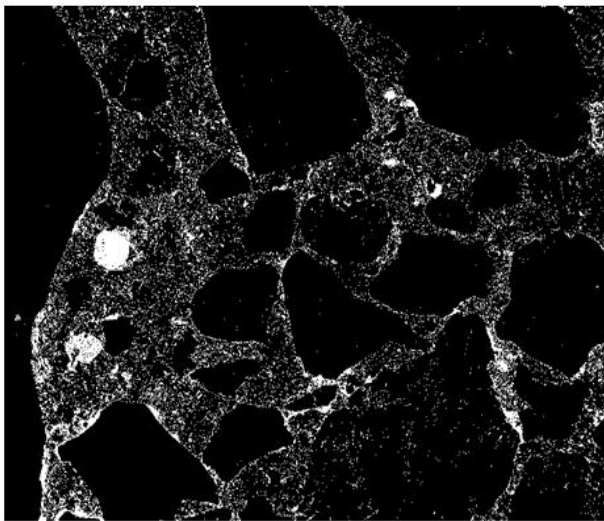
Figure 5-3. (a) Backscatter SEM image showing representative area of the concrete specimen; and (b) after undergoing binary segmentation to show the pore space (white) pixels.
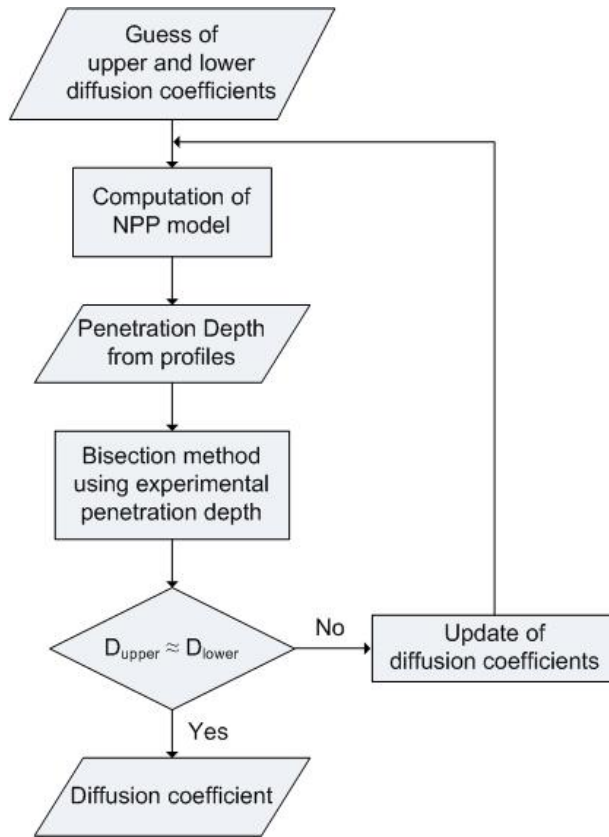
Figure 5-4. Flow chart to determine a diffusion coefficient from the present model and colorimetric measurement.
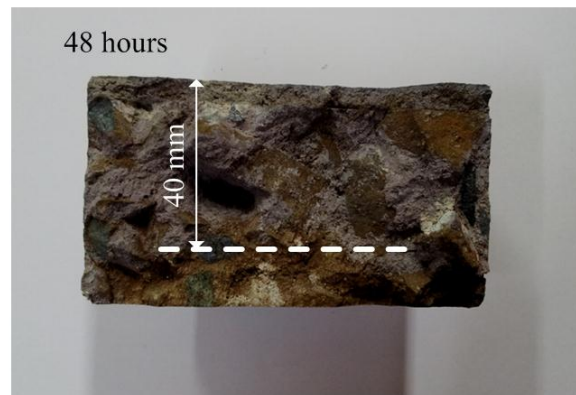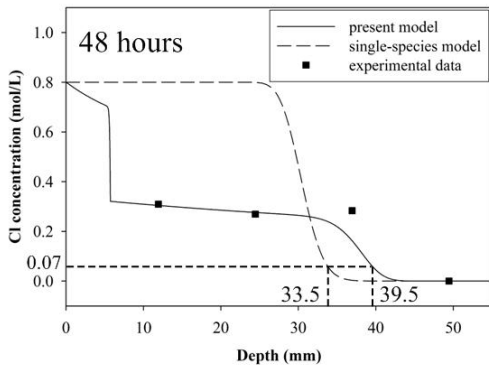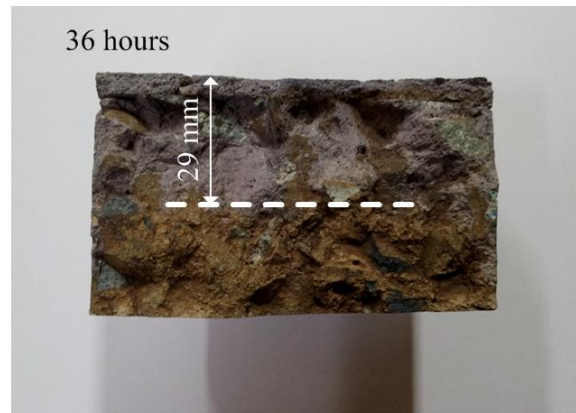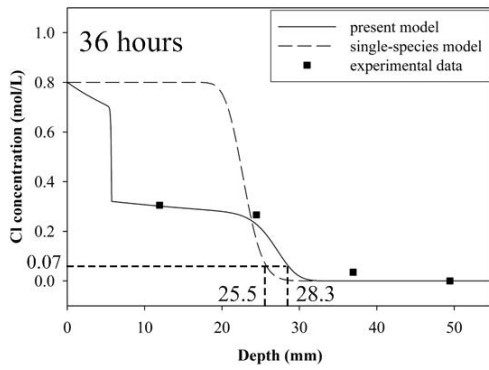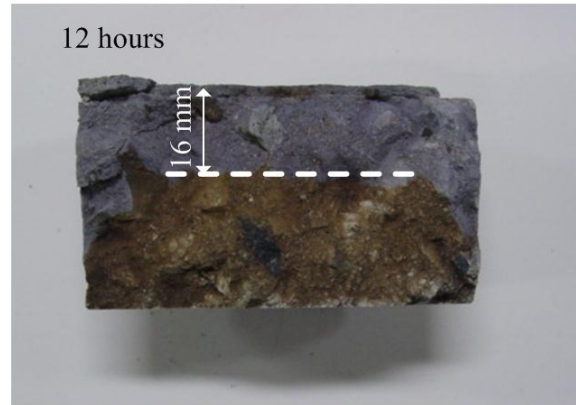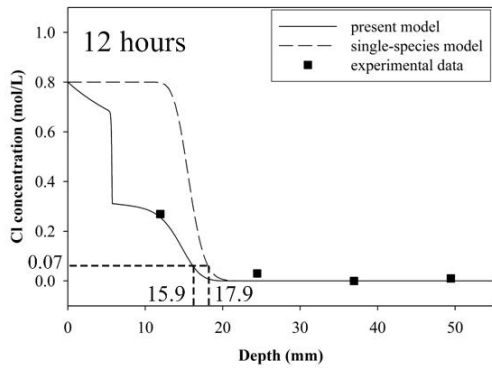
Figure 5-5. (a) Comparisons of experimental data and chloride profiles simulated by the present model and conventional single-species; and (b) colorimetric measurement of the chloride penetration depth after 24, 36, and 48-hour RCPT.
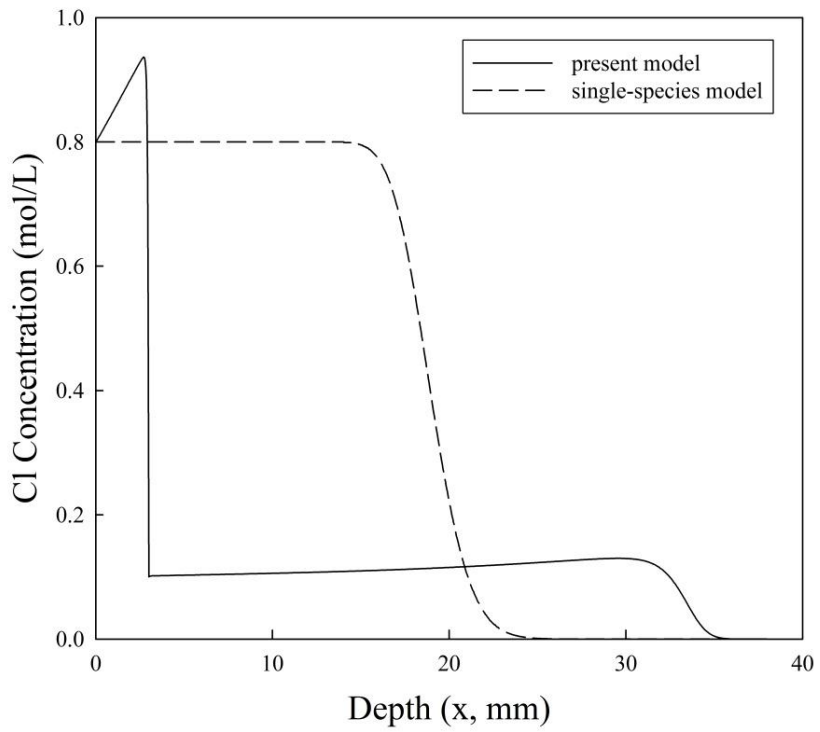
Figure 5-6. Comparison between chloride profiles of the surface-treated concrete specimen simulated by the present model and single-species model at 36-hour RCPT.

(a)
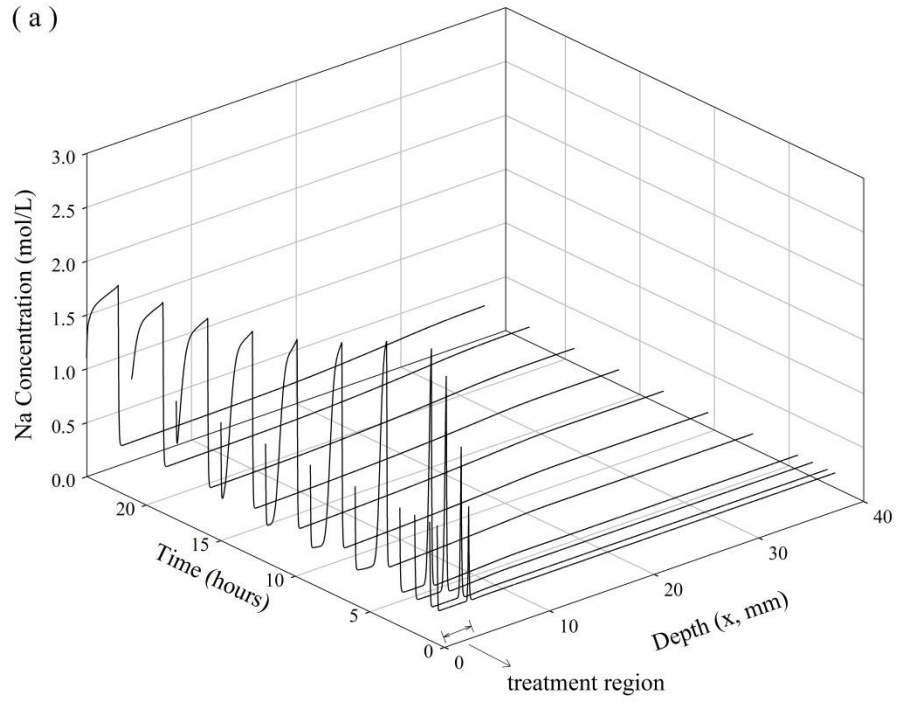
(b)
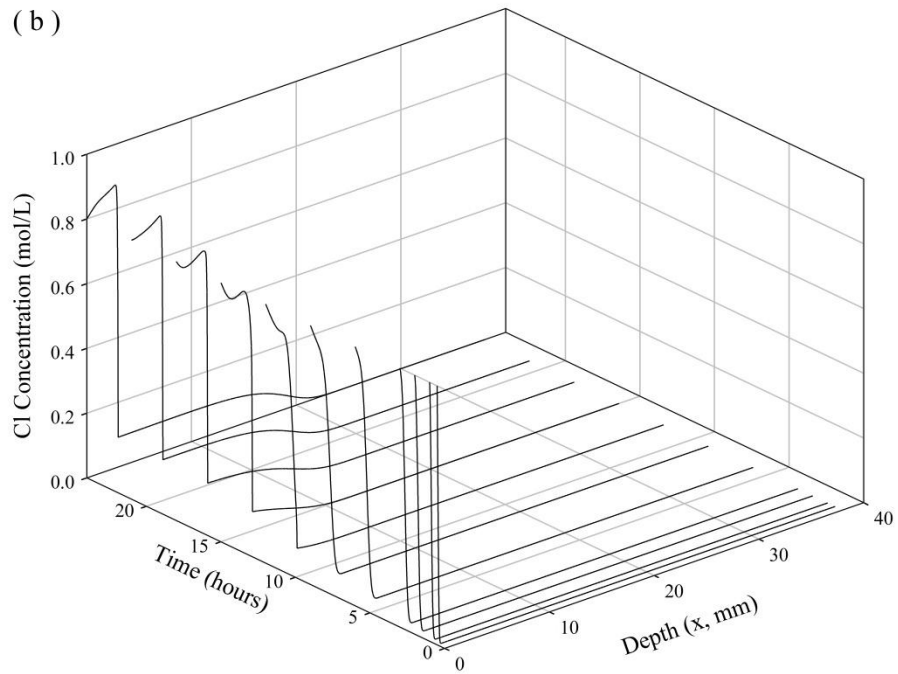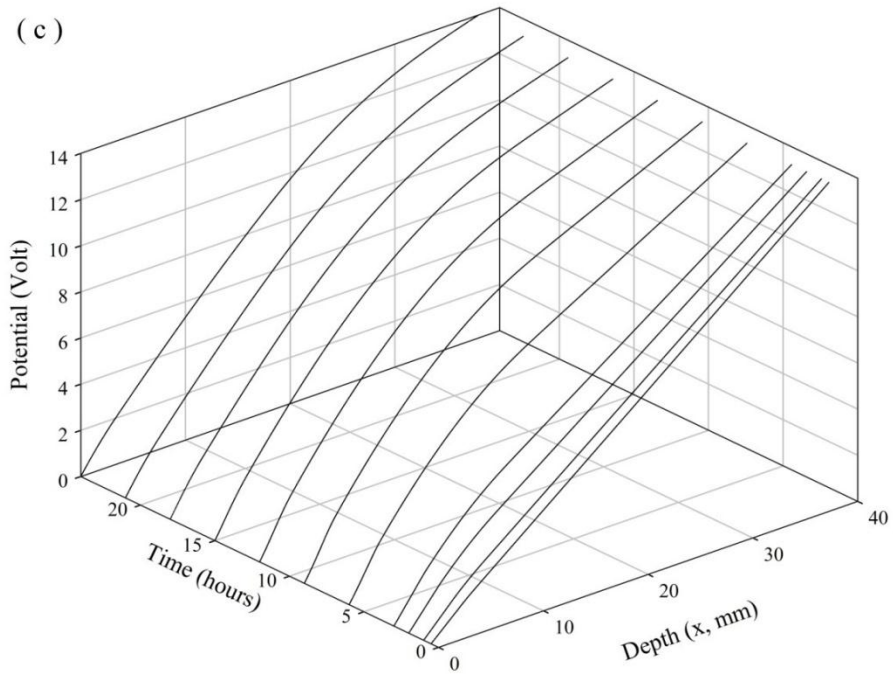
Figure 5-7. Ionic and electric potential profiles inside the surface-treated specimen as a function of specimen depth and time: (a) sodium profile; (b) chloride profile; and (c) electric potential profile.
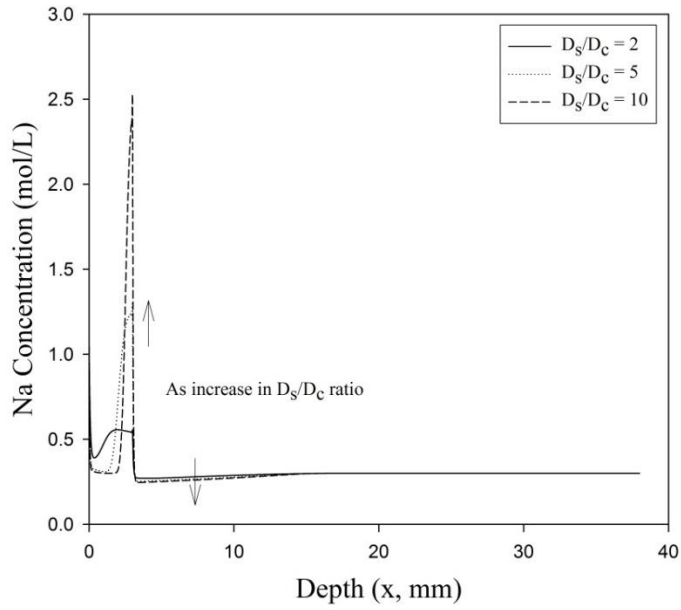
(a)
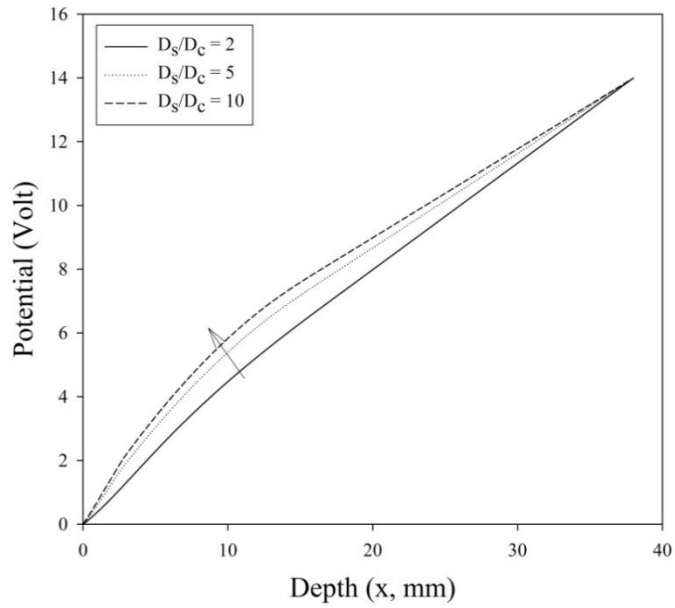
(b)

Figure 5-8. (a) Sodium and (b) electric potential profiles along the depth of the surface-treated specimen in different ratios of surface treatment to concrete diffusion coefficients at 5-hour RCPT.

Table 5-1. Boundary and initial conditions for simulations.

$C_{NaOH}^{cathode}$	$C_{NaCl}^{cathode}$	C_{NaOH}^{anode}	C_{NaCl}^{anode}	$\triangle$Volt
0.3 M	0.8 M	0.3 M	0.0 M	14 V
C_{NaOH}^{init}	C_{NaCl}^{init}	Total depth	Treatment depth	Temperature
0.3 M	0.0 M	38 mm	3 mm	25 ℃

Table 5-2. Detailed concrete compositions.

specimen	w/c ratio	fine/coarse agg. ratio	unit weight (kg/m^3)				slump (cm)
			water	cement	fine agg.	coarse agg.	
concrete	0.6	0.4	185	308	755	1122	12.7

Chapter 6.

Adsorption Mechanisms of Chloride by Calcined Layered Double Hydroxides in Hardened Cement Paste

Layered Double Hydroxides (LDHs) are promising materials for improving the corrosion protection in reinforced concrete. The possibility of having various LDH compositions and lower costs than other protection methods, such as stainless steel and cathodic or anodic protections is technically and economically attractive. As mentioned in Chapter 1, it was recently reported that LDH calcined at around 500°C has a higher chloride binding capacity than the original one with the recovery of its original layered structure due to the so-called "memory effect". Based on this interesting finding, the use of calcined layered double hydroxides (CLDH) as a new additive of concrete can better improve the chloride resistance than LDH. However, there is no previous research that examined how the cementitious environment affects the adsorption isotherms, the memory effect, and the dominant process for the chloride adsorption by CLDH.

The primary objective of this chapter is to provide information to assess the plausible use of CLDH against the chloride-induced deterioration in reinforced concrete structures. Therefore, the equilibrium and kinetics of the chloride uptake by CLDH-admixed cement pastes were investigated to determine the adsorption isotherms for cementitious systems. The adsorption process in the cement matrix may be different from that in aqueous solution. Therefore, based on the adsorption rate and a Fickian diffusion model, the chloride adsorption by CLDH through the cement matrix was simulated and then compared with an X-ray fluorescence (XRF) map. Using XRD, this chapter examined whether the CLDH has the memory effect in the cementitious system.

6.1. Mathematical Model for Chloride Transport in Cement Paste with the Inclusion of CLDH

The study in this chapter attempts to simulate the effect of CLDH on the chloride profile over the cement matrix that initially contained uniform chloride contents. Without the external voltage, chloride transport in the cementitious system can be modeled by a Fickian diffusion model [144]:

$$\frac{\partial C}{\partial t} = \nabla \cdot \left(D_t \nabla C \right) - r_t \tag{6.1}$$

where, C is the chloride concentration at time t, and r_t is the adsorption rate at time t. As mentioned in the previous chapter, most advanced models include electro-neutrality in

the presence of ionic charges, however here it is reasonable to use the Fickian diffusion model to simulate the chloride transport in cement paste influenced by CLDH. Ionic interactions have a minor effect on the chloride diffusion process without externally applied voltage, with the adsorption process being a dominant condition in the ionic transport. Wang et al. [145] studied the structure and dynamics in the interlayer of ordered Mg/Al Cl-LDH ([$Mg_3Al(OH)_8$]Cl·$3H_2O$) with molecular dynamic simulation and far-infrared spectroscopy (FIR) and observed that interlayer chloride motions are remarkably similar to free chloride motions in aqueous solution due to the similarity of the nearest- neighbor of the chloride in the interlayer and the solution. Therefore, in the simulation reported herein, it is assumed that adsorbed chloride ions are homogeneously distributed over the CLDH particle, reflecting the active movements of chloride ions in the interlayer space.

Integrating Equations (1.22), (1.24), (1.25), and (1.27), allows for solving Equation (6.1) using the finite element method (FEM) due to the time variation in the diffusion coefficient and the adsorption rate. To derive the numerical model, the equation is applied to the Galerkin method by using the virtual concentration (δC) over the domain (Ω):

$$(\delta C)\frac{\partial C}{\partial t} = (\delta C)\nabla \cdot (D_t \nabla C) - (\delta C)r_t \qquad (6.2)$$

By applying the divergence theorem and the explicit scheme, the numerical model is expressed as:

$$\{C\}^{t+\Delta t} = \left\{[I] - \frac{D_t}{\Delta t}\left[\int_\Omega [N]^T[N]d\Omega\right]^{-1}\left[\int_\Omega [B]^T[B]d\Omega\right]\right\}\{C\}^t - \left\{\int_\Omega [N]^T d\Omega\right\}r_t \quad (6.3)$$

where, *[N]* is a shape function, *[B]* is a derivative of the shape function, and *[I]* is an identity matrix. The above model is now applied to predict the uptake of chloride ions from cement paste when a CLDH particle is placed on the center of an infinite cement matrix. As shown in Figure 6-1, because the concentration gradients in the cement matrix are highest near the cement-particle interface, a variable mesh density is used, whereby the density of the mesh increases in the cement matrix near the interface. This is done to increase accuracy and reduce computational time.

6.2. Experimental Procedure

6.2.1. Materials

The Mg/Al LDH (PURAL MG 63 HT, Mg:Al = 2.15:1) used for preparing CLDH was supplied by the SASOL GmbH, Germany, and CLDH was obtained by calcining the precursor LDH in a muffle furnace at 450 °C for 3 hours. The cement paste specimens

were made from ASTM Type I Portland cement, the composition of which is listed in Table 6-1. The percentage of CLDH used as an admixed inhibitor against chloride attack was 8.5 % by the total mass of the solid pre-calculated to absorb approximately 2 % of chloride content, which reflected the boundary content of the concrete specimen exposed to seawater for 2 years (see ref. [146]). To assess the effect of CLDH, control specimens of cement pastes that did not contain CLDH were also prepared for every mix design. Chloride levels were managed by using 0.3, 0.6, 0.8, 1, and 3 M NaCl solutions as mix water, obtaining homogeneous chloride contents for all specimens (see refs. [39, 147, 148]). A solution-to-solid ratio of 0.4 was considered to be the benchmark. For each mix, two cylindrical specimens (Ø 2.5 cm × 2.5 cm)—one the control and the second the CLDH specimen—were cast and steam-cured at 20 °C for all test ages. Therefore, the numbers of specimens were 20 and 24, respectively, for the equilibrium and kinetic studies.

6.2.2. Equilibrium and Kinetics

The equilibrium isotherms were carried out by using 0.3, 0.6, 0.8, 1, and 3 M NaCl solutions as mix water. With each chloride level of the solutions, four specimens were prepared: two for the control and two for the CLDH specimens. All specimens were cured over 28 days, which is acknowledged as not being the exact time required to reach perfect equilibrium; however, this assumption was made because a 28-day curing period has been commonly used as the standard to reach equilibrium in hydration kinetics [149]. The final concentration of free chloride in the cement paste was determined by following ASTM C 1218 [150]; therefore, pulverized samples were removed from the cement paste by using the dry-grinding technique and measured for water-soluble chloride using a chloride meter for concrete provided by DAE YOUNG WIRE Co., LTD. The chloride loading for CLDH specimen was calculated from the following equation:

$$q_e = \frac{(C_0 - C_e)M}{m} \times \frac{1000}{100} \left(\frac{mg}{\%\ cement} \right) \tag{6.4}$$

where q_e is the adsorption loading of CLDH at equilibrium (mg/g), m is the mass of CLDH in each specimen (g), M is the total mass of one specimen (g), and C_0 and C_e (% cement) are the chloride concentrations of the control and cement-CLDH specimens, respectively. Since the measured unit of chloride contents in the cement paste is percentage by mass of cement (% cement), the total mass of the specimens (M) was used instead of the volume of the solution, which is the method commonly used in other equilibrium studies.

The kinetic study used 0.1, 0.3, and 0.6 M NaCl solutions as mix water. Using an identical procedure as that outlined for the equilibrium study, the chloride contents were measured at 1, 3, 7, and 28 days. Control specimens were also prepared and cured under identical conditions. The measured specimens were subjected to additional experiments

using XRD, X-ray fluorescence (XRF), and SEM. Chloride uptake by CLDH was calculated using the following equation:

$$q_t = \frac{(C_0 - C_t)M}{m} \times \frac{1000}{100} \left(\frac{mg}{\%\ cement} \right) \tag{6.5}$$

where q_t is the adsorption loading of CLDH at time t (mg/g), m is the mass of CLDH in each specimen (g), M is the total mass of one specimen (g), and C_0 and C_t (% cement) are the chloride concentrations of the control and experimental specimens at time t (days), respectively.

CLDH (0.1 g) were dispersed in 20 mL of chloride solutions and stirred for 6 days at room temperature in sealed tubes. Five mL aliquots were extracted at selected time intervals and filtered. The chloride concentrations in the solution were measured using a selective electrode for chloride ions. The chloride uptake by the CLDH was calculated from the following equation:

$$q_t = \frac{(C_0^a - C_t^a)V}{m} \tag{6.6}$$

where V is the volume of solution (L), and $C^a{}_0$ (mg/L) and $C^a{}_t$ (mg/L) are the initial concentration of chloride and that at time t, respectively.

6.2.3. Hydration Rate Constant

The LOI non-evaporable water content measurement was performed according to the procedure described in Ref. [151]. The non-evaporable water content of the 7-day specimen was obtained by measuring the relative mass loss between 105 and 1000 °C, and then correcting for the LOI of the dry cement powder. A value of 0.25 g H_2O/g cement—the non-evaporable water content for a fully hydrated sample—was calculated based on the Bogue equations and the chemical composition of the cement, as shown in Table 6-1. The degree of hydration ($\alpha = 0.588$) was then estimated as the ratio of the measured non-evaporable water content to the amount for a fully hydrated specimen. The time, $t = 7$ days, and the degree of hydration were substituted into Equation (1.27) to obtain the hydration rate constant ($k = 0.03$ h^{-1}), which was used in further simulations conducted in the present study.

6.2.4. Other Techniques

The XRD patterns of the samples were obtained using a PANalytical X'Pert Pro diffractometer with a Cu Kα (λ=1.5418 Å) incident radiation. The data were collected from 5 to 70°. The composition maps on the cement paste and admixed CLDH of the 7-day specimens were obtained using Orbis Micro-XRF provided by EDAX. To reduce the

possibility of significantly misrepresenting the chloride distribution on the specimen, a relatively flat area of the split specimen was measured; no additional treatment on specimen, such as polishing, was performed. To study the morphological features of the powdered CLDH and reformed CLDH included in the cement paste, SEM was conducted using a CAMECA SX 100 and gold-coated specimens.

6.3. Results and Discussion

6.3.1. Equilibrium Study

Determining the equilibrium isotherm is important to optimize the use of adsorbents. The correlation between equilibrium data and isotherms leads to developing a better model that represents well the quantity and operation of adsorption system. In this section, the quantity of the chloride removals by CLDH in cement paste (q_e) are scattered against the chloride concentration equilibrated in the control specimen (C_e) [see Figure 6-2(a)]. Two general-purpose equilibrium models are considered to fit the experimental data: (a) Langmuir's [152] model, shown in Equation (6.7), and (b) Freundlich's [153] model, shown in Equation (6.8).

$$q_e = \frac{QbC_e}{1+bC_e} \qquad (6.7) \qquad\qquad q_e = K_F C_e^{1/n} \qquad (6.8)$$

where, Q and b are the Langmuir constants, K_F and n are the Freundlich constants, C_e is the chloride concentration equilibrated in the cement paste (% chloride by weight of cement), and q_e is the adsorption loading at equilibrium (mg/g).

Figure 6-2(a) shows that the Langmuir isotherm fits the experimental data more satisfactorily than the Freundlich isotherm does, suggesting that the adsorption process takes place at specific homogeneous sites within LDH as assumed by the Langmuir equation. The best-fit Langmuir parameters are $Q = 153.1$ mg/g and $b = 0.418$ % cement. The evaluated chloride uptake in the cement matrix (153.1 mg/g) is much less than the stoichiometric calculation (257.2 mg/g), implying that other anions in the cement paste pore solution might be adsorbed into CLDH as well by competing with chloride ions.

6.3.2. Kinetic Study

To determine the appropriate isotherm, three general-purpose kinetic models were compared with the experimental data. The key features of the kinetic models used in the present study are summarized as follows:

Pseudo first-order kinetics model: The pseudo first-order kinetics model suggested by Lagergren [154] is given by the following linear equation:

$$\ln(q_e - q_t) = \ln q_e - k_1 t \tag{6.9}$$

where k_1 is the rate constant of adsorption (days^{-1}), and q_e and q_t are the amount of chloride adsorbed at equilibrium and at time t (days), respectively. Plotting $ln(q_e\text{-}q_t)$ versus t results in a straight line, and its slope is the rate constant, k_1. Figure 6-2(b) shows the fitted model compared to the experimental data.

Pseudo second-order kinetics model: The pseudo second-order model [155, 156] also illustrates the kinetics of sorption in the solid/liquid systems. The linearly expressed equation is as follows:

$$\frac{t}{q_t} = \frac{1}{k_2 q_e^2} + \frac{1}{q_e} t \tag{6.10}$$

where, k_2 (*g/mg* days) is the rate constant of the pseudo second-order kinetics. The rate constant can be calculated from the straight line fitted to the experimental data in Figure 6-2(c).

Elovich equation: the adsorption data may also be analyzed using the Elovich equation [157, 158], whose linear form is:

$$q_t = \frac{1}{\beta} \ln(\alpha\beta) + \frac{1}{\beta} \ln t \tag{6.11}$$

where, α is the initial sorption rate constant (*mg/g* days), and β is the desorption constant (*g/mg*). The constants can be obtained from the slope and intercept of the plot of q_t versus *ln(t)*, as shown in Figure 6-2(d).

Figure 6-2(b), (c), and (d) present the results of fitting the experimental data to the pseudo first-order, pseudo second-order, and Elovich models. The figure shows that the pseudo second-order model is the most suitable in describing the absorption kinetics of chloride by CLDH admixed into the cement paste. Table 6-2 lists all of fitted parameters for the pseudo second-order model. According to the assumptions of the pseudo second-order kinetics model, the chemical interaction between the chloride ions and CLDH is responsible for the binding capacity of the CLDH. The rate constant, k_2, is shown in Table 6-2.

6.3.3. XRD analysis and SEM images

The XRD patterns of two cement pastes specimens—the control and CLDH-cement paste specimen—are shown in Figure 6-6(a) and (b). When CLDH interacts with chloride ions in aqueous solution, the layered structure reconstructs [like the latter feature shown in Figure 6-7 and its XRD pattern is shown in Figure 6-6(c)]. The new peaks shown in Figure 6-6(b) appeared in identical positions of the Mg/Al-Cl LDH in Figure

6-6(c), indicating that the CLDH admixed in the cement matrix also reconstruct the layered structure with anions. Figure 6-7 shows the schematic illustration of the CLDH structure reconstructed with intercalated anions. After LDH is calcined at 500℃, its layered structure disappears (identically to that shown Figure 6-7); its XRD pattern as raw CLDH is shown in Figure 6-6(d). The XRD patterns in Figure 6-6 are evidence that the cementitious environment does not have any effect on CLDH to reform the layer structure of LDH.

The morphology of the raw CLDH and the reformed LDH by adsorbing anions in the cementitious environment is compared in Figure 6-8. The raw CLDH in Figure 6-8(a) has plate-like particles with sharp edges, in addition to some particles that are settled with well-defined hexagonal shape but no defined orientation. After adsorbing anions from the cement matrix, the materials appear to be constituted of well-defined lamellar shapes stacked on top of each other. In addition, it can be seen from Figure 6-8(b) that the edges of the reformed LDH in the cement paste are more irregular than those of the raw CLDH. In addition, their crystalline sizes have increased compared to the smaller particles of the raw CLDH. Clearly the growth of the crystal was not homogeneous for all particles.

6.3.4. Chloride Adsorption Mechanism by CLDH in Cementitious Environment

The 7-day cement paste/CLDH specimen immersed in 0.6 M NaCl solution was subjected to additional testing to explore the chemical distributions in the middle of the adsorption process before an equilibrium state is reached. The composition maps for Mg, Al, Si, Cl, S, K, and Fe elements were determined by XRF in terms of oxide weight percent over the selected region of the specimen. Based on Mg, Al, and Si maps shown in Figure 6-3, the Mg/Al ratio and the weight percent of SiO_2 confirm that the particle is CLDH, and that the outer region surrounding the particle is cement paste (see Figure 6-3). The Cl, S, K, and Fe maps (Figure 6-3) show that CLDH is remarkably effective in adsorbing anions without adsorbing cations from the cement paste pore solution. The Cl map reveals remarkable differences in the chlorine content between CLDH and the cement matrix, indicating that CLDH is an effective absorbent that prevents chloride-induced deterioration in reinforced concrete. Although the weight percent of SO_3 is higher than that of Cl_2O absorbed into the CLDH particle (see Figure 6-3), the molar percent of S and Cl is analogous when the unit is converted from oxide weight to molar percent. Because gypsum—one of the main ingredients of cement—is the source of sulfate, the high sulfate content of the cement matrix means that the sulfate competes with chloride to be adsorbed into CLDH.

A numerical simulation of the process of chloride adsorption by CLDH in a cementitous environment was conducted and is shown in Figure 6-4 (a), (b), and (c). Figure 6-4(d) shows the upper surface (three-dimensional) plot of the chlorine distribution obtained from the XRF map over the area of the microscopic image on the

bottom plane. The simulated chloride distribution of 7-day specimens in Figure 6-4(c) is in good agreement with the distribution measured with XRF in Figure 6-4(d). Interestingly, the chloride contents are rapidly removed in the cement-matrix regions adjacent to the CLDH particle, and subsequently, the regions influenced by CLDH expand to the outer regions over time. Due to the tortuous pore structure of the cement matrix, it is difficult for chloride ions to freely move in cement matrix—unlike in the aqueous solution—reflecting the low ionic diffusivity of cement-based materials. For this reason, it takes a long time for chloride ions to diffuse into the region influenced by CLDH particles. Hence, the slow ion transport causes the region of the cement matrix adjacent to the CLDH particle to have lower chloride content than its bulk region, slowing down the adsorption rate. To thermodynamically compensate for the deficient chloride contents of adjacent regions, over the long term chloride ions in outer regions away from CLDH are slowly transported to the regions adjacent to CLDH, thereby reducing the overall chloride contents of the cement matrix.

Following the experimental method mentioned in section 6.3.2, we have also studied the kinetics of chloride uptake by CLDH in aqueous solutions to compare it to that in cement paste. Figure 6-5 shows the comparison of adsorption kinetics in cement paste and aqueous solution. The adsorption rate in the cement paste is much slower than that in aqueous solution at the early stages of adsorption. While the adsorption in solution reaches a plateau quickly, CLDH continues to adsorb in the cement matrix. We attribute the slower kinetics in the cement matrix to the rate-limiting diffusion process. Thus we expect the adsorption rate to vary with the different pore structure of the cementitious materials. The reconstructed LDHs have a similar structure in both the cement paste and aqueous solution, suggesting that the cementitious environment has no effect on reforming the layer structure of the LDH.

6.3.5. Application of CLDH to Concrete Technology

Sustainable development of concrete infrastructure is a major challenge in today's construction industry; the use of admixed or supplementary materials is an integral component in addressing this issue. The existence of LDH-like phases in cement matrix, such as AFm phases, has been thought to improve the corrosion resistance of the reinforced concrete structure by preventing chloride-induced deterioration. The beneficial effects of AFm phases on adsorbing chloride from hardened cement supports the idea of using CLDH in concrete as an effective chloride absorbent. Both surface-applied and admixed methods can be employed for the use of CLDH. In fact, Tatematsu et al. [78] plastered the corrosion-inhibiting paste admixed with hydrocalmite—one of LDHs—on the surfaces of ~1-mm-thick reinforced steel bars. Thus CLDH can be also applied in some fashion with hydrocalmite. Because limestone undergoes heat treatment of over 500°C in the manufacturing process of Portland cement, LDH can be transformed to CLDH and admixed to cement powder if LDH goes through the heat treatment simultaneously with the limestone. In other words, there are a variety of ways to utilize

CLDH in the construction industry. This study has demonstrated the effects of CLDH on chloride uptake in a cement-based environment, suggesting that CLDH has potential as a chloride absorbent in concrete.

6.4. Conclusion

An experimental study of the efficacy of CLDH in reducing the chloride content in the cement paste was conducted. The experimental data was fitted using both Langmuir and Freundlich equations to determine the equilibrium isotherm. An evaluation of both models demonstrated that the Langmuir model fit the experimental results to a satisfactory degree, indicating that all adsorption sites are equivalent. The kinetic data were successfully fitted using the pseudo second-order kinetic model. According to the XRD analysis and SEM images, the CLDH admixed in the cement paste not only reconstructed the layered structure with anions, but grew in an irregular morphology. Based on the kinetic study and the Fickian diffusion model, the adsorption process in the cement paste was simulated and compared with a Cl map determined using XRF. The simulation shows that the chloride transport through the cement matrix governs the adsorption rate of CLDH in the cementitious environment, whereas chemisorption of CLDH is the dominant process for aqueous solutions. This study shows that the use of CLHD in cementitous materials has extraordinary potential in preventing the chloride-induced deterioration of the reinforced concrete. Given the results presented herein, future work on the application of CLDH in cementitious materials will proceed rapidly, providing remarkable improvement in the durability of RC structures exposed to saline environments. This study will contribute fundamental information to these further research.
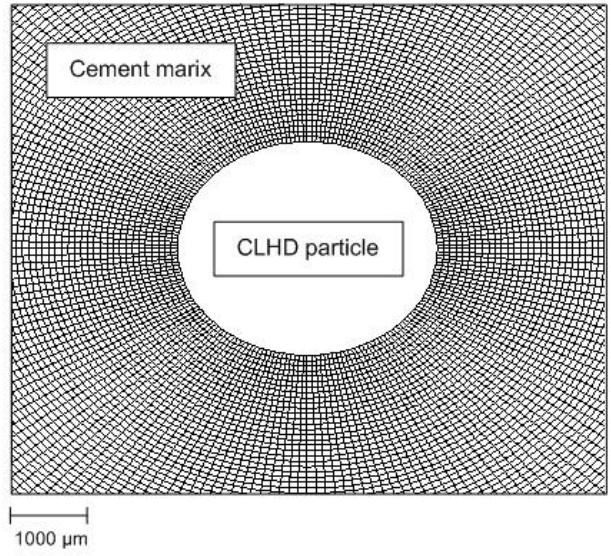
Figure 6-1. Mesh generation of cement matrix with inclusion of CLDH.

(a)   (b)

83
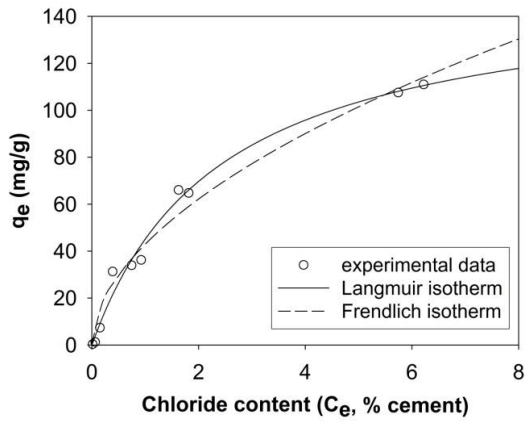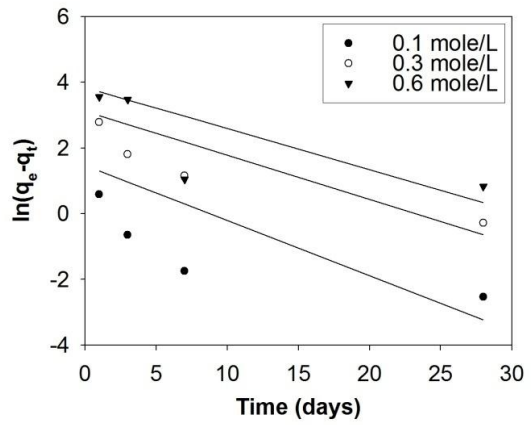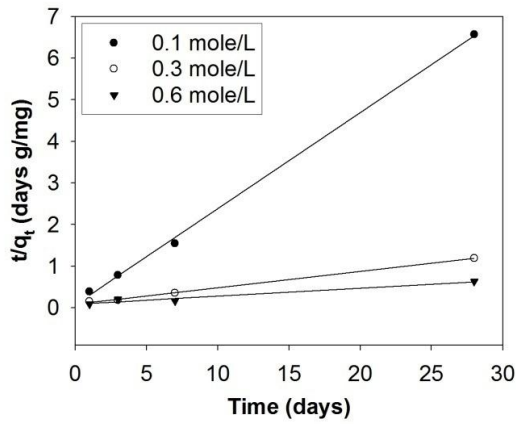
(c)
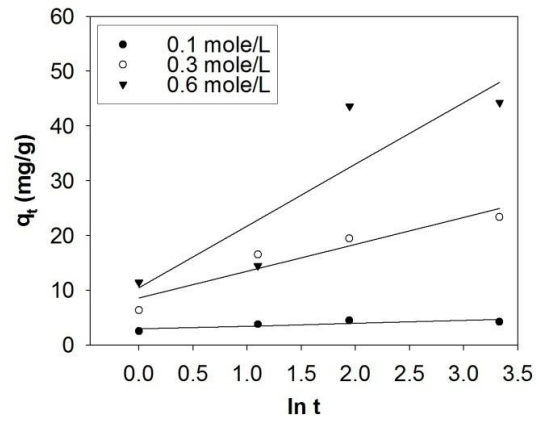
(d)

Figure 6-2. (a) Equilibrium isotherms of the chloride removal by CLDH within the cement paste at room temperature: experimental data (hollow) are fitted to the Langmuir and Freundlich models by solid and dashed curves, respectively; (b) Pseudo-first-order kinetics model; (c) Pseudo-second-order kinetics model; and (d) Elovich equation model: experimental data obtained at 1, 3, 7, and 28 days were measured and fitted to the kinetics models in (b), (c) and (d).
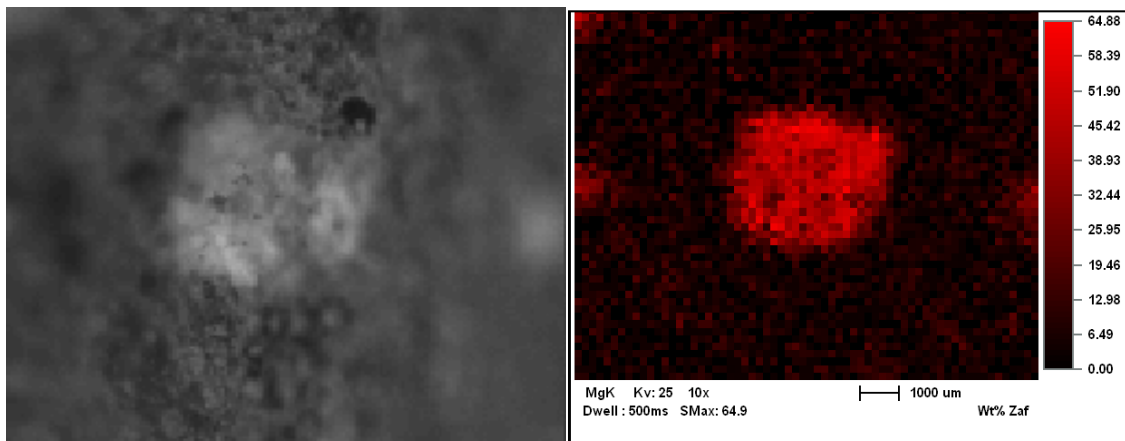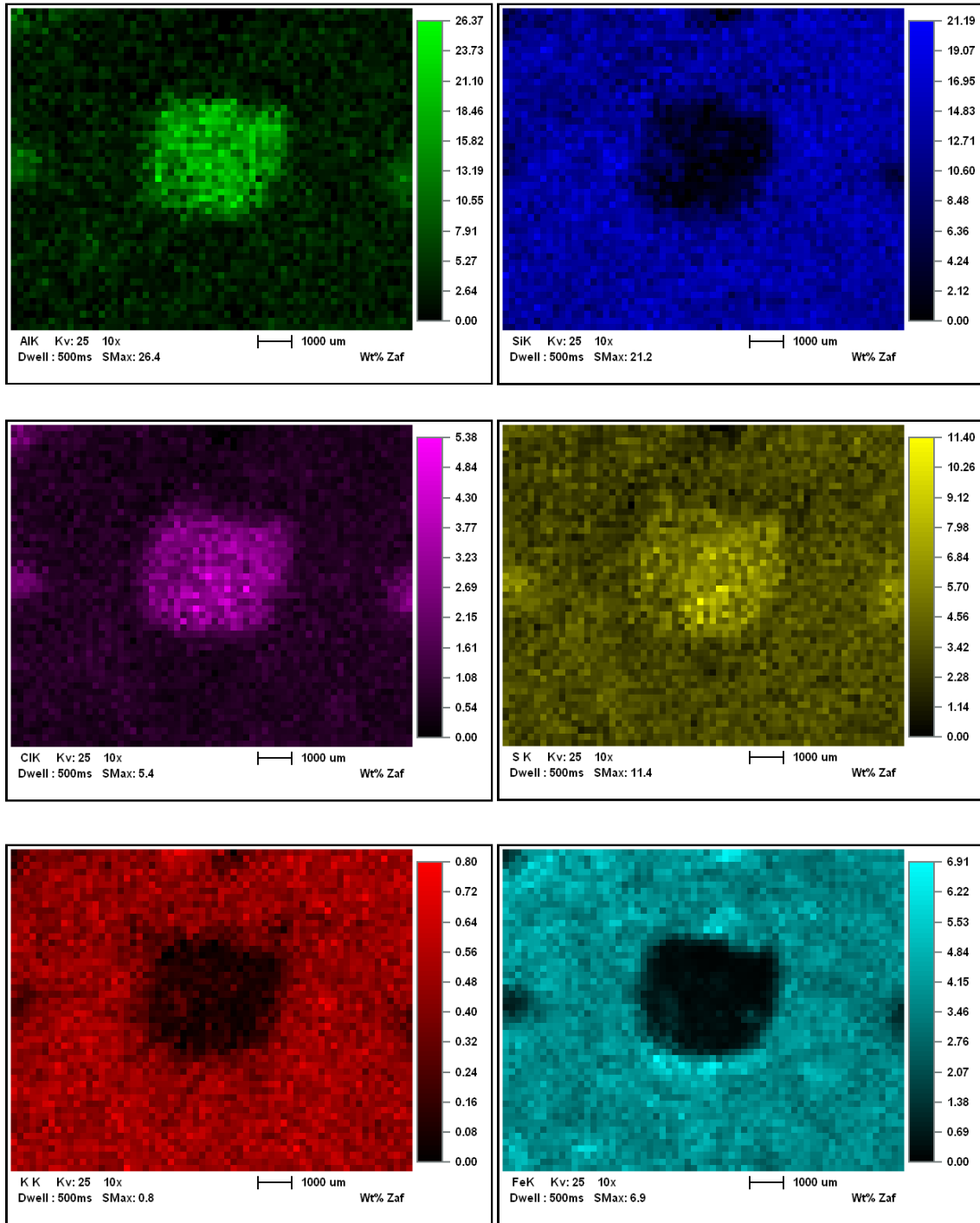
Figure 6-3. Microscopic image and X-ray fluorescence maps showing distributions of elements (Mg, Al, Si, Cl, S, K, and Fe) by oxide weight percent.
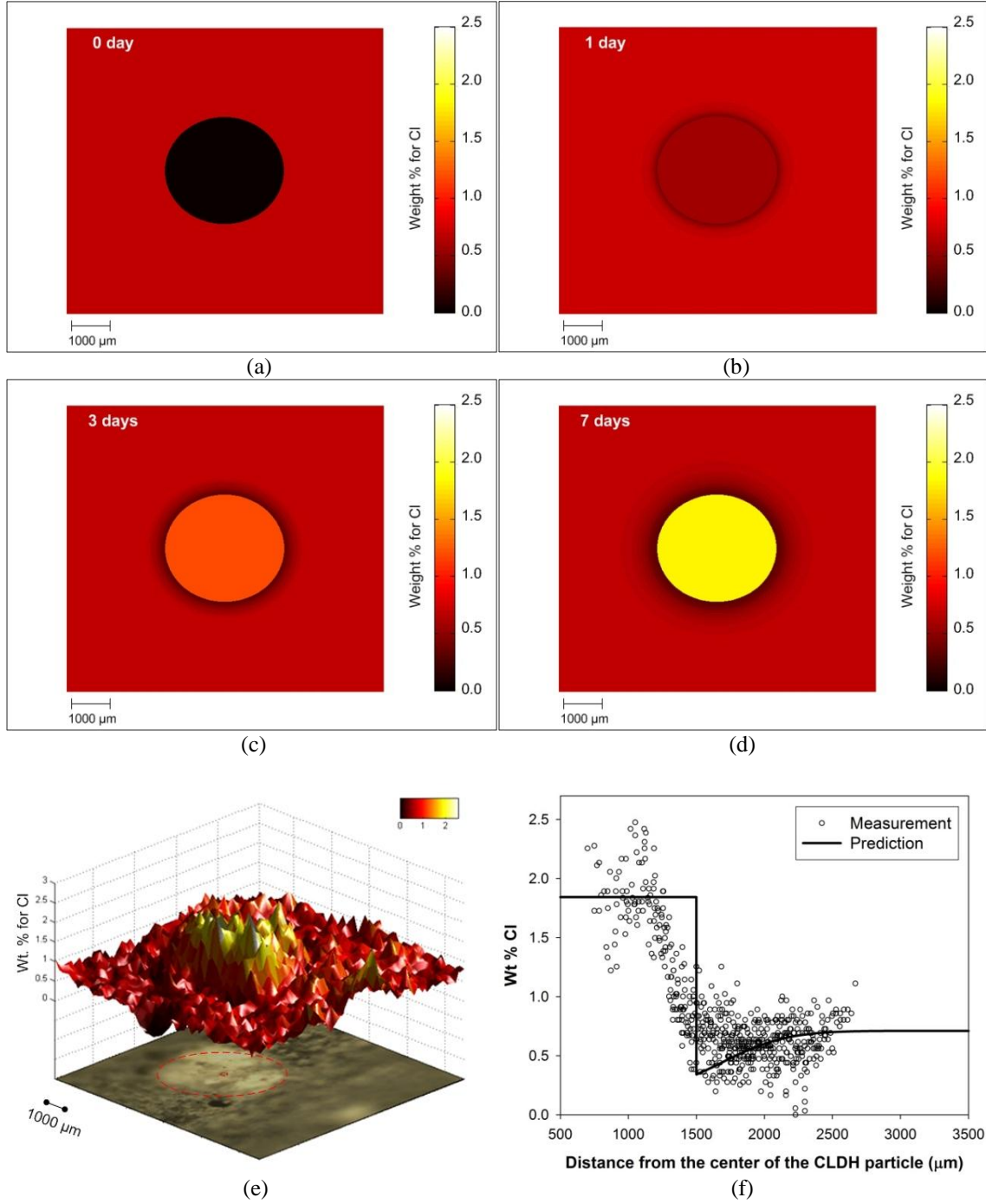
Figure 6-4. Simulation of adsorption process of chloride ions at (a) 0 days (b) 1 day (c) 3 days, and (d) 7days, and (e) Cl XRF map with microscopic image, and (f) comparison between the measurements obtained from (e) and the prediction obtained from (d) in terms of the distance from the center of the CLDH particle.
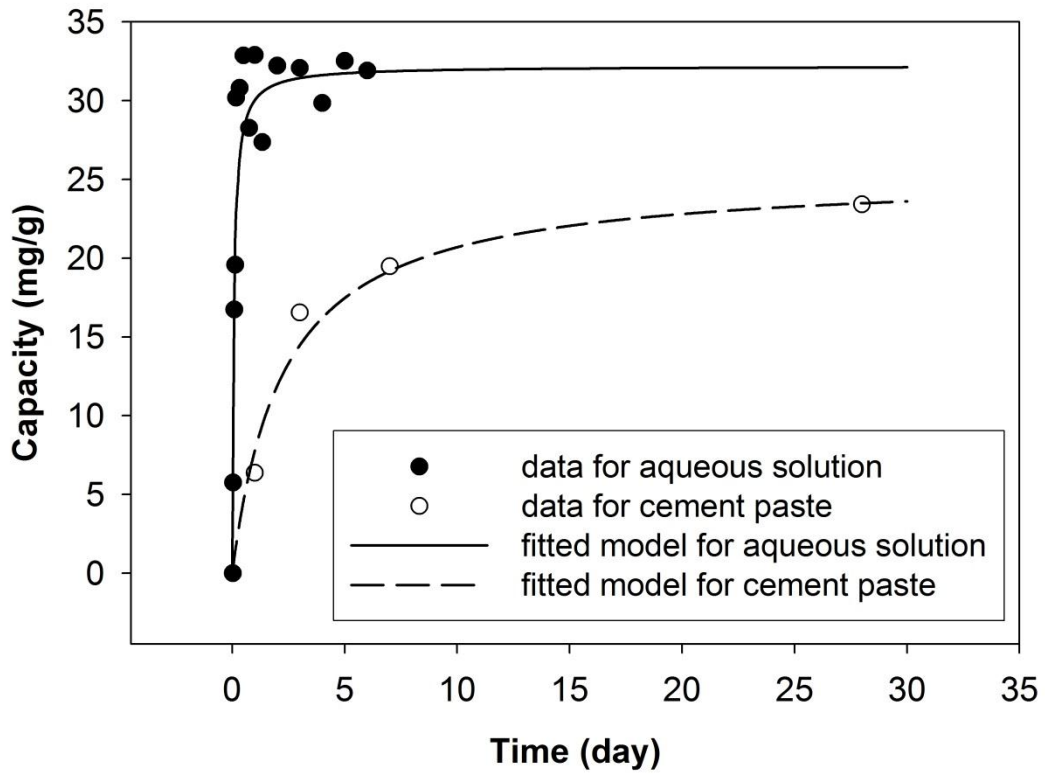
Figure 6-5. The kinetics of uptake of chloride by CLDH in the cement paste and aqueous solution.
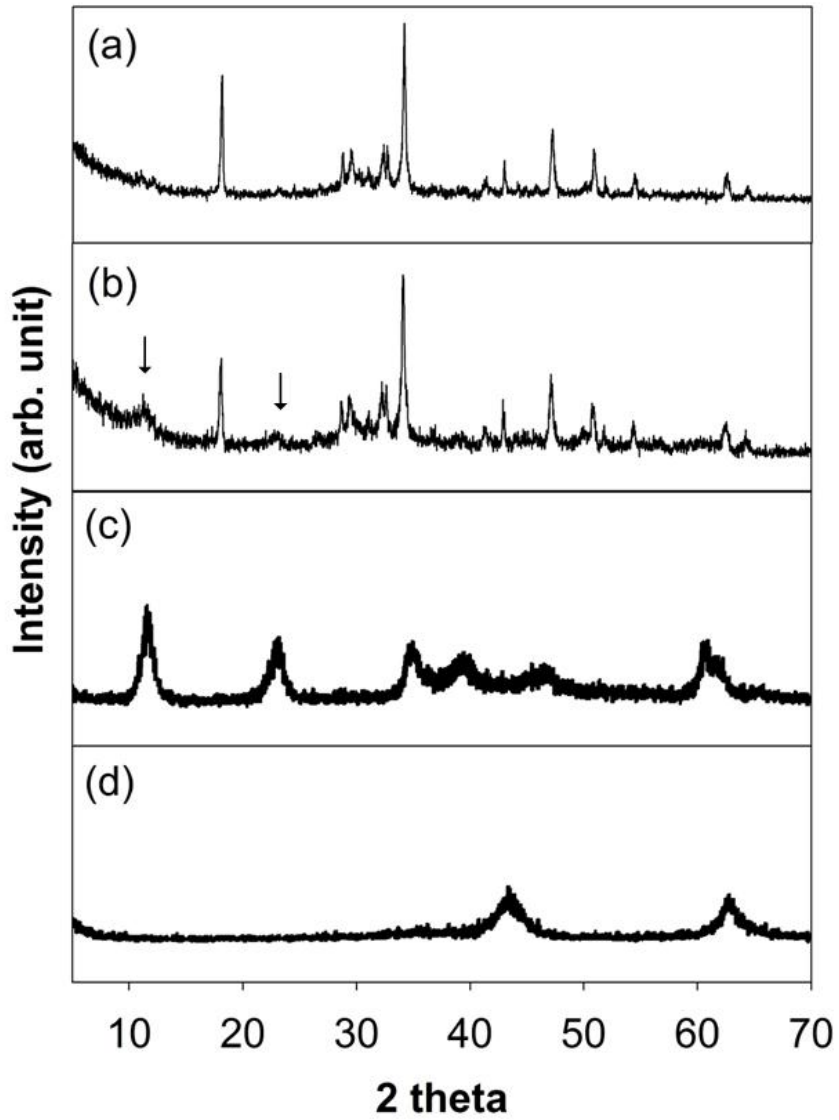
Figure 6-6. Powder XRD patterns: f(a) cement paste without CLDH; (b) cement paste with CLDH; (c) Mg/Al-Cl LDH; and (d) raw CLDH.
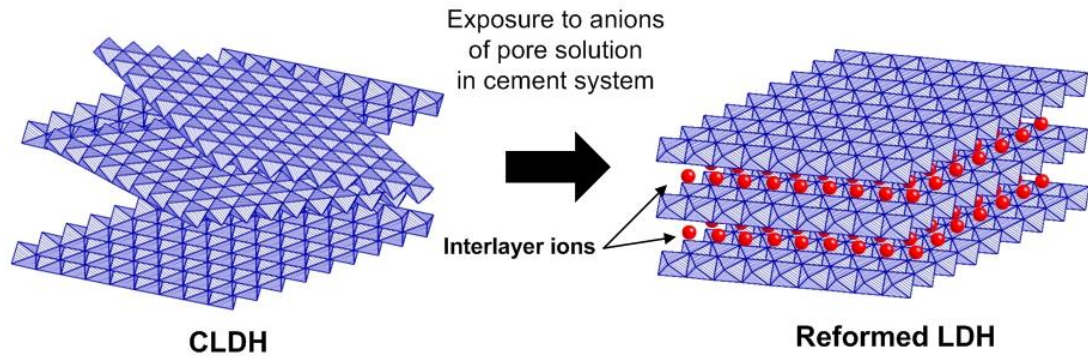
Figure 6-7. Schematic illustration of reforming layered structure of LDH by adsorbing anions.

(a)   (b)
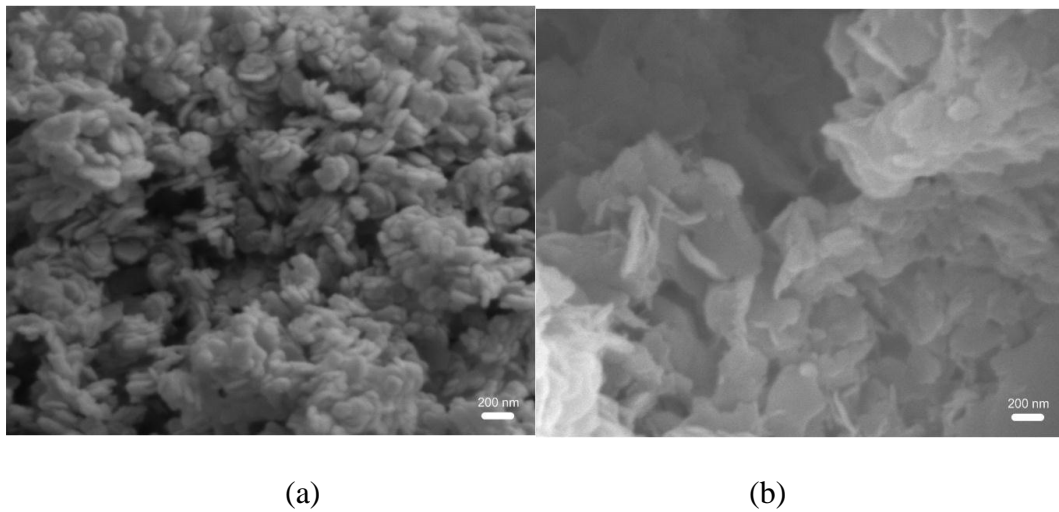
Figure 6-8. SEM micrographs: (a) raw CLDH; and (b) reformed LDH in the cement paste.

Table 6-1. Chemical composition of cement (mass fraction, %).

SiO_2	Al_2O_3	Fe_2O_3	CaO	MgO	K_2O	Na_2O	SO_3	LOI
20.2	5.2	5.5	62.2	1.0	0.7	0.2	4.1	1.5

Table 6-2. Regression coefficients (R^2) and kinetic parameters for the pseudo second-order kinetics model.

[Cl⁻] of mix water (mole/L)	R^2	q_e (mg/g)	k_2 (g/mg days)
0.1	0.9988	4.3309	0.7355
0.3	0.9979	25.3796	0.0174
0.6	0.9559	51.6840	0.0045

Chapter 7. Summary and Conclusion

As presented in Chapter 1, the deterioration of cement-based materials generally occurs via transport and adsorption phenomena, and a significant number of concrete structures and radioactive waste containers have been exposed to aqueous and saline environments. Nevertheless, there are still research gaps with respect to this subject. The work presented in this thesis aims to provide new insights into some of these gaps. To address the research goals, both experimental and simulation research on multiple scales were performed.

Water structure and water transport in 14 Å tobermorite were investigated in Chapter 3. The interlayer water of the C-S-H phases plays an important part in the mechanical properties, creep, and shrinkage of concrete. Since 14 Å tobermorite is often used as one of the structural models for the C-S-H phases, the water structure and transport in 14 Å tobermorite can be used to indirectly assess those of the C-S-H phases in hydrated cement. Chapter 3 provided detailed information on the position and mobility of the interlayer water molecules of 14 Å tobermorite using MD simulation. From the simulation result, it was noted that four water molecules (two W1s, W2, and W3) forming a Ca-centered octahedron with a Ca cation, and two OH groups of bridging silica tetrahedra within the interlayer space keep a similar distance from the centered Ca cation. Each of their oxygen atoms is attracted to and oriented toward the centered Ca cation. The position of their hydrogen atoms is oriented by the hydrogen bonds with other water molecules or the bridging oxygen of the silicate chain. In the Ca-centered octahedron, the W2 water molecule was transported between the upper and lower sites to form hydrogen bonds with the upper or lower W1 water molecules at room temperature. The W4 water molecule was strongly bonded by two OH groups of the upper and lower bridging tetrahedra. The W3 water molecule—one of four water molecules forming the Ca-centered octahedral—also has restrictive mobility since it is strongly bonded with the W4 water molecule. The W6 water molecule moves more actively than the others because of the less packed space. The self-diffusion coefficient of the interlayer water was calculated from the velocity autocorrelation function, and its order of magnitude was equivalent to that of water adsorbed on the inner surface of tobermorite. This implies that the interlayer water of the C-S-H phases has a similar transport rate to its surface adsorbed water.

Chapter 4 investigated the interactions between sodium or chloride ions and the C-S-H phases with the following Ca/Si ratios: 0.66, 0.95, 1.44, and 1.60. By using the contrast element maps reproduced from STXM images, it was observed that the C-S-H phase with 0.66 Ca/Si strongly interacts with sodium ions, while that with 1.60 Ca/Si does so with chloride ions. It is well known that in the C-S-H phases, the non-bridging oxygen of the silica tetrahedra—the end groups in silicate chains—induces a negative charge, and the positively charged calcium ions in the interlayer space counteract the

negative charge of the silicate chain. Based on our observation and the above fact, in Chapter 4 it was proposed that the ion selectivity of the C-S-H phases is governed by their residual charge. In other words, the lower Ca/Si C-S-H contains fewer Ca cations in the interlayer, which is not enough to balance the negative charge of the silicate chain. With this residual negative charge, the 0.66 Ca/Si C-S-H interacts strongly with the positively charged sodium ions to neutralize the residual charge. In contrast, the calcium-rich C-S-H acquires its residual positive charge in the opposite manner to the less Ca rich C-S-H. Consequently, the 1.60 Ca/Si C-S-H strongly interacted with the negatively charged chloride ions. The Si K-edge XANES of the Na-containing area in the C-S-H sample with 0.66 Ca/Si shifted toward a lower binding energy. The Si K-edge generally shifts to a lower binding energy with increased depolymerization of silicate chains. Therefore, the energy shift suggests the possibility that Na-interactions depolymerize the silicate chains. The probable site is the bridging silica tetrahedra that are known to be vulnerable. The energy shift helped to understand the variation in the structure of the silicate chain using the tobermorite-like C-S-H model.

The phase change of monosulfoaluminate as a function of the NaCl concentration was quantitatively analyzed with XRD, XANES spectra, and the least-square linear combination. In addition, the detailed phase assemblage was predicted using thermodynamic calculations. At low NaCl concentrations, the dissolution of monosulfoaluminate caused the ettringite formation, and the remaining monosulfoaluminate simultaneously transformed to Kuzel's salt. While increasing the NaCl concentration from 3 to 4 M, monosulfoaluminate transformed to Friedel's salt without its dissolution or transformation to Kuzel's salt. The important parameters regarding the phase change of monosulfoaluminate are more likely to be the free chloride content and ionic strength of the pore solution, and the available amount of monosulfoaluminate in hardened cement paste.

In Chapter 5, the ionic transport of the surface-treated concrete was investigated with the numerical model developed from the extended NPP model. To validate the model developed in Chapter 5, the simulation result was compared to the RCPT measurements. The simulation study indicated that the effectiveness of the surface treatment highly affected the ionic profiles and electric field during RCPT. Within the first few hours of RCPT, cations accumulated at the interfacial region, while anions were trapped in the cathode cell due to the low diffusivity of the surface treatment. As a result, this phenomenon created a local electric field. After the first few hours, anions were attracted by the accumulated cations at the interfacial region. This caused the local electric potential to be reduced and distributed along the sample depth. Since the ionic profiles and electric field are interactive, the proposed numerical model and algorithms in Chapter 5 suggest a method to compute more accurate diffusivity of the surface-treated concrete than the conventional one.

In Chapter 6, CLDH was applied to reduce the chloride-induced deterioration as the adsorbent and the protective material in cement-based materials. CLDHs do not only

adsorb chloride ions in aqueous solution with the memory effect, but also have a much higher binding capacity than the original LDHs. However, further research is required to understand the effect of a cementitious environment on chloride adsorption by CLDH. This adsorption in hardened cement paste was investigated in batch cultures to determine adsorption isotherms. Furthermore, the chloride adsorption by CLDH through the cement matrix was simulated using the Fickian model, and the simulation result was compared to the XRF chlorine map. Based on the result, it is proposed that the adsorption process is governed by the chloride transport through the cement matrix, which differs from that in an aqueous solution. XRD analysis showed that, in the cementitious environment the CLDH rebuilds the layered structure. Therefore, we found notable feasibility to apply the CLDH to the cement and concrete industry. In this thesis, we have investigated some of the research gaps regarding adsorption and transport in cement-based materials. The findings presented herein will contribute to the understanding of the durability of cement-based materials and provide fundamental information for further research.

References

[1] P.-C. Aïtcin, Cements of yesterday and today: Concrete of tomorrow, Cement and Concrete Research, 30 (2000) 1349-1359.

[2] R.M. Gataullin, Durability of reinforced-concrete containers for radioactive wastes, Atomic Energy, 93 (2002) 611-613.

[3] P.K. Mehta, P.J.M. Monteiro, Concrete: Microstructure, properties, and materials, McGraw-Hill, New Jersey (2006).

[4] F.P. Glasser, J. Marchand, E. Samson, Durability of concrete—Degradation phenomena involving detrimental chemical reactions, Cement and Concrete Research, 38 (2008) 226-246.

[5] H.F.W. Taylor, Cement chemistry, Thomas Telford, (1997).

[6] D.P. Calmet, Ocean disposal of radioactive waste: Status report, IAEA Bulletin, 31 (1989) 47-50.

[7] A.S. Abdulrahman, M. Ismail, M.S. Hussain, Corrosion inhibitors for steel reinforcement in concrete: A review, Scientific Research and Essays, 6 (2011) 4152-4162.

[8] ASTM C 125, Standard Terminology Relating to Concrete and Concrete Aggregates, American Society for Testing and Materials and Structures.

[9] L. Skinner, S. Chae, C. Benmore, H. Wenk, P. Monteiro, Nanostructure of calcium silicate hydrates in cements, Physical Review Letters, 104 (2010) 195502.

[10] I. Richardson, The calcium silicate hydrates, Cement and Concrete Research, 38 (2008) 137-158.

[11] R.J.M. Pellenq, N. Lequeux, H. Van Damme, Engineering the bonding scheme in CSH: The iono-covalent framework, Cement and Concrete Research, 38 (2008) 159-174.

[12] D.J.M. Flower, J.G. Sanjayan, Green house gas emissions due to concrete manufacture, The International Journal of Life Cycle Assessment, 12 (2007) 282-288.

[13] L.Y. Li, C.L. Page, Modelling of electrochemical chloride extraction from concrete: Influence of ionic activity coefficients, Computational Materials Science, 9 (1998) 303-308.

[14] L.Y. Li, C.L. Page, Finite element modelling of chloride removal from concrete by an electrochemical method, Corrosion Science, 42 (2000) 2145-2165.

[15] Y. Wang, L.Y. Li, C.L. Page, A two-dimensional model of electrochemical chloride removal from concrete, Computational Materials Science, 20 (2001) 196-212.

[16] Y. Wang, L.Y. Li, C.L. Page, Modelling of chloride ingress into concrete from a saline environment, Building and Environment, 40 (2005) 1573-1582.

[17] M. Kato, Numerical analysis of the Nernst-Planck-Poisson system, Journal of Theoretical Biology, 177 (1995) 299-304.

[18] E. Samson, J. Marchand, J.L. Robert, J.P. Bournazel, Modelling ion diffusion mechanisms in porous media, International Journal for Numerical Methods in Engineering, 46 (1999) 2043-2060.

[19] E. Samson, G. Lemaire, J. Marchand, J.J. Beaudoin, Modeling chemical activity effects in strong ionic solutions, Computational Materials Science, 15 (1999) 285-294.

[20] E. Samson, J. Marchand, Modeling the effect of temperature on ionic transport in cementitious materials, Cement and Concrete Research, 37 (2007) 455-468.

[21] E. Samson, J. Marchand, K.A. Snyder, J.J. Beaudoin, Modeling ion and fluid transport in unsaturated cement systems for isothermal conditions, Cement and Concrete Research, 35 (2005) 141-153.

[22] K. Krabbenhøt, J. Krabbenhøt, Application of the Poisson-Nernst-Planck equations to the migration test, Cement and Concrete Research, 38 (2008) 77-88.

[23] J. Bear, J.M. Buchlin, Modelling and applications of transport phenomena in porous media, Springer,   (1991).

[24] Y. Maltais, E. Samson, J. Marchand, Predicting the durability of Portland cement systems in aggressive environments-Laboratory validation, Cement and Concrete Research, 34 (2004) 1579-1589.

[25] L.A. Richards, Capillary conduction of liquids through porous mediums, Physics, 1 (1931) 318-333.

[26] J. Šelih, A.C.M. Sousa, T.W. Bremner, Moisture transport in initially fully saturated concrete during drying, Transport in Porous Media, 24 (1996) 81-106.

[27] D. Lockington, J. Parlange, Anomalous water absorption in porous materials, Journal of Physics D: Applied Physics, 36 (2003) 760.

[28] N.S. Martys, C.F. Ferraris, Capillary transport in mortars and concrete, Cement and Concrete Research, 27 (1997) 747-760.

[29] M.T. Van Genuchten, A closed-form equation for predicting the hydraulic conductivity of unsaturated soils, Soil Science Society of America Journal, 44 (1980) 892-898.

[30] C. Hall, Water sorptivity of mortars and concretes: A review, Magazine of Concrete Research, 41 (1989) 51-61.

[31] Y. Xi, Z.P. Bazant, H.M. Jennings, Moisture diffusion in cementitious materials adsorption

isotherms, Advanced Cement Based Materials, 1 (1994) 248-257.

[32] E.J. Garboczi, D.P. Bentz, Computer simulation of the diffusivity of cement-based materials, Journal of Materials Science, 27 (1992) 2083-2092.

[33] T.C. Powers, T.L. Brownyard, Studies of the physical properties of hardened Portland cement paste, ACI Journal Proceeding, 18 (1947) 101-132.

[34] D.P. Bentz, Influence of water-to-cement ratio on hydration kinetics: simple models based on spatial considerations, Cement and Concrete Research, 36 (2006) 238-244.

[35] A. Bentur, S. Diamond, N.S. Berke, Steel corrosion in concrete: Fundamental and civil engineering practice, Taylor & Francis, London (1997).

[36] M.H.F. Medeiros, P. Helene, Surface treatment of reinforced concrete in marine environment: Influence on chloride diffusion coefficient and capillary water absorption, Construction and Building Materials, 23 (2009) 1476-1484.

[37] V.S. Ramachandran, Possible states of chloride in the hydration of tricalcium silicate in the presence of calcium chloride, Materials and Structures, 4 (1971) 3-12.

[38] J.J. Beaudoin, V.S. Ramachandran, R.F. Feldman, Interaction of chloride and C-S-H, Cement and Concrete Research, 20 (1990) 875-883.

[39] A.K. Suryavanshi, J.D. Scantlebury, S.B. Lyon, Mechanism of Friedel's salt formation in cements rich in tri-calcium aluminate, Cement and Concrete Research, 26 (1996) 717-727.

[40] M.R. Jones, D.E. Macphee, J.A. Chudek, G. Hunter, R. Lannegrand, R. Talero, S.N. Scrimgeour, Studies using ^{27}Al MAS NMR of AFm and AFt phases and the formation of Friedel's salt, Cement and Concrete Research, 33 (2003) 177-182.

[41] H. Viallis, P. Faucon, J.C. Petit, A. Nonat, Interaction between salts (NaCl, CsCl) and calcium silicate hydrates (CSH), The Journal of Physical Chemistry B, 103 (1999) 5212-5219.

[42] J. Hill, A.W. Harris, M. Manning, A. Chambers, S.W. Swanton, The effect of sodium chloride on the dissolution of calcium silicate hydrate gels, Waste Management, 26 (2006) 758-768.

[43] D. Sugiyama, T. Fujita, Chemical Alteration of Calcium Silicate Hydrates in Saline Groundwater-Mechanism of Sorption of Na on CSH and Effect of NaCl on Leaching of Ca from CSH, Denryoku Chuo Kenkyujo Komae Kenkyujo Hokoku, (2004) 20P.

[44] D. Sugiyama, T. Fujita, A thermodynamic model of dissolution and precipitation of calcium silicate hydrates, Cement and Concrete Research, 36 (2006) 227-237.

[45] D. Sugiyama, Chemical alteration of calcium silicate hydrate (CSH) in sodium chloride solution, Cement and Concrete Research, 38 (2008) 1270-1275.

[46] A.G. Kalinichev, R.J. Kirkpatrick, Molecular dynamics modeling of chloride binding to the surfaces of calcium hydroxide, hydrated calcium aluminate, and calcium silicate phases, Chemistry of Materials, 14 (2002) 3539-3549.

[47] S.Y. Hong, F.P. Glasser, Alkali binding in cement pastes: Part I. The CSH phase, Cement and Concrete Research, 29 (1999) 1893-1903.

[48] U.A. Birnin-Yauri, F.P. Glasser, Friedel's salt, $Ca_2Al(OH)_6(Cl,OH) \cdot 2H_2O$: its solid solutions and their role in chloride binding, Cement and Concrete Research, 28 (1998) 1713-1723.

[49] M. Balonis, B. Lothenbach, G. Le Saout, F.P. Glasser, Impact of chloride on the mineralogy of hydrated Portland cement systems, Cement and Concrete Research, 40 (2010) 1009-1022.

[50] H. Zibara, D. Hooton, K. Yamada, M.D.A. Thomas, Roles of cement mineral phases in chloride binding, Cement Science and Concrete Technology, 56 (2002) 384-391.

[51] H. Hirao, K. Yamada, H. Takahashi, H. Zibara, Chloride binding of cement estimated by binding isotherms of hydrates, Journal of Advanced Concrete Technology, 3 (2005) 77-84.

[52] E. Bonaccorsi, S. Merlino, A.R. Kampf, The Crystal Structure of Tobermorite 14 Å (Plombierite), a C-S-H Phase, Journal of the American Ceramic Society, 88 (2005) 505-512.

[53] H.D. Megaw, C.H. Kelsey, Crystal structure of tobermorite, Nature, 177 (1956) 390-391.

[54] S. Merlino, E. Bonaccorsi, T. Armbruster, Tobermorites; their real structure and order-disorder (OD) character, American Mineralogist, 84 (1999) 1613.

[55] S. Merlino, E. Bonaccorsi, T. Armbruster, The real structures of clinotobermorite and tobermorite 9 A: OD character, polytypes, and structural relationships, European Journal of Mineralogy, 12 (2000) 411.

[56] S. Merlino, E. Bonaccorsi, T. Armbruster, The real structure of tobermorite 11A: normal and anomalous forms, OD character and polytypic modifications, European Journal of Mineralogy, 13 (2001) 577.

[57] B.D. Cullity, S.R. Stock, Elements of X-ray Diffraction, Prentice Hall, (2001).

[58] I.J. de Vries, R.B. Polder, Hydrophobic treatment of concrete, Construction and Building Materials, 11 (1997) 259-265.

[59] P.A.M. Basheer, L. Basheer, D.J. Cleland, A.E. Long, Surface treatments for concrete: Assessment methods and reported performance, Construction and Building Materials, 11 (1997) 413-429.

[60] M. Delucchi, A. Barbucci, G. Cerisola, Study of the physico-chemical properties of organic coatings for concrete degradation control, Construction and Building Materials, 11 (1997) 365-371.

[61] J.L.R. Thompson, M.R. Silsbee, P.M. Gill, B.E. Scheetz, Characterization of silicate sealers on concrete, Cement and Concrete Research, 27 (1997) 1561-1567.

[62] M. Ibrahim, A.S. Al-Gahtani, M. Maslehuddin, A.A. Almusallam, Effectiveness of concrete surface treatment materials in reducing chloride-induced reinforcement corrosion, Construction and Building Materials, 11 (1997) 443-451.

[63] A.M.G. Seneviratne, G. Sergi, C.L. Page, Performance characteristics of surface coatings applied to concrete for control of reinforcement corrosion, Construction and Building Materials, 14 (2000) 55-59.

[64] A.A. Almusallam, F.M. Khan, S.U. Dulaijan, O.S.B. Al-Amoudi, Effectiveness of surface coatings in improving concrete durability, Cement and Concrete Composites, 25 (2003) 473-481.

[65] H.Y. Moon, D.G. Shin, D.S. Choi, Evaluation of the durability of mortar and concrete applied with inorganic coating material and surface treatment system, Construction and Building Materials, 21 (2007) 362-369.

[66] M. Medeiros, P. Helene, Efficacy of surface hydrophobic agents in reducing water and chloride ion penetration in concrete, Materials and Structures, 41 (2008) 59-71.

[67] W.J. McCarter, Assessing the protective qualities of treated and untreated concrete surfaces under cyclic wetting and drying, Building and Environment, 31 (1996) 551-556.

[68] C.C. Yang, L.C. Wang, T.L. Weng, Using charge passed and total chloride content to assess the effect of penetrating silane sealer on the transport properties of concrete, Materials Chemistry and Physics, 85 (2004) 238-244.

[69] N.R. Buenfeld, J.Z. Zhang, Chloride diffusion through surface-treated mortar specimens, Cement and Concrete Research, 28 (1998) 665-674.

[70] J.Z. Zhang, I.M. McLoughlin, N.R. Buenfeld, Modelling of chloride diffusion into surface-treated concrete, Cement and Concrete Composites, 20 (1998) 253-261.

[71] C. Alonso, C. Andrade, M. Castellote, P. Castro, Chloride threshold values to depassivate reinforcing bars embedded in a standardized OPC mortar, Cement and Concrete Research, 30 (2000) 1047-1055.

[72] M. Saremi, E. Mahallati, A study on chloride-induced depassivation of mild steel in simulated concrete pore solution, Cement and Concrete Research, 32 (2002) 1915-1921.

[73] T.A. Söylev, M.G. Richardson, Corrosion inhibitors for steel in concrete: State-of-the-art report, Construction and Building Materials, 22 (2008) 609-622.

[74] C. Andrade, C. Alonso, M. Acha, B. Malric, Preliminary testing of Na2PO3F as a curative corrosion inhibitor for steel reinforcements in concrete, Cement and Concrete Research, 22 (1992) 869-881.

[75] K. Soeda, T. Ichimura, Present state of corrosion inhibitors in Japan, Cement and Concrete Composites, 25 (2003) 117-122.

[76] R.K. Dhir, M.A.K. El-Mohr, T.D. Dyer, Chloride binding in GGBS concrete, Cement and Concrete Research, 26 (1996) 1767-1773.

[77] G.K. Glass, N.R. Buenfeld, The presentation of the chloride threshold level for corrosion of steel in concrete, Corrosion Science, 39 (1997) 1001-1013.

[78] H. Tatematsu, T. Sasaki, Repair materials system for chloride-induced corrosion of reinforcing bars, Cement and Concrete Composites, 25 (2003) 123-129.

[79] L. Raki, J.J. Beaudoin, L. Mitchell, Layered double hydroxide-like materials: nanocomposites for use in concrete, Cement and Concrete Research, 34 (2004) 1717-1724.

[80] L. Raki, J.J. Beaudoin, Release formulation of chemical admixtures in cement and concrete, US Patent, (2007), No. US20070022916A.

[81] S. Nonaka, T. Sato, Cement modifier, Japan Patent, (2001), No. JP2001089211A.

[82] E. Tatematsu, T. Nakamura, H. Koshimizu, S. Takatsu, Chlorine ion scavenger, Japan Patent, (1992), No. JP04154648A.

[83] M. Morioka, K. Ashida, M. Handa, Cement admixture and cement composition, Japan Patent, (1993), No. JP05262546A.

[84] K. Michio, Cement mortar capable of preventing salt damage and rusting, Japan Patent, (1997), No. JP09142903A.

[85] H. Tatematsu, T. Nakamura, H. Koshimizu, T. Morishita, H. Kotaki, Cement-additive for inhibiting concrete-deterioration, US Patent, (1995), No. US5435846A.

[86] T. Sato, T. Wakabayashi, M. Shimada, Adsorption of various anions by magnesium aluminum oxide of ($Mg_{0.7}Al_{0.3}O_{1.15}$), Industrial & Engineering Chemistry Product Research and Development, 25 (1986) 89-92.

[87] J.G. Nunan, P.B. Himelfarb, R.G. Herman, K. Klier, C.E. Bogdan, G.W. Simmons, Methanol synthesis catalysts based on $Cs/Cu/ZnO/M_2O_3$ (M= Al, Cr, Ga): genesis from coprecipitated hydrotalcite-like precursors, solid-state chemistry, morphology, and stability, Inorganic Chemistry, 28 (1989) 3868-3874.

[88] L. Lv, J. He, M. Wei, D.G. Evans, X. Duan, Uptake of chloride ion from aqueous solution by calcined layered double hydroxides: equilibrium and kinetic studies, Water Research, 40 (2006) 735-743.

[89] J. Hua, L. Lu, Chloride removal from wastewater by thermally treated hydrotalcite, Chinese Journal of Geochemistry, 25 (2006) 255-256.

[90] S.V. Churakov, P. Mandaliev, Structure of the hydrogen bonds and silica defects in the tetrahedral double chain of xonotlite, Cement and Concrete Research, 38 (2008) 300-311.

[91] S.V. Churakov, Structural position of H_2O molecules and hydrogen bonding in anomalous 11 A tobermorite, American Mineralogist, 94 (2009) 156.

[92] R.T. Cygan, J.J. Liang, A.G. Kalinichev, Molecular models of hydroxide, oxyhydroxide, and clay phases and the development of a general force field, The Journal of Physical Chemistry B, 108 (2004) 1255-1266.

[93] A.G. Kalinichev, J. Wang, R.J. Kirkpatrick, Molecular dynamics modeling of the structure, dynamics and energetics of mineral-water interfaces: Application to cement materials, Cement and Concrete Research, 37 (2007) 337-347.

[94] S. Li, W.K. Liu, Meshfree and particle methods and their applications, Applied Mechanics Reviews, 55 (2002) 1.

[95] K. Benzerara, T.H. Yoon, T. Tyliszczak, B. Constantz, A.M. Spormann, G.E. Brown Jr, Scanning transmission X-ray microscopy study of microbial calcification, Geobiology, 2 (2004) 249-259.

[96] T. Tyliszczak, T. Warwick, A.L.D. Kilcoyne, S. Fakra, D.K. Shuh, T.H. Yoon, G.E. Brown Jr, S. Andrews, V. Chembrolu, J. Strachan, Soft X-ray scanning transmission microscope working in an extended energy range at the advanced light source, international conference on synchrotron radiation instrumentation, American Institute of Physics, San Francisco, United States, 2004, 1356-1359.

[97] J. Ha, S. Chae, K.W. Chou, T. Tyliszczak, P.J.M. Monteiro, Scanning Transmission X-Ray Microscopic Study of Carbonated Calcium Silicate Hydrate, Transportation Research Record, 2142 (2010) 83-88.

[98] J. Ha, S. Chae, K.W. Chou, T. Tyliszczak, P.J.M. Monteiro, Effect of polymers on the nanostructure and on the carbonation of calcium silicate hydrates: A scanning transmission X-ray microscopy study, Journal of Materials Science, (2011) 1-14.

[99] D.C. Koningsberger, R. Prins, X-ray absorption: Principles, applications, techniques of EXAFS, SEXAFS and XANES, Wiley, New York (1987).

[100] AASHTO T 277, Standard test method for electrical indication of concrete's ability to resist chloride iron penetration, American Association of State and Highway Transportation Officials.

[101] ASTM C 1202-10, Standard test method for electrical indication of concrete's ability to resist chloride ion penetration, American Society for Testing and Materials and Structures.

[102] NT Build 492, Chloride migration coefficient from non-steady state migration experiment, Nordtest Method.

[103] E. Samson, J. Marchand, K.A. Snyder, Calculation of ionic diffusion coefficients on the

basis of migration test results, Materials and Structures, 36 (2003) 156-165.

[104] M.T. Bassuoni, M.L. Nehdi, T.R. Greenough, Enhancing the reliability of evaluating chloride ingress in concrete using the ASTM C 1202 rapid chloride penetrability test, Journal of ASTM International, 3 (2006) 1-13.

[105] K. Stanish, R.D. Hooton, M.D.A. Thomas, A novel method for describing chloride ion transport due to an electrical gradient in concrete: part 2. experimental study, Cement and Concrete Research, 34 (2004) 51-57.

[106] R.J. Kirkpatrick, A.G. Kalinichev, X. Hou, L. Struble, Experimental and molecular dynamics modeling studies of interlayer swelling: water incorporation in kanemite and ASR gel, Materials and Structures, 38 (2005) 449-458.

[107] O. Teleman, B. Jönsson, S. Engström, A molecular dynamics simulation of a water model with intramolecular degrees of freedom, Molecular Physics, 60 (1987) 193-203.

[108] H.J.C. Berendsen, J.P.M. Postma, W.F. Van Gunsteren, J. Hermans, Interaction models for water in relation to protein hydration, Intermolecular forces, 331 (1981) 331-342.

[109] H.J.C. Berendsen, J.R. Grigera, T.P. Straatsma, The missing term in effective pair potentials, Journal of Physical Chemistry, 91 (1987) 6269-6271.

[110] D.E. Smith, L.X. Dang, Computer simulations of NaCl association in polarizable water, Journal of Chemical Physics, 100 (1994) 3757-3766.

[111] M. Griebel, S. Knapek, G.W. Zumbusch, Numerical simulation in molecular dynamics: Numerics, algorithms, parallelization, applications, Springer,   (2007).

[112] S. Plimpton, e. al., LAMMPS: Large-scale Atomic/Molecular Massively Parallel Simulator, Sandia National Laboratories, 2011.

[113] H.M. Jennings, Colloid model of C-S-H and implications to the problem of creep and shrinkage, Materials and Structures, 37 (2004) 59-70.

[114] D. Chandler, Introduction to modern statistical mechanics, Oxford University Press, (1987).

[115] M. Toda, R. Kubo, N. Saitō, N. Hashitsume, Statistical physics: Nonequilibrium statistical mechanics, Springer,   (1992).

[116] K.S. Smirnov, D. Bougeard, A molecular dynamics study of structure and short-time dynamics of water in kaolinite, The Journal of Physical Chemistry B, 103 (1999) 5266-5273.

[117] H. Manzano, J.S. Dolado, A. Guerrero, A. Ayuela, Mechanical properties of crystalline calcium-silicate-hydrates: comparison with cementitious C-S-H gels, Physica Status Solidi (a), 204 (2007) 1775-1780.

[118] J.P. Korb, P.J. McDonald, L. Monteilhet, A.G. Kalinichev, R.J. Kirkpatrick, Comparison of proton field-cycling relaxometry and molecular dynamics simulations for proton-water surface dynamics in cement-based materials, Cement and Concrete Research, 37 (2007) 348-350.

[119] X. Pardal, I. Pochard, A. Nonat, Experimental study of Si–Al substitution in calcium-silicate-hydrate (CSH) prepared under equilibrium conditions, Cement and Concrete Research, 39 (2009) 637-643.

[120] T. Matschei, B. Lothenbach, F. Glasser, The AFm phase in Portland cement, Cement and Concrete Research, 37 (2007) 118-130.

[121] R.B. Perkins, C.D. Palmer, Solubility of ettringite ($Ca_6[Al(OH)_6]_2(SO_4)_3 \cdot 26H_2O$) at 5-75 ℃, Geochimica et Cosmochimica Acta, 63 (1999) 1969-1980.

[122] PANalytical, X'Pert HighScore Plus, Almelo, Netherlands, 2006.

[123] A. Hitchcock, P. Hitchcock, C. Jacobsen, C. Zimba, B. Loo, E. Rotenberg, J. Denlinger, R. Kneedler, aXis 2000-Analysis of X-ray Images and Spectra, McMaster University, Canada, (2006).

[124] B. Ravel, M. Newville, ATHENA, ARTEMIS, HEPHAESTUS: data analysis for X-ray absorption spectroscopy using IFEFFIT, Journal of Synchrotron Radiation, 12 (2005) 537-541.

[125] D.L. Parkhurst, C.A.J. Appelo, S. Geological, User's guide to PHREEQC (Version 2): a computer program for speciation, batch-reaction, one-dimensional transport, and inverse geochemical calculations, US Geological Survey,   (1999).

[126] K.A. Bond, T.G. Heath, C.J. Tweed, HATCHES: a referenced thermodynamic database for chemical equilibrium studies, Nirex Report, 379 (1997).

[127] J.V. Bothe, PHREEQC modeling of Friedel's salt equilibria at 23±1℃, Cement and Concrete Research, 34 (2004) 1057-1063.

[128] S. Chatterji, Mechanism of the $CaCl_2$ attack on Portland cement concrete, Cement and Concrete Research, 8 (1978) 461-467.

[129] G. Renaudin, F. Kubel, J.P. Rivera, M. Francois, Structural phase transition and high temperature phase structure of Friedels salt, $3CaO \cdot Al_2O_3 \cdot CaCl_2 \cdot 10H_2O$, Cement and Concrete Research, 29 (1999) 1937-1942.

[130] J.P. Rapin, G. Renaudin, E. Elkaim, M. Francois, Structural transition of Friedel's salt $3CaO \cdot Al_2O_3 \cdot CaCl_2 \cdot 10H_2O$ studied by synchrotron powder diffraction, Cement and Concrete Research, 32 (2002) 513-519.

[131] M.D. Andersen, H.J. Jakobsen, J. Skibsted, Characterization of the α-β phase transition in Friedel's salt ($Ca_2Al (OH)_6Cl \cdot 2H_2O$) by variable-temperature ^{27}Al MAS NMR spectroscopy, The Journal of Physical Chemistry A, 106 (2002) 6676-6682.

[132] M. Balonis, F.P. Glasser, The density of cement phases, Cement and Concrete Research, 39 (2009) 733-739.

[133] D. Li, G. Bancroft, M. Fleet, X. Feng, Silicon K-edge XANES spectra of silicate minerals, Physics and Chemistry of Minerals, 22 (1995) 115-122.

[134] P. Hewlett, Lea's chemistry of cement and concrete, Butterworth-Heinemann, (2004).

[135] X. Cong, R.J. Kirkpatrick, 29Si MAS NMR study of the structure of calcium silicate hydrate, Advanced Cement Based Materials, 3 (1996) 144-156.

[136] E. Wieland, R. Dähn, M. Vespa, B. Lothenbach, Micro-spectroscopic investigation of Al and S speciation in hardened cement paste, Cement and Concrete Research, 40 (2010) 885-891.

[137] S.J. Naftel, T.K. Sham, Y.M. Yiu, B.W. Yates, Calcium L-edge XANES study of some calcium compounds, Journal of Synchrotron Radiation, 8 (2001) 255-257.

[138] M. Newville, IFEFFIT: interactive XAFS analysis and FEFF fitting, Journal of Synchrotron Radiation, 8 (2001) 322-324.

[139] H.F.W. Taylor, C. Famy, K.L. Scrivener, Delayed ettringite formation, Cement and Concrete Research, 31 (2001) 683-693.

[140] ASTM C 1152, Standard test method for acid-soluble chloride in mortar and concrete, American Society for Testing and Materials and Structures.

[141] D.A. Lange, H.M. Jennings, S.P. Shah, Image analysis techniques for characterization of pore structure of cement-based materials, Cement and Concrete Research, 24 (1994) 841-853.

[142] T. Luping, L.O. Nilsson, Rapid determination of the chloride diffusivity in concrete by applying an electric field, ACI Materials Journal, 89 (1993) 49-53.

[143] J.Z. Zhang, N.R. Buenfeld, Chloride profiles in surface-treated mortar specimens, Construction and Building Materials, 14 (2000) 359-364.

[144] J. Crank, The mathematics of diffusion, Clarendon Press Oxford, (1979).

[145] J. Wang, A.G. Kalinichev, J.E. Amonette, R.J. Kirkpatrick, Interlayer structure and dynamics of Cl-bearing hydrotalcite: far infrared spectroscopy and molecular dynamics modeling, American Mineralogist, 88 (2003) 398-409.

[146] O.E. Gjørv, Durability and service life of concrete structures, The First Fib Congress, Japan Prestressed Concrete Engineering Association, Tokyo, 2002, 1-16.

[147] P. Lambert, C.L. Page, N.R. Short, Pore solution chemistry of the hydrated system tricalcium silicate/sodium chloride/water, Cement and Concrete Research, 15 (1985) 675-680.

[148] C. Andrade, C.L. Page, Pore solution chemistry and corrosion in hydrated cement systems

containing chloride salts: a study of cation specific effects, British Corrosion Journal, 21 (1986) 49-53.

[149] R.H. Rogue, W. Lerch, Hydration of Portland cement compounds, Industrial & Engineering Chemistry, 26 (1934) 837-847.

[150] ASTM C 1218-99, Standard test method for water-soluble chloride in mortar and concrete, American Society for Testing and Materials and Structures.

[151] X. Feng, E.J. Garboczi, D.P. Bentz, P.E. Stutzman, T.O. Mason, Estimation of the degree of hydration of blended cement pastes by a scanning electron microscope point-counting procedure, Cement and Concrete Research, 34 (2004) 1787-1793.

[152] I. Langmuir, The adsorption of gases on plane surfaces of glass, mica and platinum, Journal of the American Chemical Society, 40 (1918) 1361-1403.

[153] H.M.F. Freundlich, Over the adsorption in solution, The Journal of Physical Chemistry, 57 (1906) 385-470.

[154] S. Lagergren, About the theory of so-called adsorption of soluble substances, Kungliga Svenska Vetenskapsakademiens Handlingar, 24 (1898) 1-39.

[155] Y.S. Ho, G. McKay, Sorption of dye from aqueous solution by peat, Chemical Engineering Journal, 70 (1998) 115-124.

[156] Y.S. Ho, G. McKay, D.A.J. Wase, C.F. Forster, Study of the sorption of divalent metal ions on to peat, Adsorption Science & Technology, 18 (2000) 639-650.

[157] J. Zeldowitsch, Über den mechanismus der katalytischen oxydation von CO an MnO_2, Acta Physicochim URSS, 1 (1934) 364-449.

[158] Y.S. Ho, G. McKay, A comparison of chemisorption kinetic models applied to pollutant removal on various sorbents, Process Safety and Environmental Protection, 76 (1998) 332-340.